

Inelastic Majorana Dark Matter and Its Self-Interactions in a Gauged $U(1)_{L_\mu-L_\tau}$ Model

Kwei-Chou Yang^{1,*}

¹*Department of Physics and Center for High Energy Physics,
Chung Yuan Christian University, 200 Chung Pei Road, Taoyuan 32023, Taiwan*

We develop an inelastic Majorana dark matter model gauged by $U(1)_{L_\mu-L_\tau}$ symmetry, featuring a complex scalar and fermions with a small Dirac mass. The model exhibits strong interactions between the dark fermion-antifermion pair and the scalar, with a large coupling generating a Majorana mass after symmetry breaking. The dark fermion splits into two nearly degenerate Majorana eigenstates, with the $U(1)_{L_\mu-L_\tau}$ gauge boson Z' interacting via inelastic axial vector currents. The lighter Majorana serves as dark matter (DM), while the heavier may also contribute. The model predicts DM masses ranging from about 10 GeV to hundreds of GeV, with the scalar favored below 100 MeV. Strong coupling causes DM particles to mainly annihilate into two scalars, which determines the relic abundance, while thermal equilibrium with the bath occurs through Z' interactions. Self-interacting DM particles scatter via ladder exchange of strongly coupled light scalars, helping resolve small-scale issues. The Z' interacts with the muon, affecting its magnetic moment and explaining the $(g-2)_\mu$ discrepancy. Effects on experiments, N_{eff} , and the Hubble tension from kinetic mixing between Z' and the photon, originating from high-energy scales, are discussed. The model details and parameter constraints used in experiments are also covered.

arXiv:2512.05694v1 [hep-ph] 5 Dec 2025

* kcyang@cycu.edu.tw

I. INTRODUCTION

Generally, dark matter may be made up of particles with slight mass differences. In such cases, it is called inelastic dark matter (iDM). This idea was proposed to explain discrepancies observed in early direct-detection experiments such as DAMA and CDMS [1, 2]. Since then, research on inelastic dark matter has expanded to include a broader range of areas, including direct and indirect detection methods, particle physics experiments, and astronomical observations, as well as explanations and predictions of the Universe’s evolution [3–24].

One example is a type of iDM called pseudo-Dirac fermion dark matter [6, 11, 14, 20, 22–24]. This model has recently gained significant attention and has been studied extensively. In the simplest $U(1)$ symmetry scenario, the dark sector particles consist of a Dirac fermion and its antiparticle with mass m_D , along with a complex scalar. This model features a weak interaction, characterized by a coupling strength of f , between the dark Dirac fermion-antifermion pair and the dark scalar. When spontaneous symmetry breaking (SSB) occurs, it results in a small Majorana mass “ fv_S ”, where v is the vacuum expectation value of the scalar after SSB. After symmetry breaking, the Dirac particles in the dark sector split into two nearly identical Majorana eigenstates ($m_D \pm fv_S$), referred to as pseudo-Dirac dark matter. Producing pseudo-Dirac dark matter with a tiny mass difference generally suggests that f is also small.

We aim to develop a minimal iDM dark matter model that accounts for key astronomical observations and experimental results. The model includes the following features. Besides the complex scalar (ϕ_S), the dark sector also contains fermions (χ, χ^c) with a very small Dirac mass m_D . A strong coupling occurs between the dark fermion-antifermion pair and the dark scalar, resulting in interaction terms such as $(f/\sqrt{2})\bar{\chi}\chi^c\phi_S$ for these dark particles, with a sizable coupling constant f . This term produces the Majorana mass “ fv_S ” after SSB. After symmetry breaking, the dark sector fermions split into two Majorana states ($fv \pm m_D$) with nearly degenerate masses. Following SSB, the lighter Majorana particle (χ_-) serves as dark matter. The heavier Majorana particles (χ_+) might also contribute to current dark matter, depending on their lifetimes or whether they are regenerated in the dense inner halo through upscattering.

Our model predicts dark matter masses ranging from about 10 GeV to several hundred GeV, while scalar particles (S) have masses roughly between 10 MeV and a few hundred MeV, with a preference for less than 100 MeV. Due to the large coupling constant f between dark matter and the scalar, the annihilation process $\chi_{\mp}\chi_{\mp} \rightarrow SS$ is the dominant reaction during dark matter freeze-out, resulting in the current relic abundance. Furthermore, dark matter can undergo multiple elastic

interactions via these strongly coupled light scalar bosons. These self-interactions can transfer heat from the inner regions to the outer parts of the halo, reducing the density at the core [25–27]. In Sec. X, we will analyze dark matter self-scattering cross sections and discuss related small-scale challenges.

Before symmetry breaking, the dark sector we built satisfies the $U(1)_{L_\mu-L_\tau}$ gauge symmetry. This model is the simplest extension of the SM that introduces inelastic Majorana dark matter and can account for the currently measured anomalous magnetic moment of muons, while remaining anomaly-free. The muon and tauon lepton doublets in the SM interact with the $U(1)_{L_\mu-L_\tau}$ gauge boson Z' because they have opposite charges under this symmetry. Since Z' couples to the muon, it affects the muon's magnetic moment, potentially explaining the $(g-2)_\mu$ discrepancy [28], known as the $L_\mu-L_\tau$ scenario [29–40]. As a result, when using this model to explain the $(g-2)_\mu$ anomaly, we can determine the parameter space for the Z' - μ coupling strength and the Z' mass. We will also review current experimental constraints on this parameter space. Additionally, we will analyze how the kinetic-energy mixing between Z' and the photon, originating at high energy scales, affects specific experiments.

The experimental results of $(g-2)_\mu$ [41–45] indicate that the coupling constant between Z' and the muon is roughly $4 \times 10^{-4} \sim 10^{-3}$. Although its value minimally impacts dark matter self-scattering, it is enough for S to remain in thermal equilibrium with the SM bath through $S \leftrightarrow Z'Z'$ interactions until dark matter freezes out. Therefore, while S particles can directly interact with SM particles via the mixing angle α , which arises from mixing with the SM Higgs, this angle is not necessary to maintain thermal equilibrium, allowing for minimal α values. We will analyze the constraints imposed by different experiments on α in Sec. IX.

During thermal evolution, S and Z' can remain in thermal equilibrium with ν_μ and ν_τ . Because Z' can mix with photons, when the weak interaction rate drops below the Universe's expansion rate, photons and electrons can temporarily stay in thermal equilibrium with other neutrinos via $Z' \rightarrow e^+e^-$. This will affect current N_{eff} observations and might also alleviate the Hubble tension.

Although both this model and the inelastic pseudo-Dirac model involve dark sector Dirac fermions transforming into two nearly degenerate Majorana particles after symmetry breaking, they still have some crucial differences. In the pseudo-Dirac model, the masses of the Majorana particles mainly result from the initial Dirac mass term in the dark sector, and the inelastic vector currents, $\bar{\chi}_\pm \gamma_\mu \chi_\mp$, interact with the gauge boson Z' , even though the Majorana nature prevents the elastic vector current. Although the fermions in the pseudo-Dirac model are Majorana particles, the overall properties of macroscopic Dirac particles are still preserved. The model presented

in this paper is called the inelastic Majorana dark matter model. The main contribution to the eigenmasses of Majorana particles arises from the Majorana mass term after SSB, and the Z' particles are coupled to the inelastic axial vector currents, $\chi_{\pm}\gamma_{\mu}\gamma_5\chi_{\mp}$. This model is not regarded as a pseudo-Majorana model for two reasons: first, to avoid the misconception that the dark matter particle in this model is not Majorana; second, because the inelastic axial-vector current can still be considered a characteristic of Majorana particles.

The rest of this article is organized as follows. In Sec. II, we provide a detailed description of the inelastic Majorana $U(1)_{L_{\mu}-L_{\tau}}$ model. In Appendix A, we list the derivation of the eigenmasses and eigenstates of the Dark sector Majorana particles. In Sec. II C, we discuss mixing between Z' and photons, or between Z' and Z , at the one-loop level or due to kinetic-energy mixing at high-energy scales. We also derive the interaction terms for the neutral gauge field coupling to SM and dark-sector particles in the Lagrangian, with the relevant calculations provided in Appendix B. Sec. III describes the independent parameters required.

Sec. IV explores $(g-2)_{\mu}$ and its parameter space, along with other experimental constraints on the parameters. In Sec. V, we examine the thermal evolution of dark matter and the constraints that certain parameters must meet when $\chi_{\mp}\chi_{\mp}$ mainly annihilate to SS . Sec. VI investigates possible values of N_{eff} within this model and the parameter configurations needed to alleviate the Hubble tension. Sec. VII analyzes how the mass splitting in dark matter and the lifetime of excited dark matter affect the remaining amount of excited dark matter.

Sec. VIII examines the impact of the Sommerfeld factor on dark matter relic abundance. By incorporating the Sommerfeld enhancement factor, we also investigate the indirect detection of dark matter self-annihilation. In Sec. IX, we present and analyze the experimental constraints on the mixing angle α arising from mixing between the dark-sector scalar and the SM Higgs. Sec. X discusses the calculation of DM self-scattering cross sections and their implications for solving small-scale structure issues. In Sec. XI, we review various experiments and methods that could support iDM measurements and evaluate their impact on the model. We conclude with a summary in Sec. XII. Further details and relevant formulas are included in the Appendices.

II. DESCRIPTION OF THE INELASTIC MAJORANA DARK MATTER MODEL

We consider a minimal extension of the inelastic Majorana dark matter model for which the dark sector is gauged under a local $U(1)_{L_{\mu}-L_{\tau}}$ symmetry with a gauge boson Z' . Meanwhile, the SM μ and τ sectors can interact with the dark sector by exchanging the gauge boson Z' associated

	$SU(2)_L$	$U(1)_Y$	$U(1)_{L_\mu-L_\tau}: q_{L_d}$
$L_\mu = (\nu_\mu, \mu_L)$	2	-1/2	$q_{\mu\tau}$
$L_\tau = (\nu_\tau, \tau_L)$	2	-1/2	$-q_{\mu\tau}$
μ_R	1	-1	$q_{\mu\tau}$
τ_R	1	-1	$-q_{\mu\tau}$
ϕ_H	2	1/2	0
χ	1	0	q_d
ϕ_S	1	0	$2q_d$

TABLE I. Charge assignments, where the generic $U(1)_{L_\mu-L_\tau}$ charge is denoted as q_{L_d} .

with the $L_\mu - L_\tau$ symmetry,

$$\mathcal{L} \supset -g_d q_{\mu\tau} Z'_\mu J_{L_\mu-L_\tau}^\mu, \quad (1)$$

with

$$J_{L_\mu-L_\tau}^\mu = \bar{\mu}\gamma^\mu\mu - \bar{\tau}\gamma^\mu\tau + \bar{\nu}_{\mu L}\gamma^\mu\nu_{\mu L} - \bar{\nu}_{\tau L}\gamma^\mu\nu_{\tau L}, \quad (2)$$

where g_d is the coupling constant related to the Z' , which couples to μ - and τ -lepton sectors with charge $+q_{\mu\tau}$ and $-q_{\mu\tau}$, respectively. We assume the dark sector contains a vector-like Dirac fermion χ and a Higgs-like complex scalar ϕ_S with the $U(1)_D$ charge assigned to be $+q_d$ and $+2q_d$, respectively. The charge assignments for all relevant particles are summarized in Table I. In the study, we use $g_{\mu\tau} \equiv g_d q_{\mu\tau}$, and $g_\chi = g_d q_d = g_{\mu\tau} \times (q_d/q_{\mu\tau})$ as free parameters to take into account their relative size.

In the following subsections, we will separately discuss (i) the mixing of the dark scalar and SM Higgs, (ii) the dark eigen-Majorana states and their interactions, and (iii) the possible kinetic mixing between Z' and SM neutral gauge bosons, Z and A (photon).

A. The Higgs sector

The Higgs portal may hint at the dark sector interacting with SM particles owing to mixing between the dark scalar ϕ_S and the SM Higgs doublet ϕ_H . The relevant Lagrangian is described by

$$\mathcal{L}_{\text{Higgs}} = (D_\mu\phi_H)^\dagger D^\mu\phi_H + (D_\mu\phi_S)^\dagger D^\mu\phi_S - V(\phi_H, \phi_S), \quad (3)$$

where $D_\mu\phi_{S,H} = (\partial_\mu + iq_{S,H}g_d Z'_\mu)\phi_{S,H}$ with $U(1)_D$ charges $q_H = 0$ and $q_S = 2q_d$, and with $q_S g_d \equiv 2g_\chi$. Here, the potential is given by

$$V(\phi_H, \phi_S) = -\mu_H^2 \phi_H^\dagger \phi_H + \lambda_H (\phi_H^\dagger \phi_H)^2 - \mu_S^2 \phi_S^\dagger \phi_S + \lambda_S (\phi_S^\dagger \phi_S)^2 + \lambda_{SH} (\phi_S^\dagger \phi_S) (\phi_H^\dagger \phi_H). \quad (4)$$

We consider $SU(2)_L \times U(1)_Y \times U(1)_D$ is spontaneously broken into $U(1)_{\text{QED}} \times Z_2$, where the Z_2 symmetry invariant under $\chi_\pm \rightarrow -\chi_\pm$ stabilizes the lightest dark-sector Majorana fermion which becomes the dark matter candidate (which will be further discussed in the following subsection). The parameter requirements are as follows. The spontaneous symmetry breaking (SSB) requires $\mu_H^2 > 0$ and $\mu_S^2 > 0$. The vacuum stability needs $\lambda_H > 0, \lambda_S > 0$ and $\lambda_{SH} > -2\sqrt{\lambda_H \lambda_S}$. The conditions with scalar eigenmasses $m_S^2, m_H^2 > 0$ give $\lambda_{SH}^2 < 4\lambda_H \lambda_S$.

Writing $\phi_H = \exp(i\tau^a \zeta^a / v_H) \cdot (0, (\phi_h + v_H) / \sqrt{2})^T$ and $\phi_S = \exp(i\sigma / v_S) (\phi_s + v_S) / \sqrt{2}$, the three fields ζ^a and the field σ can be set as zero respectively through the unitarity transformation; the former three (ζ^a) have then become the longitudinal degrees of freedom (DoFs) of W^\pm and Z , while the latter one (σ) the longitudinal DoF of Z' . The vacuum expectation value v_S , for which its additional phase (or sign) can be absorbed by field redefinitions of the dark sector particles, is taken to be positive. Thus, $(D_\mu \phi_S)^\dagger D^\mu \phi_S$ will give rise to the Z' 's mass term, $m_{Z'}^2 Z'_\mu Z'^\mu / 2$ with $m_{Z'} = 2g_\chi v_S$.

We can then represent the post-SSB Higgs-sector Lagrangian in terms of the neutral fields (ϕ_s, ϕ_h) , where the mass term is

$$\frac{1}{2} (\phi_s, \phi_h) \mathcal{M}^2 \begin{pmatrix} \phi_s \\ \phi_h \end{pmatrix} \quad (5)$$

with

$$\mathcal{M}^2 = \begin{pmatrix} 2\lambda_S v_S^2 & \lambda_{SH} v_S v_H \\ \lambda_{SH} v_S v_H & 2\lambda_H v_H^2 \end{pmatrix}. \quad (6)$$

Diagonalizing the mass matrix, the two neutral fields can be further expressed by the corresponding mass eigenstates (s, H) ,

$$\begin{pmatrix} \phi_s \\ \phi_h \end{pmatrix} = \begin{pmatrix} \cos \alpha & \sin \alpha \\ -\sin \alpha & \cos \alpha \end{pmatrix} \begin{pmatrix} S \\ H \end{pmatrix}, \quad (7)$$

where the mixing angle α satisfies the condition,

$$\sin 2\alpha = \frac{v_S v_H \lambda_{SH}}{\sqrt{(\lambda_H v_H^2 - \lambda_S v_S^2)^2 + (\lambda_{SH} v_S v_H)^2}} = \frac{2v_S v_H \lambda_{SH}}{m_H^2 - m_S^2}, \quad (8)$$

and the eigenmasses squared (m_S^2, m_H^2) are given by

$$\begin{aligned} m_S^2 &= \lambda_H v_H^2 + \lambda_S v_S^2 - \sqrt{(\lambda_H v_H^2 - \lambda_S v_S^2)^2 + (\lambda_{SH} v_S v_H)^2}, \\ m_H^2 &= \lambda_H v_H^2 + \lambda_S v_S^2 + \sqrt{(\lambda_H v_H^2 - \lambda_S v_S^2)^2 + (\lambda_{SH} v_S v_H)^2}. \end{aligned} \quad (9)$$

In the paper, we use H to be the SM-like Higgs with mass $m_H = 125.25$ GeV [46]. The Lagrangian for S , which includes its self-interaction terms and interactions with the dark gauge field, is given by

$$\begin{aligned} \mathcal{L} \supset & \frac{1}{2} \partial_\mu S \partial^\mu S - \frac{1}{2} m_S^2 S^2 - \left(\frac{g_\chi m_S^2 c_\alpha^3}{m_{Z'}} + \frac{m_S^2 s_\alpha^3}{2v_H} \right) S^3 + \frac{g_\chi^2}{2m_{Z'}^2} (c_\alpha^2 m_S^2 + s_\alpha^2 m_H^2) c_\alpha^4 S^4 \\ & + 2c_\alpha^2 g_\chi^2 S^2 Z'^\mu Z'_\mu + 2c_\alpha g_\chi m_{Z'} S Z'^\mu Z'_\mu + \dots, \end{aligned} \quad (10)$$

where $c_\alpha \equiv \cos \alpha$ and $s_\alpha \equiv \sin \alpha$.

B. The dark sector part involving dark fermions

The interaction containing the dark sector fermion is given by

$$\mathcal{L}_\chi = i\bar{\chi}\gamma^\mu D_\mu \chi - m_D \bar{\chi}\chi - \frac{f}{\sqrt{2}} \bar{\chi}^c \chi \phi_S^* - \frac{f^*}{\sqrt{2}} \bar{\chi} \chi^c \phi_S, \quad (11)$$

where $m_\chi > 0$ corresponds to a Dirac mass, $\chi^c \equiv C\bar{\chi}^T$ is the charge conjugate of χ , $D_\mu = \partial_\mu + ig_d \hat{q}_D Z'_\mu$ is the covariant derivative, with \hat{q}_D the $U(1)_D$ charge operator, of which the charge is $+q_d$ for χ and $-q_d$ for χ^c .

After SSB, ϕ_S develops a vacuum expectation value given by $\langle \phi_S \rangle = v_S/\sqrt{2}$. The mass term for the dark fermion in the Lagrangian is given by

$$\mathcal{L}_m = \mathcal{L}_m^D + \mathcal{L}_m^M, \quad (12)$$

where the Dirac mass part is

$$\begin{aligned} -\mathcal{L}_m^D &= \frac{m_D}{2} (\bar{\chi}\chi + \bar{\chi}^c \chi^c) \\ &= \frac{m_D}{2} (\bar{\chi}_R \chi_L + \bar{\chi}_R \chi_L + \bar{\chi}_R^c \chi_L^c + \bar{\chi}_R^c \chi_L^c), \end{aligned} \quad (13)$$

and the Majorana mass part is

$$\begin{aligned} -\mathcal{L}_m^M &= \frac{fv_S}{2} (\bar{\chi}^c \chi + \bar{\chi} \chi^c) \\ &= \frac{fv_S}{2} (\bar{\chi}_R^c \chi_L + \bar{\chi}_L \chi_R^c + \bar{\chi}_L^c \chi_R + \bar{\chi}_R \chi_L^c). \end{aligned} \quad (14)$$

Here we take f to be positive and $fv_S \gg m_D$. Note that through this paper, we adopt the notations¹ $\chi_L^c \equiv (\chi^c)_L = (\chi_R)^c$ and $\chi_R^c \equiv (\chi^c)_R = (\chi_L)^c$. Regarding the condition that the Majorana mass is much larger than the Dirac mass, the mass eigenstates, obtained by diagonalizing the mass matrix, split into two nearly degenerate Majorana levels, forming an inelastic Majorana pair with two mass eigenvalues,

$$m_{\pm} = fv_S \pm m_D, \quad (15)$$

which correspond to the physical Majorana fermions,

$$\chi_+ = \frac{1}{\sqrt{2}}(\chi_L + \chi_R + \chi_R^c + \chi_L^c) \quad \text{and} \quad \chi_- = \frac{1}{\sqrt{2}}(-\chi_L + \chi_R - \chi_R^c + \chi_L^c), \quad (16)$$

respectively. Appendix A contains the relevant derivation. Rewriting Eq. (11) in terms of the mass basis, the Lagrangian \mathcal{L}_χ is given by

$$\begin{aligned} \mathcal{L}_\chi = & \frac{i}{2}(\bar{\chi}_+ \gamma_\mu \partial^\mu \chi_+ + \bar{\chi}_- \gamma_\mu \partial^\mu \chi_-) - \frac{1}{2}g_\chi Z'^\mu (\bar{\chi}_+ \gamma_\mu \gamma_5 \chi_- + \bar{\chi}_- \gamma_\mu \gamma_5 \chi_+) \\ & - \frac{1}{2}[m_+ \bar{\chi}_+ \chi_+ + m_- \bar{\chi}_- \chi_-] - \frac{f}{2}(S \cos \alpha + H \sin \alpha)(\bar{\chi}_+ \chi_+ + \bar{\chi}_- \chi_-). \end{aligned} \quad (17)$$

C. The gauge boson sector

We generically assume that residual kinetic mixings between Z' and A and between Z' and Z , resulting from interactions at some high-energy scale, already exist after spontaneous electro-weak and $U(1)_{L_\mu-L_\tau}$ symmetry breaking. As a result, the neutral gauge boson sector of the Lagrangian reads

$$\begin{aligned} \mathcal{L}_{\text{gauge}} = & -\frac{1}{4}\hat{Z}_{\mu\nu}\hat{Z}^{\mu\nu} - \frac{1}{4}\hat{F}_{\mu\nu}\hat{F}^{\mu\nu} - \frac{1}{4}\hat{Z}'_{\mu\nu}\hat{Z}'^{\mu\nu} + \frac{1}{2}m_Z^2\hat{Z}_\mu\hat{Z}^\mu + \frac{1}{2}m_{Z'}^2\hat{Z}'_\mu\hat{Z}'^\mu \\ & - \frac{1}{2}\epsilon_0^A\hat{Z}'_{\mu\nu}\hat{F}^{\mu\nu} - \frac{1}{2}\epsilon_0^Z\hat{Z}'_{\mu\nu}\hat{Z}^{\mu\nu}, \end{aligned} \quad (18)$$

where the covariant field strengths for \hat{Z} , \hat{A} , and \hat{Z}' are respectively given by

$$\hat{Z}_{\mu\nu} = \partial_\mu \hat{Z}_\nu - \partial_\nu \hat{Z}_\mu, \quad \hat{F}_{\mu\nu} = \partial_\mu \hat{A}_\nu - \partial_\nu \hat{A}_\mu, \quad \hat{Z}'_{\mu\nu} = \partial_\mu \hat{Z}'_\nu - \partial_\nu \hat{Z}'_\mu. \quad (19)$$

and $m_{Z'} = 2g_\chi v_S$. Here we have added “*hat*” to gauge fields to denote that they are not the mass eigenstates. In addition to the residual mixing among the gauge fields, allowing the dark gauge boson to directly couple to μ and τ lepton sectors, these neutral gauge bosons coupled to SM and dark fermions are described by the Lagrangian,

$$\mathcal{L} \supset - (g_Z J_Z^\mu, e J_\gamma^\mu, g_{\mu\tau} J_{L_\mu-L_\tau}^\mu + g_\chi J_D^\mu) \hat{\mathbf{V}}_\mu, \quad (20)$$

¹ In the literature, someones instead use $\chi_L^c \equiv (\chi_L)^c$ and $\chi_R^c \equiv (\chi_R)^c$.

where $\hat{\mathbf{V}}_\mu = (\hat{Z}_\mu, \hat{A}_\mu, \hat{Z}'_\mu)^T$ is a vector column formed by gauge fields, $J_Z^\mu = J_3^\mu - \sin^2 \theta_W J_\gamma^\mu$ is the neutral current with $J_3^\mu = \bar{\psi} \gamma^\mu P_L T^3 \psi$, $J_\gamma^\mu = \bar{\psi} \gamma^\mu Q \psi$ is the electromagnetic current with ψ being the SM fermion and Q being the corresponding electromagnetic charge operator, $g_Z \equiv e/(\sin \theta_W \cos \theta_W)$, and dark Majorana current $J_D^\mu = (1/2)(\bar{\chi}_+ \gamma_\mu \gamma_5 \chi_- + \bar{\chi}_- \gamma_\mu \gamma_5 \chi_+)$. Here, $P_L = (1 - \gamma_5)/2$ is the left-handed projector and the eigenvalue of T^3 is $\pm 1/2$ for a left-handed doublet SM fermion or 0 for an isosinglet SM fermion.

However, \hat{Z}' can still mix with the photon \hat{A} and with the \hat{Z} boson at a one-loop level due to $m_\mu \neq m_\tau$ at low energy with the scale $\mu \lesssim m_\mu$. Thus, the Lagrangian relevant to the gauge mixing, involving the one-loop corrections, is described by

$$\mathcal{L}_{\text{mix}} = -\frac{1}{2} \epsilon_A \hat{Z}'_{\mu\nu} \hat{F}^{\mu\nu} - \frac{1}{2} \epsilon_Z \hat{Z}'_{\mu\nu} \hat{Z}^{\mu\nu}, \quad (21)$$

with $\epsilon_A = \epsilon_0^A + \epsilon'_A$ and $\epsilon_Z = \epsilon_0^Z + \epsilon'_Z$, where the one-loop mixing parameters below the m_μ scale are given by

$$\epsilon'_A = -\frac{eg_{\mu\tau}}{12\pi^2} \ln\left(\frac{m_\tau^2}{m_\mu^2}\right) \simeq -\frac{g_{\mu\tau}}{69}, \quad \epsilon'_Z = \left(-\frac{1}{4} + \sin^2 \theta_W\right) \frac{1}{\sin \theta_W \cos \theta_W} \epsilon'_A, \quad (22)$$

with θ_W being the Weinberg angle which is satisfied with $\sin \theta_W = 0.231$ at the scale m_Z in the $\overline{\text{MS}}$ scheme [46].

To deal with the mixing term, we need to transform the present gauge fields into their physical states. We first diagonalize the kinetic term of the neutral gauge Lagrangian, initially written in terms of $\hat{\mathbf{V}}_\mu$, in the canonical basis, which results in the kinetic mixing terms vanishing. Using the obtained basis, we diagonalize the mass matrix to get the mass eigenvalues. As such, the physical gauge fields are redefined as $\mathbf{V}_\mu = (Z_\mu, A_\mu, Z'_\mu)^T = \mathbf{U} \hat{\mathbf{V}}_\mu$, where the transform matrix up to order of $\epsilon_{A,Z}$ is given by

$$\mathbf{U} = \begin{pmatrix} 1 & 0 & -\frac{\epsilon_Z m_{Z'}^2}{m_Z^2 - m_{Z'}^2} \\ 0 & 1 & \epsilon_A \\ \frac{\epsilon_Z m_{Z'}^2}{m_Z^2 - m_{Z'}^2} & 0 & 1 \end{pmatrix}, \quad (23)$$

and the corresponding mass squared matrix is $\text{diag}(m_Z^2, 0, m_{Z'}^2) + \mathcal{O}(\epsilon_{A,Z}^2)$. We formulate some of the detailed expressions in Appendix B to make explicit the procedure. The resultant Lagrangian describing the interactions of the physical gauge bosons coupled to the SM and dark currents can

be rewritten from Eq. (20) as

$$\begin{aligned}
\mathcal{L} &\supset -(g_Z J_Z^\mu, e J_\gamma^\mu, g_{\mu\tau} J_{L_\mu-L_\tau}^\mu + g_\chi J_D^\mu) \mathbf{U}^{-1} \mathbf{V}_\mu \\
&= -e J_\gamma^\mu A_\mu - g_Z J_Z^\mu Z_\mu - g_{\mu\tau} J_{L_\mu-L_\tau}^\mu Z'_\mu - g_\chi J_D^\mu Z'_\mu \\
&\quad + \epsilon_A e J_\gamma^\mu Z'_\mu + \epsilon_Z \frac{m_Z^2}{m_Z^2 - m_{Z'}^2} (g_{\mu\tau} J_{L_\mu-L_\tau}^\mu + g_\chi J_D^\mu) Z_\mu - \epsilon_Z \frac{m_{Z'}^2}{m_Z^2 - m_{Z'}^2} g_Z J_Z^\mu Z'_\mu + \mathcal{O}(\epsilon_{A,Z}^2). \quad (24)
\end{aligned}$$

III. THE PARAMETERS

We adopt H to be the observed Higgs resonance with mass $m_H = 125.25$ GeV, and the vacuum expectation value $v_H = 246.22$ GeV [46]. Compared with the SM, the present model contains 8 independent parameters, which are taken to be

$$m_-, \quad m_+ = m_- + \delta m, \quad m_{Z'}, \quad m_S, \quad g_{\mu\tau}, \quad g_\chi, \quad f, \quad \alpha \text{ (the mixing angle)}, \quad (25)$$

with $\delta m = 2m_D$. Our discussion of these parameters is limited to the following conditions: (i) we assume $\delta m \ll m_\mp, m_{Z'}$. We also examine how δm relates to the remnant χ_+ in current dark matter. (ii) Assuming that the experimental results of $(g-2)_\mu$ can be explained, we analyze the constraints of various current experiments on the parameter space of $g_{\mu\tau}$ and $m_{Z'}$. (iii) To ensure dark matter remains in thermal equilibrium with the SM bath before freeze-out, we assume $m_S > 2m_{Z'}$. (iv) The dark matter annihilation process, $\chi_\mp \chi_\mp \rightarrow SS$, primarily affects the evolution of DM and ultimately determines its current relic abundance. From this, the values of f and m_\mp will be derived, along with the limit for g_χ . (v) We assume that m_S is much less than m_\pm , which results in significant self-scattering of dark matter and helps address the small-scale structure issues. (vi) This model does not impose particular constraints on the mixing angle α ; however, its magnitude may be limited by other experiments.

IV. $(g-2)_\mu$ AND THE CONSTRAINTS ON PARAMETERS $g_{\mu\tau}$ AND $m_{Z'}$

The measurement of the muon anomalous magnetic moment, $a_\mu = (g-2)_\mu/2$, announced by the Muon $g-2$ Collaboration at Fermilab (FNAL) [41, 42] is in agreement with the previous Brookhaven (BNL E821) result [43]. The combined experimental average differs from the SM [44, 45] by

$$\Delta a_\mu = a_\mu(\text{exp}) - a_\mu(\text{SM}) = (24.9 \pm 4.8) \times 10^{-10}, \quad (26)$$

with a 5σ deviation. From Eq. (24), the Lagrangian for the muon current coupling with the gauge bosons, relevant to the contributions to Δa_μ , is given by

$$\begin{aligned} \mathcal{L} \supset & - (g_{\mu\tau} + e\epsilon_A + \epsilon_Z r_{ZZ'} g_V g_Z) \bar{\mu} \gamma^\mu \mu Z'_\mu - \epsilon_Z r_{ZZ'} g_A g_Z \bar{\mu} \gamma^\mu \gamma_5 \mu Z'_\mu \\ & - (g_Z g_V - \epsilon_Z (1 + r_{ZZ'}) g_{\mu\tau}) \bar{\mu} \gamma^\mu \mu Z_\mu - g_Z g_A \bar{\mu} \gamma^\mu \gamma_5 \mu Z_\mu, \end{aligned} \quad (27)$$

where $g_V = -1/4 + \sin^2 \theta_W$, $g_A = 1/4$, and $r_{ZZ'} = m_{Z'}^2 / (m_Z^2 - m_{Z'}^2)$. Using the generic formulas for neutral vector bosons coupling to muons [28], the total contribution to the anomaly in this model is evaluated as

$$\begin{aligned} \Delta a_\mu = & \frac{(g_{\mu\tau} + e\epsilon_A + \epsilon_Z r_{ZZ'} g_V g_Z)^2}{4\pi^2} \frac{m_\mu^2}{m_{Z'}^2} I_V(m_{Z'}) + \frac{(\epsilon_Z r_{ZZ'} g_A g_Z)^2}{4\pi^2} \frac{m_\mu^2}{m_{Z'}^2} I_A(m_{Z'}) \\ & + \frac{(g_Z g_V - \epsilon_Z (1 + r_{ZZ'}) g_{\mu\tau})^2}{4\pi^2} \frac{m_\mu^2}{m_Z^2} I_V(m_Z) + \frac{(g_Z g_A)^2}{4\pi^2} \frac{m_\mu^2}{m_Z^2} I_A(m_Z), \end{aligned} \quad (28)$$

with

$$I_V(m_0) = \int_0^1 dx \frac{m_0^2 x^2 (1-x)}{m_0^2 (1-x) + m_\mu^2 x^2}, \quad (29)$$

$$I_A(m_0) = \int_0^1 dx \frac{m_0^2 x (1-x) (x-4) - 2x^3 m_\mu^2}{m_0^2 (1-x) + m_\mu^2 x^2}. \quad (30)$$

In the present work, we consider the conditions satisfying $r_{ZZ'} \ll 1$, i.e., $m_{Z'}^2 \ll m_Z^2$, so that we have

$$\Delta a_\mu \simeq \frac{(g_{\mu\tau} + e\epsilon_A)^2}{4\pi^2} \int_0^1 dx \frac{m_\mu^2 x^2 (1-x)}{m_{Z'}^2 (1-x) + m_\mu^2 x^2}. \quad (31)$$

In this study, we assume that the correction to Δa_μ due to kinetic mixing between the Z' and photon fields follows the relation $e\epsilon_A \simeq e\epsilon_0^A - 0.0044 g_{\mu\tau} \ll g_{\mu\tau}$.

Fig. 1 illustrates the parameter space compatible with muon $(g-2)_\mu$ data. It highlights regions ruled out by experiments such as BABAR [47], CCFR [48, 49], white dwarf (WD) cooling [50, 51], and Borexino [30, 52]. WD cooling and Borexino results depend on the kinetic mixing parameter $\epsilon_A = -g_{\mu\tau}/69 + \epsilon_0^A$. In this study, we reevaluated the WD cooling constraint, primarily via the decay of plasmons into neutrino pairs. Within the Standard Model, the effective Lagrangian is represented by

$$\mathcal{L}_{\text{SM,eff}} = - \sum_{i=e,\mu,\tau} 2 \frac{C_V^i G_F}{\sqrt{2}} (\bar{\nu}_{i,L} \gamma^\mu \nu_{i,L}) (\bar{e} \gamma_\mu e), \quad (32)$$

where $C_V \equiv \sum_{i=e,\mu,\tau} C_V^i \simeq 0.964$. For the present model, the relevant effective Lagrangian is given by

$$\mathcal{L}_{\text{eff}} \supset - \sum_{i=\mu,\tau} (\delta_{i,\mu} - \delta_{i,\tau}) \frac{e g_{\mu\tau} \epsilon_A}{m_{Z'}^2} (\bar{\nu}_{i,L} \gamma^\mu \nu_{i,L}) (\bar{e} \gamma_\mu e), \quad (33)$$

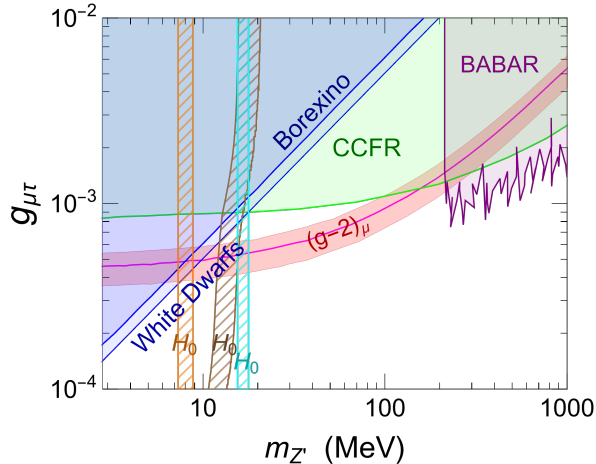


FIG. 1. The central value (magenta solid curve) and the parameter regions within 2σ (red) are determined by the muon $(g-2)_\mu$ measurements for the present iDM model with the $U(1)_{L_\mu-L_\tau}$ gauge boson Z' . Exclusions from various experiments, including BABAR [47], CCFR [48, 49], white dwarf (WD) cooling [50, 51], and Borexino [30, 52], are displayed. The hatched regions, which satisfy $3.2 < N_{\text{eff}} < 3.33$ [53], can alleviate the Hubble tension (H_0), with colors in brown, orange, and cyan representing $|\epsilon_A| = g_{\mu\tau}/69, 10^{-7}, 0$, respectively. The region to the left of the Hubble tension boundary line, where $N_{\text{eff}} > 3.33$, is disfavored by Planck 2018 data (TT, TE, EE+lowE+lensing+BAO at 95%CL) [53].

where we specify that, *e.g.*, $\delta_{i,\mu} = 1$ when $i \equiv \mu$, and 0 otherwise. Considering that extra cooling is excluded at 90% CL, this implies that $(eg_{\mu\tau}\epsilon_A/m_{Z'}^2)^2/(C_V G_F)^2 < 0.99$. This constraint can be shown as

$$g_{\mu\tau} \leq 6.1 \times 10^{-4} \times \frac{m_{Z'}}{12 \text{ MeV}} \times \left| 1 - \frac{69}{g_{\mu\tau}} \epsilon_0^A \right|^{1/2}. \quad (34)$$

Figure 1 assumes $\epsilon_0^A = 0$ for plotting WD cooling and Borexino results. The figure shows that the WD bounds are slightly tighter than those from Borexino. It is important to note that, even if the condition $e\epsilon_A \ll g_{\mu\tau}$ is satisfied, a small kinetic mixing effect from interactions at high-energy scales can substantially impact the interpretation of both WD cooling and Borexino data.

The hatched areas, where $3.2 < N_{\text{eff}} < 3.33$, could help resolve the disagreement between cosmological and local Hubble constant measurements, known as the Hubble tension (H_0). These regions are color-coded in brown, orange, and cyan, corresponding to $|\epsilon_A| = g_{\mu\tau}/69, 10^{-7}, 0$, respectively. The zone on the left of the Hubble tension boundary, with $N_{\text{eff}} > 3.33$, is disfavored by Planck 2018 data (TT, TE, EE + lowE + lensing + BAO) at 95% CL [53]. A detailed analysis of N_{eff} will be given in Sec. VI.

V. BOLTZMANN EQUATIONS AND THERMAL FREEZE-OUT

In this section, we will estimate the freeze-out parameter $x_f = m_-/T_{f_0}$ and the related DM annihilation cross section that can result in the present-day relic abundance, where T_{f_0} is the DM freeze-out temperature. We consider the nearly degenerate case $\delta m \ll m_{\pm}$. After freeze-out, the lifetime of χ_+ is determined by its 3-body decay channels, $\chi_+ \rightarrow \chi_- \nu_\mu \bar{\nu}_\mu$ and $\chi_- \nu_\tau \bar{\nu}_\tau$, depending on the values of δm and the coupling constant g_χ . The heavier Majorana fermion χ_+ could also be a dark matter candidate if its lifetime is comparable to or longer than the Universe's age. Similar to the case about coannihilations discussed in Ref. [54], the final dark matter abundance is described by the sum of number densities of all dark sector Majorana fermions,

$$n = n_{\chi_+} + n_{\chi_-}, \quad (35)$$

of which the evolution follows the Boltzmann equation,

$$\frac{dn}{dt} + 3Hn = - \sum_{i,j=\chi_{\pm}} \sum_X \langle \sigma v \rangle_{i,j \rightarrow X} (n_i n_j - n_i^{\text{eq}} n_j^{\text{eq}}), \quad (36)$$

with $X \equiv$ all possible final states. Addressing small-scale issues requires significant self-interactions among dark matter particles, facilitated by light S particles that are strongly coupled to dark matter via a large coupling constant. Therefore, we consider that the DM freeze-out process mainly occurs through $\chi_{\mp} \chi_{\mp} \rightarrow S S$, where S maintains its thermal equilibrium density at the same temperature as the SM bath primarily via the reactions, $S \leftrightarrow Z' Z'$ and $Z' \leftrightarrow \text{SM SM}$, meaning $n_S = n_S^{\text{eq}}$, until after χ_+ and χ_- freeze-out.² This property has been applied in Eq. (36). In our scenario, since the processes $\chi_{\mp} \chi_{\mp} \rightarrow Z' Z'$ and $\chi_{\mp} \chi_{\pm} \rightarrow Z' S$ are negligible, meaning their cross sections are much smaller than that of $\chi_{\mp} \chi_{\mp} \rightarrow S S$, we can further constrain the relevant coupling g_χ . We will analyze this point later. These Majorana annihilation cross sections, along with the related thermally averaged cross section formulas, are listed in Appendix D. Because we have $\delta m \ll m_{\chi_{\pm}}$, the freeze-out parameter x_f^+ for χ_+ closely matches $x_f^- \equiv x_f$, allowing us to use the approximation,

$$\frac{n_{\chi_{\pm}}}{n} \simeq \frac{n_{\chi_{\pm}}^{\text{eq}}}{n^{\text{eq}}}. \quad (37)$$

Thus, we illustrate the Boltzmann equation as

$$\frac{dn}{dt} + 3Hn = - \langle \sigma_{\text{eff}} v \rangle (n^2 - (n^{\text{eq}})^2), \quad (38)$$

² The decay widths of Z' and S , including the Higgs decaying into dark sector particles, are listed in Appendix C

where

$$\langle \sigma_{\text{eff}} v \rangle = \sum_{i,j=\chi_{\pm}} \sum_X \langle \sigma v \rangle_{i,j \rightarrow X} \frac{n_i^{\text{eq}} n_j^{\text{eq}}}{n^{\text{eq}} n^{\text{eq}}}. \quad (39)$$

We rewrite Eq. (38) in terms of the yield $Y = n/s$, which represents the ratio of n to the entropy density of the Universe, as

$$\frac{dY}{dx} = -\frac{m_-}{x^2} \left(\frac{\pi}{45G} \right)^{1/2} g_*^{1/2} \langle \sigma_{\text{eff}} v \rangle \left(Y^2 - (Y^{\text{eq}})^2 \right), \quad (40)$$

where $Y^{\text{eq}} = n^{\text{eq}}/s$, and $g_*^{1/2} \equiv \tilde{h}_{\text{eff}}/g_{\text{eff}}^{1/2}$ with $\tilde{h}_{\text{eff}} \equiv h_{\text{eff}}[1 + (1/3)(d \ln h_{\text{eff}}/d \ln T)]$. Here, h_{eff} and g_{eff} are the effective degrees of freedom (DoFs) for the Universe's total entropy and energy density, respectively, with

$$s = h_{\text{eff}}(T) \frac{2\pi^2}{45} T^3, \quad \rho = g_{\text{eff}}(T) \frac{\pi^2}{30} T^4. \quad (41)$$

Effective DoFs relevant to the QCD phase transition temperature of $T_{\text{QCD}} = 150$ MeV [55] are utilized in the analysis.

We adopt the method outlined in Refs. [56, 57] to determine the freeze-out parameter x_f and the appropriate coupling constant f related to the DM annihilation cross section that yields the current relic abundance. We define $T_{\text{fo}} (= m_-/x_f)$ as the temperature where $Y - Y^{\text{eq}} = \delta \cdot Y^{\text{eq}}$, ensuring that $d\delta/dx \ll 1$ and that δ is approximately 1. Next, we derive the approximation from Eq. (40), given by

$$\left(1 - \frac{27}{8x} - \frac{\delta_m x}{2} - \frac{29\delta_m}{16} \right) \approx x^{-1/2} e^{-x} \delta (\delta + 2) \sqrt{\frac{45}{\pi^5}} \frac{g_*^{1/2} M_{\text{pl}} m_-}{h_{\text{eff}}} g_- \langle \sigma v_{\text{eff}} \rangle, \quad (42)$$

at $x = x_f$. Here, g_- denotes the internal degrees of freedom of the Majorana fermion χ_- , $M_{\text{pl}} \equiv (8\pi G)^{-1/2}$ signifies the reduced Planck mass, and $\delta_m = m_+/m_- - 1 = \delta m/m_-$. Since x_f logarithmically depends on δ , we set $\delta = 1$ for the analysis.

The freeze-out process is dominated by annihilation $\chi_{\mp} \chi_{\mp} \rightarrow S S$, approximating the effective cross section as

$$\begin{aligned} \langle \sigma v_{\text{eff}} \rangle &\simeq \frac{1}{4} \left(\langle \sigma v \rangle_{\chi_- \chi_- \rightarrow SS} (1 + x \delta m) + \langle \sigma v \rangle_{\chi_+ \chi_+ \rightarrow SS} (1 - x \delta m) \right) \\ &\simeq \frac{1}{2} \langle \sigma v \rangle_{\chi_- \chi_- \rightarrow SS}, \end{aligned} \quad (43)$$

where

$$\langle \sigma v \rangle_{\chi_- \chi_- \rightarrow SS} \simeq \frac{9f^4}{64\pi m_-^2} x^{-1} - \frac{51f^4}{64\pi m_-^2} x^{-2}. \quad (44)$$

See Appendix D for a detailed explanation. We integrate³ Eq. (40) from freeze-out x_f to x_0 , with yields Y_f and Y_0 , respectively, considering that Y^{eq} is insignificant compared to Y . Here $x_0 = m_-/T_0$, with T_0 indicating the photon bath temperature below which DM self-interactions become too weak to maintain thermal equilibrium among themselves. The potential corrections arising from the Sommerfeld effect will be addressed separately in Sec. VIII. For $x > x_0$, the DM particles become free-streaming and non-thermal. However, they still follow a Maxwell-Boltzmann distribution, $f_{\text{MB}} \propto \exp[p^2/(2m_{\text{DM}}T_{\text{DM}})]$, because the momentum redshifts as $p \propto a^{-1}$, and the DM temperature scales as $T_{\text{DM}} = T^2/T_{kd} \propto a^{-2}$.

Consequently, we get

$$-\int_{Y_f}^{Y_0} \frac{dY}{Y^2} \approx m_- \left(\frac{\pi}{45G} \right)^{1/2} \left(\int_{x_f}^{x_{kd}} g_*^{1/2} \langle \sigma v \rangle_{\chi-\chi-\rightarrow SS} \frac{dx}{2x^2} + \int_{x_{kd}}^{x_0} g_*^{1/2} \langle \sigma v \rangle_{\chi-\chi-\rightarrow SS} \frac{dx}{2x^2} \right), \quad (45)$$

where $x_{kd}(= m_-/T_{kd})$ represents the value of x at the temperature when DM kinetically decouples from the bath. Between x_f and x_{kd} , DM particles remain in kinetic equilibrium with the SM bath through elastic collisions, especially $\chi_{\pm} S \leftrightarrow \chi_{\pm} S$ even after freeze-out (refer to Appendix E for a detailed discussion); in other words, we have $T_{\text{DM}} = T$. Both S and Z' stay in thermal equilibrium with the (ν_{μ}, ν_{τ}) bath through interactions such as $S \leftrightarrow Z'Z'$ and $Z' \leftrightarrow \nu_{\mu}\bar{\nu}_{\mu}, \nu_{\tau}\bar{\nu}_{\tau}$. Additionally, as will be explained in Sec. VI and shown in Fig. 4, the process $Z' \leftrightarrow e^+e^-$ maintains $T = T_{\nu_{\mu}}$ until the temperature drops below m_e . It is observed that χ_{\pm} , with masses ranging from a few GeV to several hundred GeV, kinetically decouple from the scalar field S at a temperature (T_{kd}) roughly between 210 and 250 MeV. All relevant details are available in Appendix E. When $T < T_{kd}$, the dark matter's temperature T_{DM} instead decreases as $a^{-2} \propto T^2$, i.e., $T_{\text{DM}} = T^2/T_{kd}$.

Since the annihilation rate of dark matter is nearly negligible at $x = x_0$, we can use Y_0 as its current value. The left side of Eq. (45) is roughly Y_0^{-1} because $Y_f \gg Y_0$, while the integral on the right side is mainly influenced by the region near x_f , making it insensitive to the value of x_0 . The DM relic abundance [46] is related to Y_0 with

$$\Omega_{\text{DM}} \simeq \frac{m_- Y_0 s_0}{\rho_c} \simeq 0.1200/h^2, \quad (46)$$

where $\rho_c = 1.0537 \times 10^{-5} h^2 (\text{GeV}/c^2) \text{cm}^{-3}$ is the critical density with $h \simeq 0.674$, and $s_0 = 2891.2 \text{ cm}^{-3}$ is the entropy density today. From Eqs. (42) and (45), we numerically compute x_f and the coupling constant f as functions of m_- using the DM relic abundance detailed in Eq. (46). We examine the scenario where $m_{\pm} \gg m_{Z'}$ and the scalar S is located in the range

³ This discussion is general and does not distinguish between χ_+ or χ_- . To differentiate them, one must further consider the decoupling of χ_+ from χ_- when the annihilation rate of $\chi_+\chi_+ \rightarrow \chi_-\chi_-$ drops below the Hubble expansion rate, followed by the non-equilibrium decay of χ_+ to χ_- . See Sec. VII for more details.

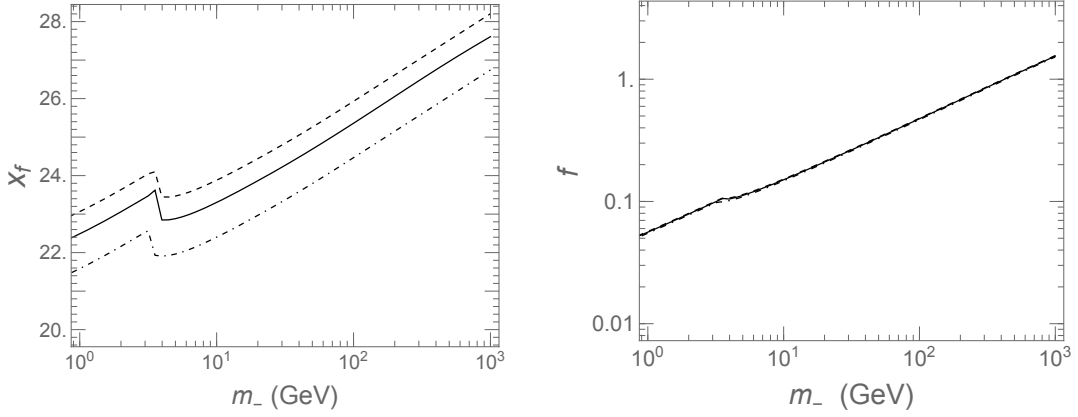


FIG. 2. Left panel: x_f as a function of m_- . Right panel: The coupling constant f that can produce the correct DM relic density as a function of m_- . The solid curve corresponds to $\delta = 1$, while the dashed and dotdashed curves are for $\delta = 1.5$ and 0.5 , respectively. The unsmooth part of the curves is due to the QCD phase transition at $T_{\text{QCD}} = 150$ MeV.

of $12 \text{ MeV} \lesssim m_S \lesssim 400 \text{ MeV}$, while also fulfilling the condition $m_S \gtrsim 2m_{Z'}$. The outcomes are illustrated in Fig. 2 for $m_- \in (1, 1000) \text{ GeV}$. For a comparative analysis, when δ is ± 0.5 , we find that the uncertainty in f is roughly less than 1%, meaning the corresponding error of $\langle\sigma v\rangle_{\chi-\chi\rightarrow SS}$ is below 5%. Generally, the reactions $\chi_{\mp}\chi_{\mp} \rightarrow Z'Z'$ and $\chi-\chi_{\pm} \rightarrow Z'S$, written as

$$\langle\sigma v\rangle_{\chi_{\mp}\chi_{\mp}\rightarrow Z'Z'} \simeq \frac{g_{\chi}^4}{16\pi m_-^2} \left\{ 1 + 3 \left(\frac{f m_-}{g_{\chi} m_{Z'}} \right)^2 \left[1 - \frac{8}{3} \frac{g_{\chi} m_-}{f m_{Z'}} + \frac{8}{3} \left(\frac{g_{\chi} m_-}{f m_{Z'}} \right)^2 \right] x^{-1} \right\}, \quad (47)$$

$$\langle\sigma v\rangle_{\chi-\chi_{\pm}\rightarrow Z'S} \simeq \frac{\delta m^2 g_{\chi}^2 f^2}{32\pi m_-^4} + \frac{g_{\chi}^2 f^2}{4\pi m_{Z'}^2} x^{-1}, \quad (48)$$

are mainly driven by the p -wave component. In the first reaction, its p -wave term is enhanced by the factor $(f m_- / (g_{\chi} m_{Z'}))^2$, while in the second, the s -wave contribution is reduced because $\delta m \ll m_-$. For the s -wave, the former is less than $10^{-14} \text{ GeV}^{-2}$ for $g_{\chi} < g_{\mu\tau}$ and $m_- > 1 \text{ GeV}$. To have $\langle\sigma v\rangle_{\chi_{\mp}\chi_{\mp}\rightarrow SS}$ be dominant over the other cross sections at freeze-out $x = x_f$, for which the value with $\delta = 1$ shown in the left panel of Fig. 2 is used, we find that it can be realized by a value of $g_{\mu\tau}/g_{\chi}$ which may be much larger than 1, depending on $m_{Z'}$ and m_- . The results are depicted in Fig. 3, where we do not show the results for $\chi_{\mp}\chi_{\pm} \rightarrow \mu^+\mu^-, \nu_{\mu}\bar{\nu}_{\mu}, \tau^+\tau^-, \nu_{\tau}\bar{\nu}_{\tau}$, of which their cross sections are less than $10^{-16} \text{ GeV}^{-2}$, much smaller the other channels in the interesting region. In Appendix D, we provide the complete forms of the relevant cross sections.

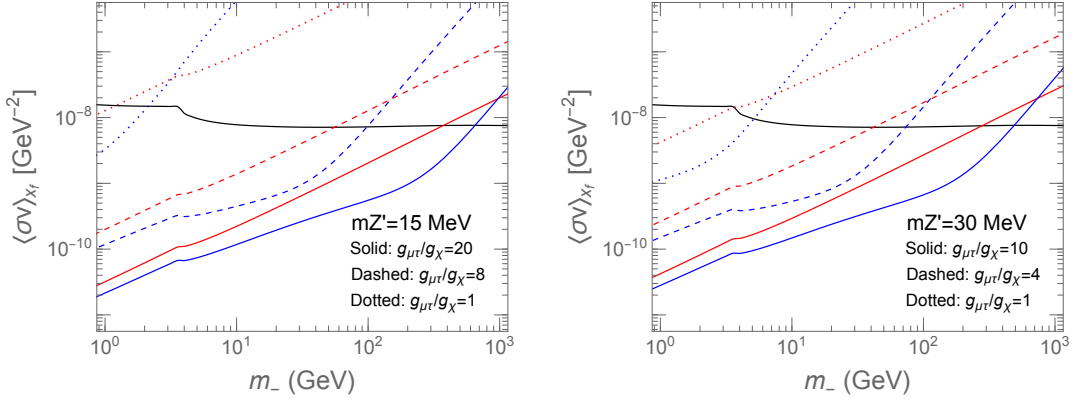


FIG. 3. Thermally averaged annihilation cross sections for processes, $\chi_{\mp}\chi_{\mp} \rightarrow SS$ (black), $\chi_{-}\chi_{+} \rightarrow Z'S$ (red), and $\chi_{\mp}\chi_{\mp} \rightarrow Z'Z'$ (blue), where the freeze-out temperature parameter x_f corresponding to the value shown in Fig. 2 with $\delta = 1$ is adopted.

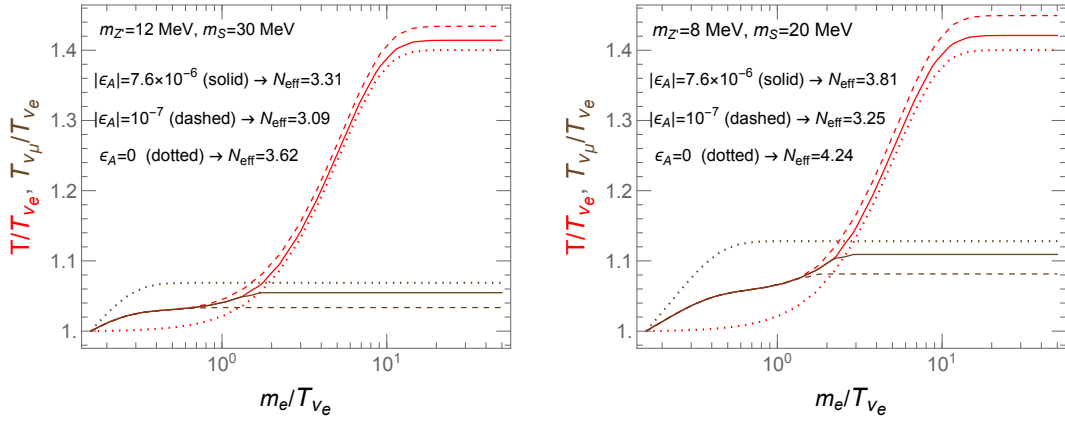


FIG. 4. The evolution of the ratios T/T_{ν_e} (red) and $T_{\nu_{\mu}}/T_{\nu_e}$ (brown) for $|\epsilon_A| = 7.6 \times 10^{-6}$ (solid line), 10^{-7} (dashed line), and 0 (dotted line), with $m_{Z'} = 12$ MeV and $m_S = 30$ MeV in the left panel, and $m_{Z'} = 8$ MeV and $m_S = 20$ MeV in the right panel. The resulting N_{eff} value is also given.

VI. CONSTRAINT FROM EFFECTIVE NUMBER OF RELATIVISTIC SPECIES AND HUBBLE TENSION

During thermal evolution, the decay rates of $S \rightarrow Z'Z'$ and $Z' \rightarrow \nu_{\mu}\bar{\nu}_{\mu}, \nu_{\tau}\bar{\nu}_{\tau}$, are greater than the Hubble expansion rate. As a result, S and Z' remain in thermal equilibrium with μ - and τ -neutrinos, maintaining a zero chemical potential even after neutrinos decouple from photons. However, due to residual kinetic mixing between Z' and the electromagnetic field, Z' can decay

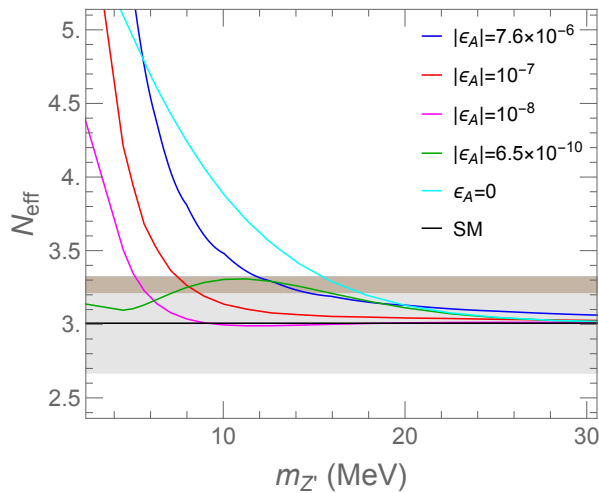


FIG. 5. N_{eff} as a function of $m_{Z'}$ values for several settings of the kinetic mixing parameter, $|\epsilon_A|$, with the Standard Model (SM) value marked by the black line. The shaded gray and brown areas represent the constraints of $N_{\text{eff}} = 2.99^{+0.34}_{-0.33}$ from Planck TT, TE, EE + lowE + lensing + BAO at a 95% confidence level. The brown region, where $3.2 < N_{\text{eff}} < 3.33$, hints at a potential reduction in the Hubble tension.

into an e^+e^- pair, with the decay width,

$$\Gamma_{Z' \rightarrow e^+e^-} = \frac{\alpha \epsilon_A^2 m_{Z'}}{3} \left(1 + \frac{2m_e^2}{m_{Z'}^2}\right) \left(1 - \frac{4m_e^2}{m_{Z'}^2}\right)^{1/2}. \quad (49)$$

Since the DoFs of S and Z' are ultimately integrated into the SM bath, these effects can impact the effective number of relativistic species, N_{eff} . This parameter is defined based on the total radiation energy density, ρ_t , and the photon density, ρ_γ , as

$$\frac{\rho_t}{\rho_\gamma} = 1 + N_{\text{eff}} \frac{7}{8} \left(\frac{4}{11}\right)^{4/3}. \quad (50)$$

Before electron neutrino-photon decoupling, all neutrinos stay in thermal equilibrium with photon-coupled particles through weak interactions with e^\pm and via $Z' \leftrightarrow e^+e^-$. About one second after the Big Bang, when the weak interaction rate falls below the expansion rate of the universe, its corresponding temperature is estimated to be around $T \approx 3.2$ MeV [32]. From this point forward, interactions among these three groups of particles— (γ, e^\pm) , (ν_e) , and (ν_μ, ν_τ) —mainly originate from $Z' \leftrightarrow e^+e^-$, which results in the transfer of entropy among them. To clarify, we define three temperatures: T , T_{ν_e} , and T_{ν_μ} , corresponding to the sets (γ, e^\pm) , (ν_e) , and (ν_μ, ν_τ) , respectively. When the temperature drops below approximately 3.2 MeV, we can estimate the neutrino-to-photon temperature ratio and N_{eff} by analyzing the separate evolution of the comoving entropy

densities [30], as described by

$$\frac{1}{a^3} \frac{d}{dt} \left(s_\gamma(T) a^3 + 2s_e(T) a^3 \right) = \frac{1}{T} \left(\langle \Gamma_{Z' \rightarrow e^+ e^-} \rangle_{T_{\nu_\mu}} \rho_{Z'}(T_{\nu_\mu}) - \langle \Gamma_{Z' \rightarrow e^+ e^-} \rangle_T \rho_{Z'}(T) \right), \quad (51)$$

$$\begin{aligned} \frac{1}{a^3} \frac{d}{dt} \left(2s_{\nu_\mu}(T_{\nu_\mu}) a^3 + 2s_{\nu_\tau}(T_{\nu_\mu}) a^3 + s_S(T_{\nu_\mu}) a^3 + s_{Z'}(T_{\nu_\mu}) a^3 \right) \\ = -\frac{1}{T_{\nu_\mu}} \left(\langle \Gamma_{Z' \rightarrow e^+ e^-} \rangle_{T_{\nu_\mu}} \rho_{Z'}(T_{\nu_\mu}) - \langle \Gamma_{Z' \rightarrow e^+ e^-} \rangle_T \rho_{Z'}(T) \right), \end{aligned} \quad (52)$$

$$a^3 \frac{d}{dt} \left(2s_{\nu_e}(T_{\nu_e}) a^3 \right) = 0, \quad (53)$$

where the thermally averaged width of Z' at temperature T_i is given by

$$\langle \Gamma_{Z' \rightarrow e^+ e^-} \rangle_{T_i} = \Gamma_{Z'} \frac{K_1(m_{Z'}/T_i)}{K_2(m_{Z'}/T_i)}, \quad (54)$$

and the evolution of the scale factor a is determined by the Hubble rate,

$$\frac{\dot{a}}{a} = \frac{\sqrt{\rho_\gamma(T) + 2(\rho_e(T) + \rho_{\nu_e}(T_{\nu_e}) + \rho_{\nu_\mu}(T_{\nu_\mu}) + \rho_{\nu_\tau}(T_{\nu_\mu})) + \rho_S(T_{\nu_\mu}) + \rho_{Z'}(T_{\nu_\mu})}}{\sqrt{3} M_{\text{pl}}}. \quad (55)$$

Here, s_a and ρ_a represent the entropy density and the thermal equilibrium (with zero chemical potential) for particle a , respectively. The factor of "2" preceding them accounts for its antiparticle. In the right-hand side of Eqs. (51) and (52), we have applied the detailed balance condition, which states that the rate of thermal heat transfer via $e^+ e^- \rightarrow Z'$ at temperature T equals $\langle \Gamma_{Z' \rightarrow e^+ e^-} \rangle_T \rho_{Z'}(T)$.

Figure 4 shows the behavior of temperature ratios T/T_{ν_e} and T_{ν_μ}/T_{ν_e} using different values for the kinetic mixing parameter $|\epsilon_A| = 7.6 \times 10^{-6}$ (which corresponds to using $\epsilon_A = -[eg_{\mu\tau}/(12\pi^2) \ln(m_\tau^2/m_\mu^2)]$ with $g_{\mu\tau} = 5.2 \times 10^{-4}$), 10^{-7} , and 0, with $m_{Z'} = 12$ MeV and $m_S = 30$ MeV, while in the right panel, $m_{Z'} = 8$ MeV and $m_S = 20$ MeV. For a Z' - γ kinetic mixing parameter $|\epsilon_A| > 10^{-8}$, the $Z' \leftrightarrow e^+ e^-$ interaction helps equilibrate the (γ, e^\pm) and $(\nu_\mu, \nu_\tau, S, Z')$ baths, maintaining $T = T_{\nu_\mu}$ until $T < m_e$. As the temperature drops, entropy from S and Z' is shared between these two baths. A larger $|\epsilon_A|$ extends the equilibrium period, causing T_{ν_μ}/T_{ν_e} to increase and T/T_{ν_e} to decrease.

On the other hand, for $|\epsilon_A| < 10^{-8}$, the baths decouple at a temperature of approximately 3.2 MeV, below which weak interactions cannot maintain temperature equilibrium among them. In this condition, an even smaller $|\epsilon_A|$ results in less entropy being transferred to the (γ, e^\pm) bath, while the eaten S and Z' further increase T_{ν_μ} when $T < m_e$.

In Fig. 5, we plot the resulting N_{eff} versus $m_{Z'}$ during the later stage of the Big Bang Nucleosynthesis (BBN) epoch, where we have adopted $m_S = 2m_{Z'} + 5$ MeV. The obtained N_{eff} is insensitive to m_S for our consideration of $m_S > 2m_{Z'}$. In Figs. 1 and 5, we show the results, accounting for

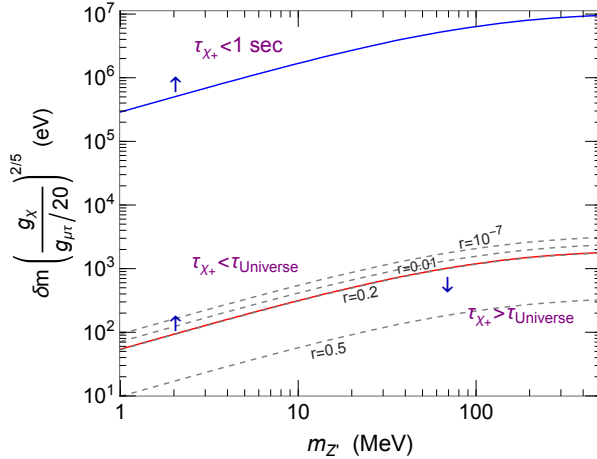


FIG. 6. Contours of the lifetime (τ_+) of χ_+ as a function of $m_{Z'}$ and δm , where the upper solid blue line indicates $\tau_+ = 1$ second, and the lower solid red line corresponds to $\tau_+ = 13.79$ billion years, the age of the Universe. The DM mass difference $\delta m = m_+ - m_-$ is shown with a reference value $g_\chi = g_{\mu\tau}/20$. Several values for the fraction of the χ_+ number density abundance at present, $r = n_+/(n_+ + n_-)$, are indicated as gray dashed lines.

$3.2 < N_{\text{eff}} < 3.33$, which can help alleviate the tension between cosmological and local observations of the Hubble constant [58, 59]. Under the constraint of $N_{\text{eff}} < 3.33$ from Planck (TT, TE, EE + lowE + lensing + BAO at 95% CL) [53], we find $m_{Z'} \gtrsim 12$ MeV for $|\epsilon_A| = 7.6 \times 10^{-6}$, and $m_{Z'} \gtrsim 7.5$ MeV for $|\epsilon_A| = 10^{-7}$. For much smaller $|\epsilon_A|$, e.g., 6.5×10^{-10} , an even wider mass range, $6.9 \text{ MeV} < m_{Z'} < 16.9 \text{ MeV}$, can help relax the Hubble tension, whereas for $\epsilon_A = 0$, the favored value shifts to higher masses. Before proceeding, it is worth noting that neutrino oscillations imply rapid changes in neutrino flavor, which may equilibrate the temperatures $T_{\nu_e} \simeq T_{\nu_\mu}$. Such effects might further slightly alter the N_{eff} [32].

VII. EXCITED STATE LIFETIME, MASS SPLITTING, AND EXCITED STATE FRACTION FOR NEARLY DEGENERATE DARK MATTER

For nearly degenerate DM, where $\delta m (= m_+ - m_-) \ll m_\pm$, the decay of χ_+ mainly occurs via three-body channels: $\chi_+ \rightarrow \chi - \nu_\mu \bar{\nu}_\mu$ and $\chi_+ \rightarrow \chi - \nu_\tau \bar{\nu}_\tau$, mediated by a virtual Z' boson. The decay width is approximately

$$\Gamma_{\chi_+} \simeq \frac{g_{\mu\tau}^4}{10\pi^3 m_{Z'}^4} \left[\delta m \left(\frac{g_\chi}{g_{\mu\tau}/20} \right)^{2/5} \right]^5. \quad (56)$$

This approximation is independent of m_- . Fig. 6 shows three regions separated by a χ_- lifetime of 1 second and the age of the universe within the parameter space of δm and $m_{Z'}$. When plotting the contour graph, we used the $g_{\mu\tau}$ value that matches the $(g-2)_\mu$ experimental results and considered $g_\chi = g_{\mu\tau}/20$ as a reference. This ensures that $\chi_\pm\chi_\pm \rightarrow SS$ is the main reaction for producing relic dark matter (see Fig. 3).

Since χ_+ mainly decays into muon and tauon neutrinos, the constraints from BBN and the cosmic microwave background (CMB) are less strict. In any case, in the $\tau_+ < 1$ sec region, since the decay of χ_+ occurs before neutrinos and photons decouple, this can prevent deviation from the BBN constraints [60]. This paper does not address the case of $\tau_+ \sim 1$ sec, which relates to δm around MeV (see Fig. 6). In the region where $\tau_+ \gg 1$ sec, because the contribution to ΔN_{eff} from χ_+ decay is minimal, we exclude its calculation and will not discuss it further.

Before analyzing the residual after χ_+ decay, we review dark matter's evolution post-freeze-out. The Universe's age is roughly H^{-1} , and Figs. 15 and 14 show the timelines for chemical decoupling of χ_+ and χ_- , as well as for dark matter's kinetic energy decoupling via S and the SM thermal bath. These decouplings happen at $t \ll 1$ sec. After chemical decoupling, dark matter stays at the SM bath temperature through S scattering. Kinetic decoupling from S occurs at $T \approx 210 - 250$ MeV, after which T_{DM} drops proportionally to T^2 . References for the decoupling processes can be found in Appendices F and E.

Below, we will provide a more accurate estimate of the residual fraction of the excited-state relic, χ_+ , after its decay. The differential equation,

$$d(a^3 n_{\chi_+}) \simeq -\frac{a^3 n_{\chi_+}}{\tau_+} dt, \quad (57)$$

describes the change in the number density of χ_+ due to its decay, where $\tau_+ = 1/\Gamma_{\chi_+}$ is the lifetime of χ_+ . The solution satisfies

$$n_{\chi_+} = n_{\chi_+,i} \left(\frac{a_i}{a}\right)^3 e^{-(t-t_i)/\tau_+}, \quad (58)$$

where t_i and a_i represent the time point and the corresponding scaling factor, respectively, when χ_+ and χ_- are chemically decoupled. Because χ_+ decays to χ_- , the comoving number of χ_- increases, and its number density can be written as

$$n_{\chi_-} = n_{\chi_-,i} \left(\frac{a_i}{a}\right)^3 + n_{\chi_+,i} \left(\frac{a_i}{a}\right)^3 \left(1 - e^{-(t-t_i)/\tau_+}\right). \quad (59)$$

Moreover, the number densities follow the relation $n_{\chi_\pm} \propto a^3$ between the freeze-out time and t_i ,

and they match the thermal equilibrium Boltzmann distribution at freeze-out,

$$n_{\chi_{\pm}}(T_{\text{fo}}) = g_{\pm} \left(\frac{m_{\pm} T_{\text{fo}}}{2\pi} \right)^3 e^{-m_{\pm}/T_{\text{fo}}}, \quad (60)$$

where $g_+ = 2$ and $g_- = 2$ represent the internal degrees of freedom for χ_+ and χ_- , respectively. Therefore, once χ_+ and χ_- are decoupled, the decay of χ_+ influences its fraction in dark matter, leading to the following result,

$$r(t) = \frac{n_{\chi_+}}{n_{\chi_+} + n_{\chi_-}} \simeq \frac{e^{-(t-t_i)/\tau_+}}{1 + e^{\delta m/T_{\text{fo}}}} \simeq \frac{1}{2} e^{-(t-t_i)/\tau_+}, \quad (61)$$

where the decoupling time, t_i , is proportional to H^{-1} and is approximately 10^{-8} to 10^{-6} seconds, as shown in Fig. 15; see the detailed discussions in Appendix F.

The value of r depends on the mass splitting, δm , of dark matter. Fig. 6 shows contour lines for $r = 0.5, 0.2, 0.01$, and 10^{-7} at the current time. A smaller δm results in a larger χ_+ residual fraction. As indicated in the figure, if δm remains below 5 keV, a significant portion of χ_+ might be present. Since dark matter density is significantly higher near galaxy centers, the annihilation processes $\chi_+\chi_- \rightarrow \mu^+\mu^-, \tau^+\tau^-$ could happen at a much greater rate in these regions. Detecting the photon spectrum produced by this process can help confirm whether it originates from such an annihilation, thereby testing this model.

In Sec. X, we analyze how different values of δm influence the average dark matter self-interaction, as shown in Figs. 11 and 12. Sec. XI will further discuss the inelastic DM scattering signal related to δm and evaluate its detectability in direct detection experiments or neutron-star capture. Additionally, Sec. XI will investigate the possibility of increasing the χ_+ number density at galaxy centers through inelastic upscattering.

VIII. SOMMERFELD EFFECTS ON THERMAL RELIC ABUNDANCE AND DARK MATTER ANNIHILATION

The Sommerfeld enhancement could affect dark matter annihilation rates, potentially altering the relic density and the signals detected indirectly. Below, we examine how the Sommerfeld effect impacts each case individually.

A. Dark matter relic density

In Sec. V, we ignored the Sommerfeld effect when calculating the yield, Y , of dark matter. When the DM particles become non-relativistic, the thermally annihilating cross-section is

$$\langle \sigma v \rangle_{\chi\text{-}\chi\text{-}\rightarrow SS} = \int S_1 \cdot (\sigma v) f_r(v) dv, \quad (62)$$

where the tree-level cross section,

$$(\sigma v)_{\chi\mp\chi\mp\rightarrow SS} \simeq \frac{3f^4}{128\pi m_{\mp}^2} v^2, \quad (63)$$

with a Sommerfeld enhancement factor, S_1 , is dominated by the p -wave component in the partial-wave expansion, and, in terms of the relative velocity (v), the probability density function of the two incident particles in the center-of-mass frame is given by

$$f_r(v) = \sqrt{\frac{2}{\pi}} \frac{v^2}{v_0^3} e^{-\frac{v^2}{2v_0^2}} = \sqrt{\frac{2}{\pi}} \left(\frac{x_-}{2}\right)^{3/2} v^2 e^{-\frac{x_- v^2}{4}}, \quad (64)$$

with $x_- = m_-/T_{\text{DM}}$ and the most probable velocity being

$$v_0 = \sqrt{\frac{2T_{\text{DM}}}{m_-}}. \quad (65)$$

Summing the ladder diagrams in the calculation increases the square of the scattering amplitude by a so-called Sommerfeld factor. Considering the DM annihilation process in the center-of-mass frame, the initial DM particles are \vec{p} and $-\vec{p}$, while the final S particles possess momenta of \vec{p}' and $-\vec{p}'$. Generally, a full amplitude, A , that includes the Sommerfeld effect, is represented by an integral involving the wave function $\phi_{\vec{p}}^*(\vec{r})$ and the bare scattering amplitude, A_0 [61, 62],

$$A(\vec{p}, \vec{p}') = \int d^3r \phi_{\vec{p}}^*(\vec{r}) \int \frac{d^3q}{(2\pi)^3} e^{i\vec{q}\cdot\vec{r}} A_0(\vec{q}, \vec{p}'), \quad (66)$$

where we can further expand A , A_0 , and $\phi_{\vec{p}}^*(\vec{r})$ in partial waves,

$$A(\vec{p}, \vec{p}') = \sum_{\ell} A_{\ell}(\vec{p}, \vec{p}') = \sum_{\ell} p^{\ell} p'^{\ell} P_{\ell}(\hat{p} \cdot \hat{p}') a_{\ell}, \quad (67)$$

$$A_0(\vec{q}, \vec{p}') = \sum_{\ell} A_{0\ell}(\vec{q}, \vec{p}') = \sum_{\ell} q^{\ell} p'^{\ell} P_{\ell}(\hat{q} \cdot \hat{p}') a_{0,\ell}, \quad (68)$$

$$\phi_{\vec{p}}^*(\vec{r}) = \frac{1}{p} \sum_{\ell} i^{\ell} (2\ell + 1) e^{i\delta_{\ell}} P_{\ell}(\hat{p} \cdot \hat{r}) \frac{\chi_{p,\ell}(\alpha_f m_- r)}{r C_{\ell}}, \quad (69)$$

with $\alpha_f = f^2/(4\pi)$ and the symbols with hats denoting the corresponding unit vectors. Here, the wave function $\chi_{p,\ell}$ satisfies the differential equation,

$$\frac{1}{m_-} \frac{d^2}{dr^2} \chi_{p,\ell} - \frac{\ell(\ell+1)}{m_- r^2} \chi_{p,\ell} + \frac{p^2}{m_-} \chi_{p,\ell} - V(r) \chi_{p,\ell} = 0, \quad (70)$$

where in the coordinate space the DM interaction through the exchange of S can be described by the Yukawa potential,

$$V(r) = -\frac{\alpha_f e^{-m_S r}}{r}. \quad (71)$$

Using the dimensionless variable $x = \alpha_f m_- r$, we can express Eq. (70) as

$$\frac{d^2}{dx^2} \chi_{p,\ell} - \frac{\ell(\ell+1)}{x^2} \chi_{p,\ell} + a^2 \chi_{p,\ell} + \frac{e^{-x/b}}{x} \chi_{p,\ell} = 0, \quad (72)$$

where

$$a = \frac{v}{2\alpha_f}, \quad b = \frac{\alpha_f m_-}{m_S}. \quad (73)$$

Following a similar derivation as in Refs. [61, 62], we obtain the ℓ -wave partial amplitude from Eq. (66),

$$A_\ell(\vec{p}, \vec{p}') \simeq \sqrt{S_\ell} A_0(\vec{p}, \vec{p}'), \quad (74)$$

where the Sommerfeld enhancement is given by

$$S_\ell = \left| \frac{(2\ell+1)!!}{C_\ell} \left(\frac{2\alpha_f}{v} \right)^{\ell+1} \right|^2. \quad (75)$$

The constant C_ℓ can be determined by

$$C_\ell^2 = [\chi_{p,\ell}(x)^2 + \chi_{p,\ell}(x - \pi/2)^2]_{|x \rightarrow \infty}. \quad (76)$$

In this paper, we consider that the DM relic density is dominated by the p -wave annihilation, $\chi_\mp \chi_\mp \rightarrow SS$. Thus, the relevant Sommerfeld factor is given by

$$S_1 = \left| \frac{3}{C_1} \left(\frac{2\alpha_f}{v} \right)^2 \right|^2. \quad (77)$$

In Sec. V, we neglected the Sommerfeld effect, which is only significant at very low velocities. The integral on the right of Eq. (45) mainly comes from a small region near $x = x_f$, where dark matter particles are still fairly relativistic. When considering this effect, we compare the ratio of the integrand at different x values to its value at $x = x_f$,

$$\frac{g_*^{1/2}(T) \langle \sigma v \rangle_{\chi-\chi \rightarrow SS}(x) / (2x^2)}{g_*^{1/2}(T_{fo}) \langle \sigma v \rangle_{\chi-\chi \rightarrow SS}(x_f) / (2x_f^2)}. \quad (78)$$

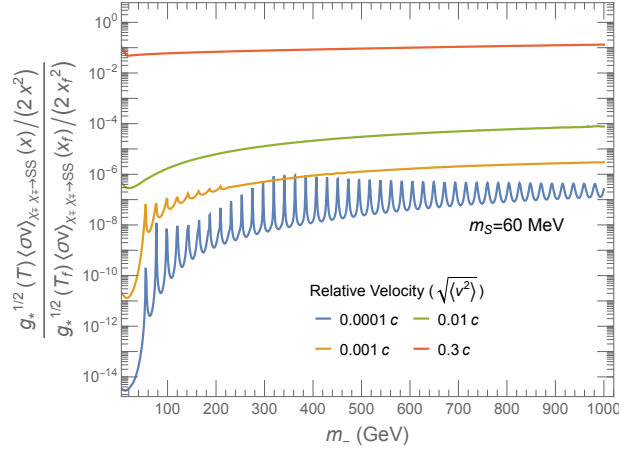


FIG. 7. Including the Sommerfeld effect, we examined the ratio of the integrand's value at different relative velocities to its value at $x = x_f$. We simply take $m_S = 60$ MeV.

These comparisons are shown in Fig. 7, examining the integrand at various relative velocities. Here, we use velocity v instead of the temperature parameter x , since dark matter becomes more non-relativistic as temperature decreases; they are related by

$$\langle v^2 \rangle = \begin{cases} \frac{6}{x}, & \text{for } x < x_{kd}, \\ \frac{6x_{kd}}{x^2} \left(\frac{h_{\text{eff}}(T)}{h_{\text{eff}}(T_{kd})} \right)^{2/3}, & \text{for } x > x_{kd}. \end{cases} \quad (79)$$

As the velocity decreases (or as x increases), the integrand drops rapidly, and this pattern continues even after considering the Sommerfeld effect. It is important to note that when the temperature falls below a certain threshold, the DM self-interaction weakens, preventing thermal equilibrium. During this period, the DM particles move freely and are non-thermal but still follow the Maxwell-Boltzmann distribution. Fig. 7 hints that for p -wave DM annihilation, even in a non-thermal state, the Sommerfeld correction has minimal impact on the relic density estimate. Therefore, including this effect does not affect the relic density results.

B. Indirect searches and constraints

Before dark matter annihilation, incident particles with low relative velocity exchange a ladder of light mediators (known as Sommerfeld enhancement), vastly boosting the annihilation rate. In Fig. 8, we display the p -wave Sommerfeld factor and its corresponding annihilation cross section for various nonrelativistic relative velocities. For low-velocity dark matter, although its tree-level annihilation cross-section σv is suppressed by v^2 , multiplying it by the Sommerfeld correction factor

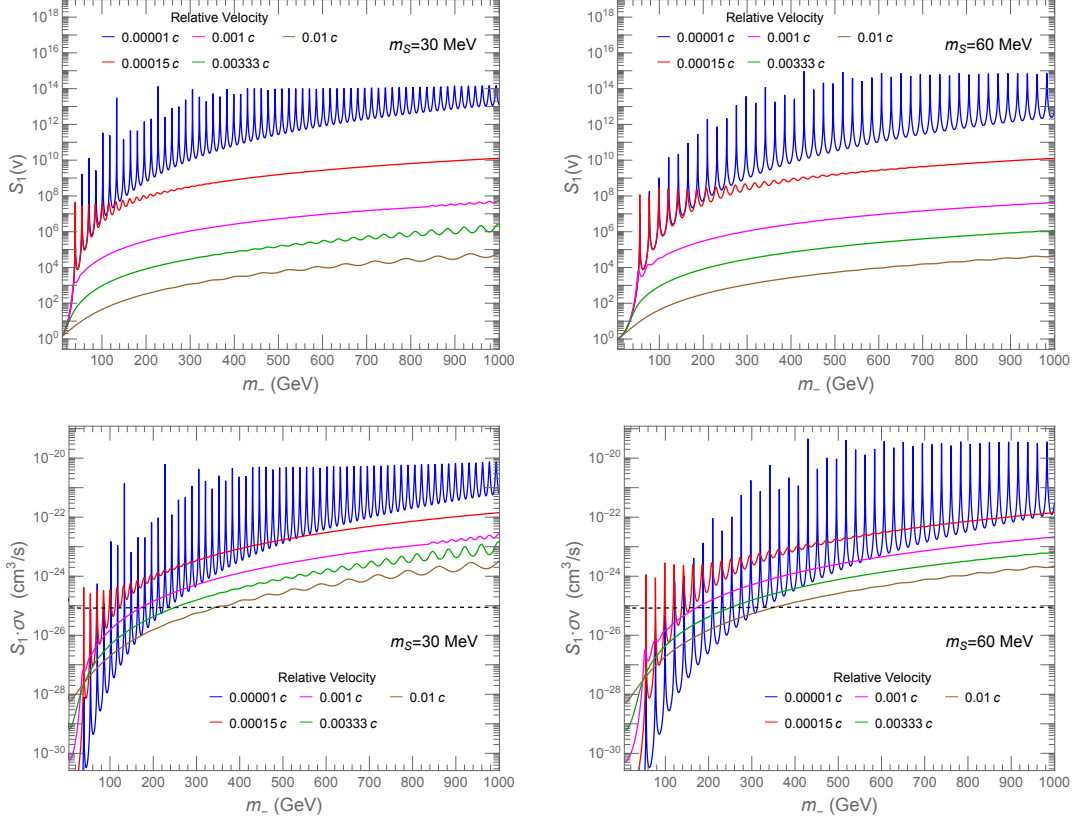


FIG. 8. The Sommerfeld enhancement factor as a function of the dark matter mass m_- for widely different values of nonrelativistically relative velocities. Also shown is the p -wave dark matter annihilation cross section with the Sommerfeld enhancement factor in the second panel, where the black dashed line indicates the value of $\langle\sigma v\rangle_{\chi-\chi-\rightarrow SS}$ at the freeze-out temperature that accounts for the thermal relic density. The mediator mass, m_S , is specified as 30 MeV (left) or 60 MeV (right).

can still result in a value significantly greater than the freeze-out $\langle\sigma v\rangle_{\chi-\chi-\rightarrow SS}$. Note that in the s -wave WIMP scenario with Majorana fermion DM, the observed relic abundance corresponds to a cross section of approximately $\langle\sigma v\rangle \sim 2 \times 10^{-26} \text{ cm}^3/\text{s}$.

In comparison with the indirect detection constraints shown in Fig. 9, we display the annihilation cross section averaged over the velocity distribution within each small-scale structure of the Universe. The left panel uses a benchmark mass of $m_S = 30 \text{ MeV}$, while the right panel uses $m_S = 60 \text{ MeV}$ for the light mediator. Here, we adopt the most probable velocities of 220, 30, 700, and 1190 km/s, which correspond to the typical scales of the local Milky Way, dwarf galaxies, galaxy groups, and galaxy clusters, respectively. The Super-Kamiokande experiment excludes the yellow area, which should only be compared to the magenta curve representing the prediction for

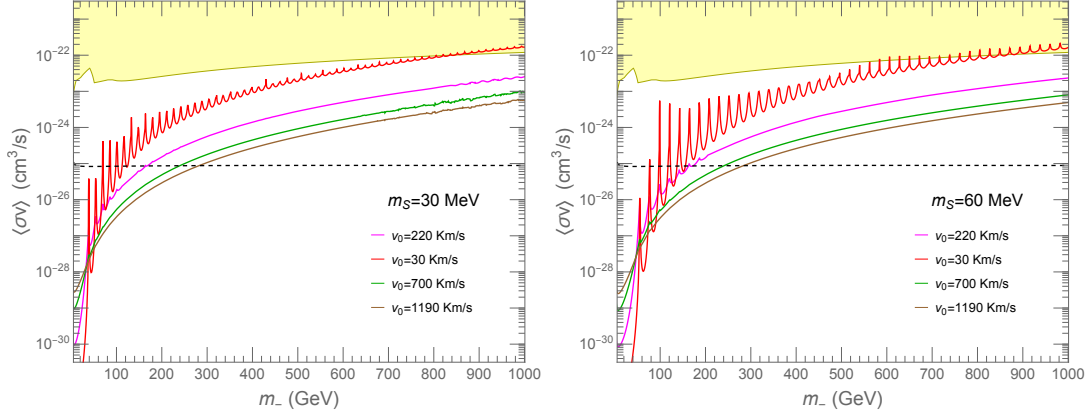


FIG. 9. The velocity-averaged annihilation cross sections. We use the most probable velocities of 220, 30, 700, and 1190 km/s, corresponding to the typical scales of the local Milky Way, dwarf galaxies, galaxy groups, and galaxy clusters, respectively. The Super-Kamiokande experiment excludes the yellow region and compares only to the magenta curve, which shows the prediction for the local Milky Way. For comparison, the left panel adopts a benchmark value of $m_S = 30$ MeV, while the right panel uses $m_S = 60$ MeV for the light mediator mass. The black dashed line represents the value of $\langle\sigma v\rangle_{\chi-\chi\rightarrow SS}$ at freeze-out temperature, which accounts for the thermal relic density.

the local Milky Way. The upper limit for muon-neutrino excess is determined using the on-off source approach of Super-Kamiokande (SK) [63, 64], based on analyses of SK-I, II, III, and IV data [65]. The maximum neutrino excess is expected in the on-source region, centered around the Galactic center, while the off-source region of the same size is located 180° away in right ascension of equatorial coordinates. Therefore, the difference in neutrino event counts (ΔN^{sig}) between these regions directly indicates DM annihilation signals. The differential muon-neutrino flux arises from a two-step annihilation process [66–69]. Initially, two DM particles annihilate into a pair of scalar mediators. Each scalar then decays into two Z' particles, with each Z' decay resulting in two neutrinos. The result can be expressed as

$$\frac{d\Phi_\nu}{dE} \simeq \frac{1}{8\pi m_-^2} \langle\sigma v\rangle_{SS} \frac{dN_\nu}{dE} \frac{1}{\Delta\Omega} \underbrace{\int_{\Delta\Omega} \int_{\text{l.o.s.}} ds \rho^2(r(s, \psi)) d\Omega}_{\text{J-factor}}, \quad (80)$$

where $\langle\sigma v\rangle_{SS} \equiv \langle\sigma v\rangle_{\chi\mp\chi\mp\rightarrow SS}$. The J-factor is calculated by integrating the DM density squared along the line of sight (l.o.s.) and over the solid angle $\Delta\Omega$ that covers the source region. The term dN_ν/dE represents the neutrino spectrum per DM annihilation. Since the neutrinos produced in DM annihilation go through intermediate steps, the spectrum from Z' decays is boosted and

becomes broader,

$$\frac{dN_\nu}{dE} = \frac{16/5}{m_- \sqrt{1 - \epsilon_2^2} \sqrt{1 - \epsilon_1^2}} \int_{t_{2,\min}}^{t_{2,\max}} \frac{dx_1}{x_1}, \quad (81)$$

where

$$\epsilon_2 = \frac{m_S}{m_-}, \quad \epsilon_1 = \frac{2m_{Z'}}{m_S}, \quad (82)$$

$$t_{2,\max} = \min \left[\frac{1}{2} \left(1 + \sqrt{1 - \epsilon_1^2} \right), \frac{2E}{\epsilon_2^2 m_-} \left(1 + \sqrt{1 - \epsilon_2^2} \right) \right], \quad t_{2,\min} = \frac{2E}{\epsilon_2^2 m_-} \left(1 - \sqrt{1 - \epsilon_2^2} \right), \quad (83)$$

$$0 \leq E \leq \frac{m_-}{4} \left(1 + \sqrt{1 - \epsilon_1^2} \right) \left(1 + \sqrt{1 - \epsilon_2^2} \right), \quad x_1 = \frac{2E_1}{m_S}, \quad (84)$$

with E , and E_1 as the neutrino energies in the center-of-mass frame of the DM pair and the S rest frame, respectively. The factor $16/5$ accounts for two effects. First, each DM annihilation produces eight neutrinos. Second, according to current oscillation parameters [70], the neutrino flux ratio observed on Earth is $1 : 2 : 2$ in the $L_\mu - L_\tau$ model [71]. Appendix G provides further details on the limit of the DM neutrino excess.

The data show neutrinos from dark matter in the Milky Way are not significantly above atmospheric background. Using the 90% C.L. upper limit for $\Delta N_{90}^{\text{sig}}$, derived from μ -like event samples in Ref. [64], we establish an upper bound on the dark matter self-annihilation cross section, $\langle \sigma v \rangle_{\chi-\chi \rightarrow SS}$, applicable to the typical velocity range of 140–280 km/s near the Galactic center. While the specific limitations of ANTARES are not detailed here [72, 73], they might restrict the mass range above 600 GeV. The model remains compatible with existing indirect detection constraints for dark matter masses ranging from 10 GeV to several hundred GeV.

IX. EXPERIMENTAL CONSTRAINTS ON THE MIXING ANGLE α

A. Particle physics experiments

Experimental events involving a light S in the final states are potentially measurable, making searches for missing energy signals from the long-lived scalar S decays outside detectors or displaced decays from beam dump experiments relevant [74–87]. In this model, the light scalar may mix with the SM Higgs. As a result, this sub-GeV hidden scalar can be produced in rare decays at colliders and fixed-target experiments. The main search for a sub-GeV scalar focuses on $K \rightarrow \pi S$, with the branching ratio depending on $\sin^2 \alpha$.

Fig. 10 shows the current experimental limits on the mixing angle in relation to the sub-GeV m_S , including reinterpretations of earlier beam-dump experiments, CHARM [74, 75] and PS191 [76–79].

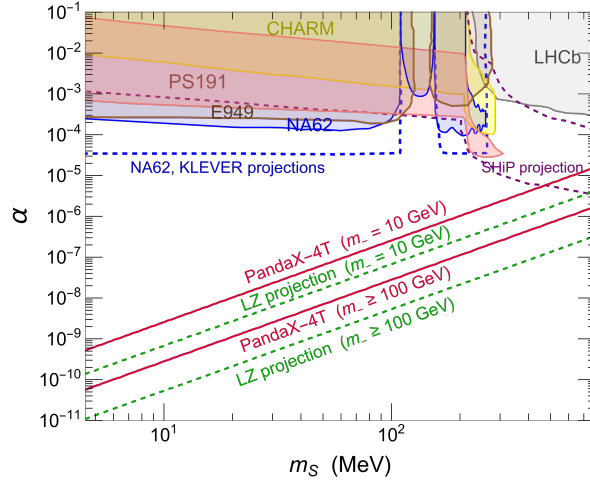


FIG. 10. Current 90% CL exclusion limits and future projections for the (m_S, α) parameter space in the sub-GeV region. Solid-colored areas with boundaries are experimentally excluded [74–82], while dashed boundaries show expected sensitivity projections [75, 83–87].

The E949 [80] and NA62 [81] experiments have placed limits on a long-lived scalar S by measuring $K^+ \rightarrow \pi^+ \bar{\nu} \nu$. In this model, a weakly interacting S can be produced in the decay $K^+ \rightarrow \pi^+ S$, sharing similar experimental characteristics with the main background process $K^+ \rightarrow \pi^+ \bar{\nu} \nu$. In the 110–155 MeV range, the decay chain $K^+ \rightarrow \pi^+ \pi^0(\gamma)$ followed by $\pi^0 \rightarrow$ invisible occurs, involving radiative photons in the final states. Assuming S escapes detection, NA62 has established constraints on the branching ratio for $K^+ \rightarrow \pi^+ S$, based on the 90% upper limit observed for $\pi^0 \rightarrow$ invisible [82].

The KLEVER project aims to measure the branching ratio of the rare decay $K_L \rightarrow \pi^0 \nu \nu$ with 20% accuracy [83]. It complements the NA62 experiment, which is expected to measure the charged mode $K^+ \rightarrow \pi^+ \bar{\nu} \nu$ with about 10% precision by the end of LHC Run 3. [83, 84]. In Fig. 10, these projections are shown assuming $\mathcal{B}(K^+ \rightarrow \pi^+ S) \sim 2 \times 10^{-12}$. The SHiP experiment can reconstruct final states with two charged tracks. We also present the projected sensitivity of SHiP for a scalar decaying into two charged particles [85, 86], as reanalyzed by Winkler [75].

B. Direct detections

In this model, direct detection can impose a more stringent limit on the mixing angle α than beam-dump experiments. When dark matter interacts with a target composed of a specific atomic nucleus through the exchange of particles like Higgs-like particles, S and h , it interacts with the

nucleus in a spin-independent t -channel. The main constraint of such experiments is determined by the scattering cross-section of dark matter and nucleons, $\chi_{\mp}N \rightarrow \chi_{\mp}N$,

$$\sigma_{\text{SI}}^N = \left(\frac{m_{\mp}m_N}{m_{\mp} + m_N} \right)^2 \frac{m_N^2 f_N^2 f^2 \sin^2 2\alpha}{16\pi v_H^2} \left(\frac{1}{m_S^2} - \frac{1}{m_h^2} \right)^2 \quad (85)$$

$$\simeq \frac{m_N^4 f_N^2 f^2 \sin^2 2\alpha}{16\pi v_H^2 m_S^4}, \quad \text{if } m_{\mp} \gg m_N, \quad (86)$$

where m_N is the mass of the nucleon, $f_N \simeq 0.3$ is related to the nucleon matrix element [88] in the isospin limit, and we have used the fact that $m_S \ll m_h$. This formula indicates that when the dark matter mass is much larger than the nucleon mass, the scattering cross section no longer depends on the dark matter mass. Moreover, with a fixed upper limit on the cross section, a smaller m_S results in a lower upper limit for α .

Figure 10 displays upper bounds on α as a function of m_S , based on PandaX-4T data [89]. Since later discussions suggest that small-scale structures typically favor $m_- \gtrsim 10$ GeV (see Figs. 11 and 12), a reference value of $m_- = 10$ GeV is used, with 100 GeV for comparison to illustrate the relationship between the results and m_- . Note that when $m_- \geq 100$ GeV, the result is almost independent of m_- . The figure also shows that PandaX-4T sets a more stringent limit on α than colliders or fixed-target experiments. For instance, at $m_S = 50$ MeV, we find $\alpha < 10^{-7}$. Future LZ experiments could increase the sensitivity of α measurement by up to a factor of 5 compared to Panda. Future LZ experiments [90], as shown by the green dashed line in Fig. 10, could potentially increase the sensitivity of α measurement by a factor of five compared to Panda.

X. SELF-SCATTERINGS OF DARK MATTER AND THE SMALL-SCALE STRUCTURE PROBLEMS

Self-interacting dark matter was introduced partly due to its strong potential to explain observations of small-scale structures that conflict with collisionless cold dark matter predictions. It provides alternative solutions to various existing small-scale problems [25, 26, 91].

Dark matter self-interactions can reduce the core density distribution, potentially helping to solve various cosmological problems. Lowering the central density of the Milky Way subhalo addresses the "too big to fail" problem. Moreover, the relatively flat dark matter density at the centers of low-mass galaxies explains the rotation curves, resolving the core-cusp issue. This idea also applies to Milky Way-sized halos, where a diminished sub-halo mass function accounts for the fewer satellite galaxies observed than predicted by the collisionless cold dark matter model, thereby clarifying the missing satellites problem. On the other hand, due to dark matter self-interactions,

galaxies with the same maximum circular velocity can exhibit significant variations in their central densities. These differences depend on when the halos formed, leading to apparent diversity in the internal rotation curves of similar galaxies [25, 27].

In this model, DM particles mainly interact through the exchange of a scalar particle, S . As they become nonrelativistic, these scattering processes can be described by the Yukawa potential (see Eq. (71)),

$$V(r) = -\frac{\alpha_f}{r} e^{-m_S r}, \quad (87)$$

where $\alpha_f = f^2/(4\pi)$ with the coupling constant f shown in Fig. 2, which can generate the correct DM relic density. The $\chi_--\chi_+$ scattering amplitude can be expressed as a sum over partial waves,

$$f(\theta) = \sum_{\ell=0}^{\infty} f_{\ell}(\theta) \equiv \frac{1}{m_- v} \sum_{\ell=0}^{\infty} e^{i\delta_{\ell}} P_{\ell}(\cos \theta) \sin \delta_{\ell}, \quad (88)$$

where θ represents the scattering angle in the center-of-mass frame. The resulting differential cross section is given by

$$\left(\frac{d\sigma}{d\Omega}\right)_{-+} = |f_{\ell}(\theta)|^2. \quad (89)$$

When two identical, unpolarized particles interact, such as the $\chi_--\chi_-$ and $\chi_+-\chi_+$ pairs, the result includes a spin-singlet state with a symmetric spatial wave function and a spin-triplet state with an antisymmetric spatial wave function. Considering that the spin-singlet state has a statistical weight of 1/4 and the spin-triplet state has a weight of 3/4, and that $f_{\ell}(\pi - \theta) = (-1)^{\ell} f_{\ell}(\theta)$, the differential cross section for scattering of the $\chi_--\chi_-$ pair is

$$\left(\frac{d\sigma}{d\Omega}\right)_{--} = \frac{1}{2} \left(\left| \sum_{\text{even}} f_{\ell}(\theta) \right|^2 + 3 \left| \sum_{\text{odd}} f_{\ell}(\theta) \right|^2 \right), \quad (90)$$

while for the $\chi_+-\chi_+$ pair, it is

$$\left(\frac{d\sigma}{d\Omega}\right)_{++} \simeq \left(\frac{d\sigma}{d\Omega}\right)_{--}, \quad \text{for } \delta m \ll m_-, \quad (91)$$

including a factor of 1/2 to prevent double-counting of identical initial states.

Our focus is on astronomical phenomena arising from dark matter self-scattering. These phenomena involve DM particles interacting with the DM background, causing them to lose momentum in the forward direction or energy perpendicular to their trajectory. The former is associated with the transfer cross-section σ_T , and the latter with the viscosity cross-section σ_V . In this paper, we

analyze related issues using the transfer cross-section. When χ_- is scattered by χ_+ , the transfer cross-section is

$$\sigma_{\text{T}}^{-+} = 2\pi \int_{-1}^1 \left(\frac{d\sigma}{d\Omega} \right)_{-+} (1 - \cos\theta) d\cos\theta. \quad (92)$$

Conversely, when χ_+ is scattered by χ_- , the result is $\sigma_{\text{T}}^{+-} = \sigma_{\text{T}}^{-+}$. These scatterings involve two distinguishable particles. However, for scattering between indistinguishable particles, such as $\chi_- \text{-} \chi_-$ and $\chi_+ \text{-} \chi_+$, because the differential cross section remains unchanged under $\theta \leftrightarrow \pi - \theta$, the definition of the transfer cross section that describes the momentum reduction rate along the direction of motion due to scattering should be modified accordingly [92, 93], with

$$\sigma_{\text{T}}^{++} = \sigma_{\text{T}}^{--} = 4\pi \int_0^1 \left(\frac{d\sigma}{d\Omega} \right)_{--} (1 - \cos\theta) d\cos\theta. \quad (93)$$

Moreover, for a dark matter system involving both χ_+ and χ_- , the average transfer cross section is

$$\begin{aligned} \sigma_{\text{T}} &= (1-r)^2 \sigma_{\text{T}}^{--} + r^2 \sigma_{\text{T}}^{++} + r(1-r) \sigma_{\text{T}}^{-+} + r(1-r) \sigma_{\text{T}}^{+-} \\ &\simeq (1-2r+2r^2) \sigma_{\text{T}}^{--} + 2r(1-r) \sigma_{\text{T}}^{-+} \quad \text{for } \delta m \ll m_-, \end{aligned} \quad (94)$$

where r is the number fraction of χ_+ in all dark matter, as defined in Eq. (61). The average transfer cross-section is proportional to the product of the number density fractions of the two scattering particles. Moreover, the effect of identical particles in the initial state has been incorporated into the cross section, as described by Eq. (90). This definition of the average transfer cross-section, as shown in Eq. (94), agrees with Refs. [30, 94, 95] in extreme cases, such as $r = 0$ or 0.5 .

Our method for calculating phase shifts closely follows Ref. [96]. To examine the impact of each dark matter component's proportion on the self-scattering cross section, we mainly focus on $r = 0$ and 0.5 , which correspond to χ_+ decaying nearly completely or having a lifetime much longer than the age of the Universe. Additionally, we analyze m_S values of 15, 30, and 60 MeV. These choices are based on the fact that the allowed mass range with $m_{Z'} < m_S/2$ in this model can satisfy current $(g-2)_\mu$ constraints, and smaller m_S values better match experimental data (see Figs. 11 and 12).

In the left panels of Figs. 11 and 12, we select some relative velocities relevant to various small-scale structures as references. We plot the relationship between σ_{T}/m_- and m_- at these specific velocities. The results show that, in the resonance region of dark matter mass, the relative change of σ_{T}/m_- as v varies will differ considerably from other regions.

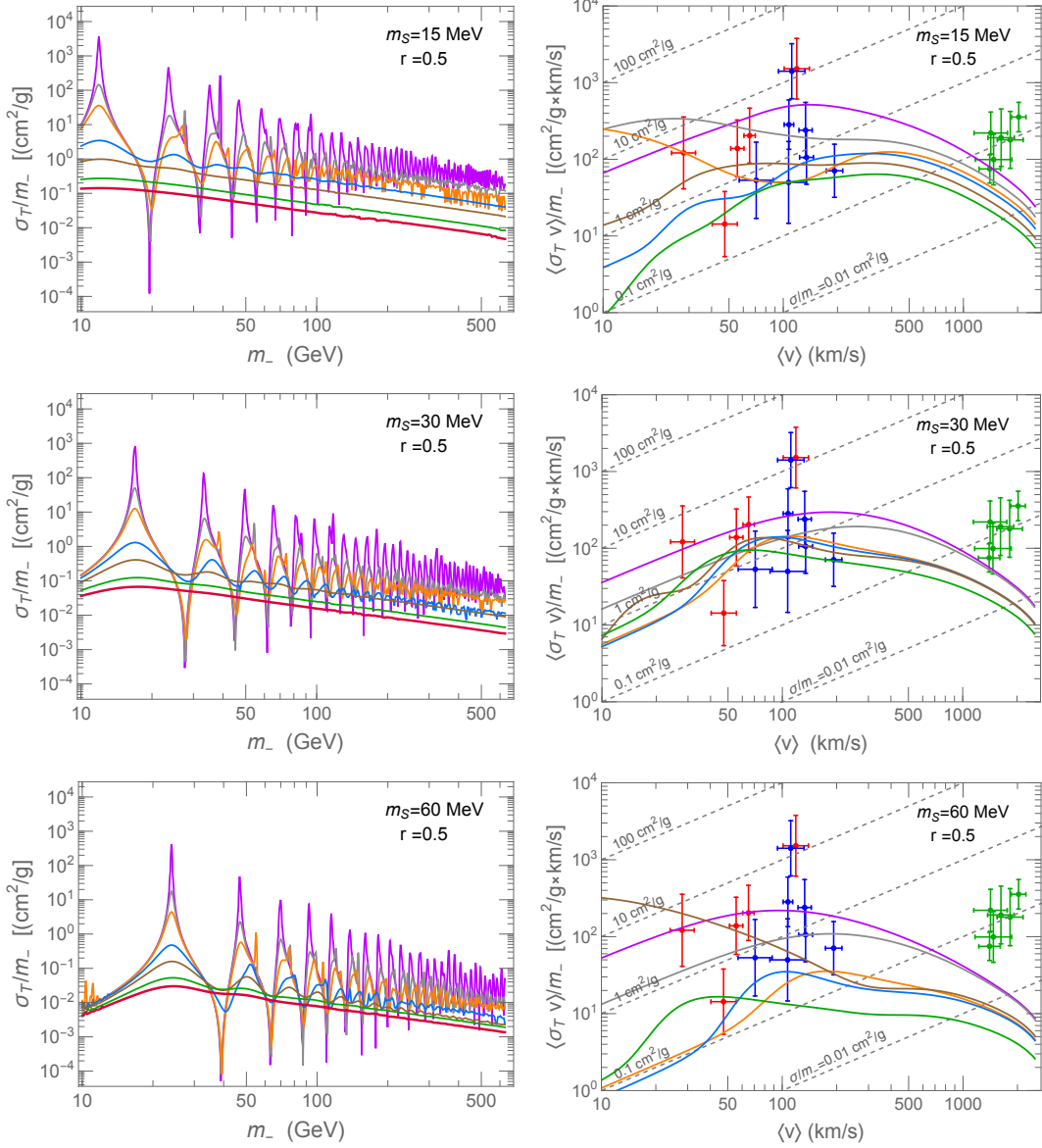


FIG. 11. Left: Self-interaction cross sections per unit DM mass vs. m_- for $m_S = 15, 30, 60$ MeV. The curves, from top to bottom at the peak with the smallest m_- , represent velocities of 10 (purple), 50 (gray), 100 (orange), 300 (blue), 500 (brown), 800 (green), and 1000 (red) km/s. Right: Velocity-weighted self-interaction cross sections per unit DM mass vs. average relative velocity $\langle v \rangle$ for $m_S = 15, 30, 60$ MeV. In the top-right panel at $\langle v \rangle = 500$ km/s, the curves from top to bottom in purple, gray, orange, blue, brown, and green represent $m_- = 26, 36, 46, 54, 74.5,$ and 101 GeV, respectively. In the middle-right panel at $\langle v \rangle = 200$ km/s, they show $m_- = 19, 20, 38.5, 38.7, 38.95,$ and 54 GeV. In the bottom-right panel at $\langle v \rangle = 300$ km/s, they correspond to $m_- = 25, 26, 54, 55, 47,$ and 98.5 GeV. Data points from Ref. [27] include dwarfs (red), LSBs (blue), and clusters (green). $r = 0.5$ is used as the current fraction of χ_+ .

Therefore, we further select specific DM mass values that better represent or align with ex-

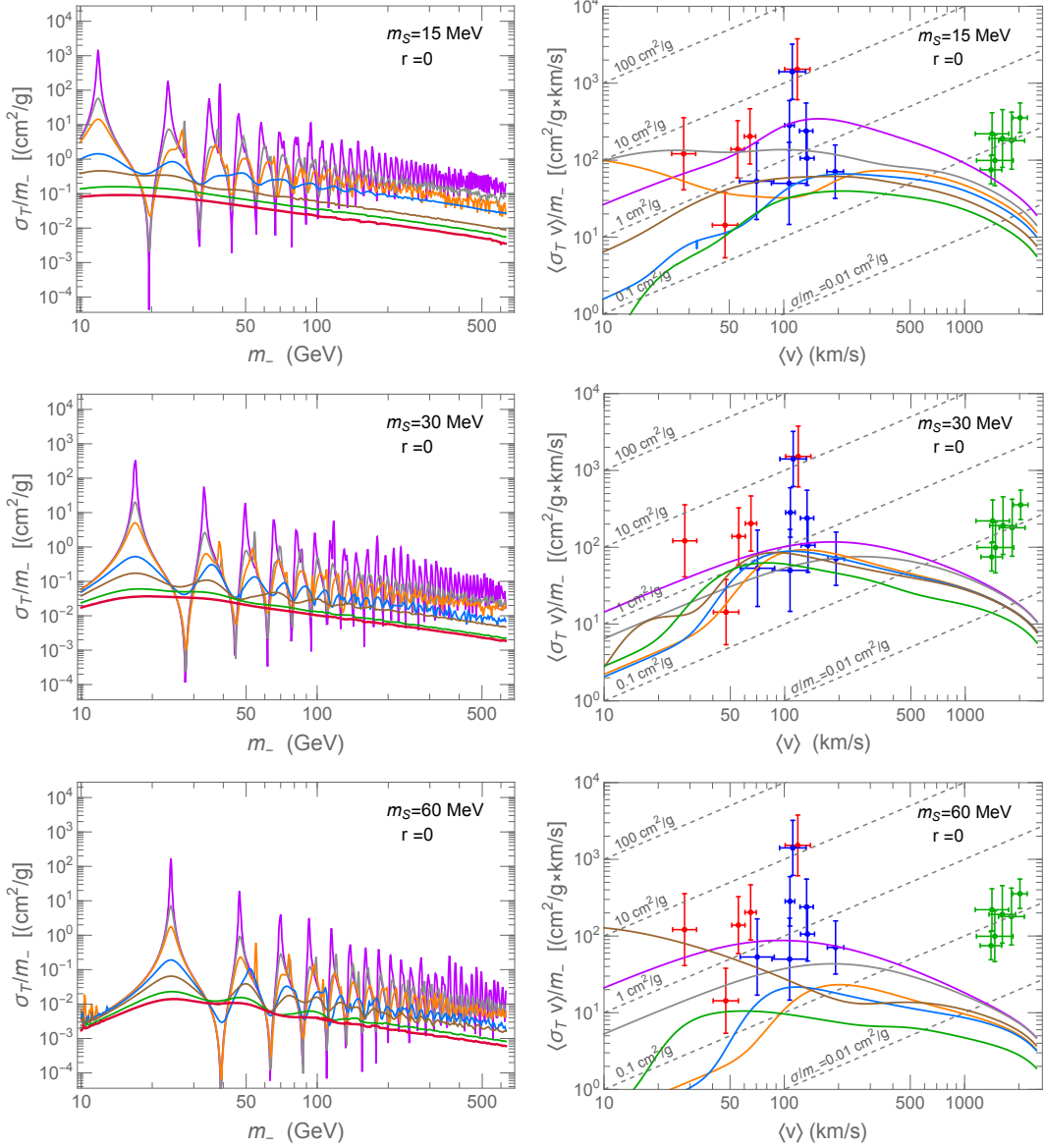


FIG. 12. Same as Fig. 11 but for $r = 0$.

perimental results for presentation. The results are illustrated in the right panels of Figs. 11 and 12. The density of the galaxy halo (ρ) is related to its age (t_{age}) and the velocity-weighted self-interaction cross section ($\langle \sigma_T v \rangle$). According to Ref. [27], within the characteristic radius of the halo, the condition $\langle \sigma_T v \rangle \rho / m_{\text{DM}} \cdot t_{\text{age}} \geq 1$ holds, indicating that on average, each dark matter particle has been scattered at least once since formation, where the transfer cross-section is used to account for forward momentum loss. Since the characteristic velocities of DM vary across galactic systems, the DM self-interaction cross-section may also depend on velocity.

We assume dark matter follows a Boltzmann-Maxwell distribution and calculate the statistical

average of the velocity-weighted cross section ($\langle\sigma_{\text{T}}v\rangle$). Figs. 11 and 12 illustrate that $\langle\sigma_{\text{T}}v\rangle/m_-$ depends significantly on the average collision velocity $\langle v\rangle$. The average velocity can be derived from the Boltzmann-Maxwell distribution given by Eq. (64), and it is related to the most probable velocity as $\langle v\rangle = 2\sqrt{2/\pi}v_0$.

The figure also displays the data analysis of clusters and galaxies from Ref. [27], including dwarf galaxies (red), low-surface-brightness galaxies (LSBs) (blue), and galaxy clusters (green). In Ref. [27], the authors used the semi-analytic Jeans method to infer from stellar dynamics that dark matter self-interactions are related to the density near the core, from galaxy to cluster systems. Since our results show that self-interactions within clusters are generally weaker than those in dwarf galaxies and LSBs, our findings provide a consistent solution to the core-cusp problem. Our self-interacting DM model can accommodate the diversity of DM halos. The cross section is typically around $\sigma_{\text{SI}}/m_X \sim (1 - 10) \text{ cm}^2/g$ at the scale of dwarf stars and LSBs, while at the scale of galaxy clusters, its value is generally smaller, approximately $\sigma_{\text{SI}}/m_X \sim (0.01 - 0.1) \text{ cm}^2/g$; these are consistent with astronomical estimates [25–27, 97–102]. The above trend will become more noticeable when the much smaller m_S is used or when the proportion of χ_+ particles is higher.

XI. DISCUSSIONS

Below, we examine some experiments or observations that may further explore and clarify this model.

$\mu N \rightarrow \mu N Z'$

This model suggests that Z' bosons could be generated via the bremsstrahlung process $\mu N \rightarrow \mu N Z'$ when a high-energy muon beam strikes with a target. Once NA64 μ employs a 160 GeV muon beam on a fixed target and produces 10^{11} MOTs (muons on target), its 90% CL upper limit for $g_{\mu\tau}$ could be reduced to below 3×10^{-4} for $m_{Z'} = 1 - 300 \text{ MeV}$ [103]. This projected sensitivity is capable of exploring the 2σ parameter space of $(g - 2)_\mu$ as predicted by the $L_\mu - L_\tau$ model. Additionally, Fermilab's M³ (Muon Missing Momentum) experiment aims to investigate the same parameter space of the $L_\mu - L_\tau$ model, as outlined in its Phase 1 projection [104].

Spin-dependent iDM direct detection

The direct detection of inelastic DM discussed here mainly involves the coupling constant g_χ , the kinetic-energy-mixing constant ϵ_A , and the inelastic DM mass splitting δm . To estimate the collision reaction between dark matter and target nuclei in direct detection experiments, we evaluate it using the inelastic scattering cross section of dark matter and nucleons. The Lagrangian for this

reaction, shown in Eq. (24), is

$$\mathcal{L} \supset -g_\chi J_D^\mu Z'_\mu + \epsilon_A e J_\gamma^\mu Z'_\mu - \epsilon_Z \frac{m_{Z'}^2}{m_Z^2 - m_{Z'}^2} g_Z J_Z^\mu Z'_\mu. \quad (95)$$

Since $m_{Z'}$ is much smaller than m_Z , we will omit the third term. The current J_γ^μ is further reformulated from the quark level to the nucleon level [105], given by

$$\epsilon_A e J_\gamma^\mu \rightarrow \epsilon_A e \bar{p} \gamma_\mu p, \quad (96)$$

indicating that Z' will only couple to protons and not neutrons. Z' mediates spin-dependent inelastic scattering between Majorana dark matter and protons. This process can be categorized into two types: the first, $\chi_+ p \rightarrow \chi_- p$, involves an excited dark matter particle colliding with a target and scattering down to the ground state (exothermic inelastic scattering [106, 107]). The second, $\chi_- p \rightarrow \chi_+ p$, occurs when ground-state dark matter, possessing sufficient kinetic energy, reaches the excited state through inelastic collisions with the target (endothermic inelastic scattering [107]). The expression for $\chi_\pm p \rightarrow \chi_\mp p$ is given by

$$\sigma_{\chi_\pm p}^{\text{SD}} \simeq g_\chi^2 \epsilon_A^2 e^2 \left(v^2 \frac{(3m_{Z'}^2 \mp 40\delta m m_p) m_p^2}{2\pi m_{Z'}^6} \pm \frac{3\delta m m_p}{\pi m_{Z'}^4} \right) \quad (97)$$

where v is the velocity of the incident dark matter, and its minimum must satisfy the following condition to occur

$$v_{\min} = \sqrt{\frac{1}{2m_p E_R} \left(\frac{m_p E_R}{\mu_{\chi p}} \mp \delta m \right)}, \quad (98)$$

with E_R as the recoil energy of the target and $\mu_{\chi p}$ as the reduced mass of the two colliding particles⁴.

Eq. (97) indicates that the scattering cross section is very small, consistent with it approaching zero as $\delta m \rightarrow 0$ and $v \rightarrow 0$. Because the model assumes $g_\chi < g_{\mu\tau}$ (see Fig. 3), the cross section is probably even smaller. Furthermore, ϵ_A may contain residual ϵ_0^A from higher energy scales (defined in Eq. (18)), so ϵ_A can only be related to $g_{\mu\tau}$ if ϵ_0^A vanishes. This means that even if the experiment measures ϵ_A , it cannot directly determine $g_{\mu\tau}$. Note that the constraints on $g_{\mu\tau}$ discussed earlier, based on data from CCFR and white dwarfs, are only valid if ϵ_0^A equals zero.

iDM capture in neutron stars

Neutron stars often contain significant amounts of muons, with the number ratio of muons to neutrons typically ranging from 1% to 10% [109–111]. The rate at which a neutron star captures

⁴ In experimental studies of dark matter interactions, it is necessary to account for the entire nucleus, replacing the proton mass with the mass of the target nucleus. Furthermore, the form factor of the atomic nucleus [105, 108] must be incorporated into the calculation of the scattering rate, which depends on momentum transfer. Nevertheless, these estimates still provide valuable insights.

dark matter depends on the differential cross section of inelastic dark matter scattering with the muon. This scattering mechanism is similar to the inelastic, spin-dependent scattering of Majorana dark matter with target nuclei discussed earlier. In this scenario, the inelastic scattering process, $\chi_{\pm} \mu \rightarrow \chi_{\mp} \mu$, is mediated via t -channel Z' exchange. When dark matter scatters inelastically with muons in a neutron star, the dark matter particles will be captured by the neutron star once their velocity falls below the escape velocity, v_{esc} , similar to the mechanisms of capture by the Sun or Earth [112–115]. For a dark matter particle initially traveling with velocity v outside the gravitational potential of the neutron star, its differential scattering cross section in the non-relativistic limit, after falling into the star and colliding with a muon, can be written as

$$\begin{aligned} & \frac{d\sigma}{dE_R}(\chi_{\mp} \mu \rightarrow \chi_{\pm} \mu) \\ & \simeq \frac{g_{\chi}^2 g_{\mu\tau}^2}{4\pi w^2} \frac{m_{\mu}}{(2E_R m_{\mu} + m_{Z'}^2)^2} \left[\frac{E_R}{m_{\mu}} \left(1 - 2 \frac{m_{\mu}}{m_{-}} - \frac{m_{\mu}^2}{m_{-}^2} \right) + 2 \frac{\delta m}{m_{\mu}} \left(1 + \frac{m_{\mu}}{m_{-}} \right) + 2w^2 \right], \end{aligned} \quad (99)$$

in the muon rest frame, where E_R is the recoil energy of the muon, $w = \sqrt{v^2 + v_{\text{esc}}^2}$, and the minimum velocity required for the process to occur must satisfy

$$v_{\text{min}}^2 = w_{\text{min}}^2 - v_{\text{esc}}^2 = \left(\sqrt{\frac{1}{2m_{\mu}E_R}} \left(\frac{m_{\mu}E_R}{\mu_{\chi\mu}} \mp \delta m \right) \right)^2 - v_{\text{esc}}^2, \quad (100)$$

with $\mu_{\chi\mu}$ the reduced mass of the two incident particles, χ_{-} (or χ_{+}) and μ .

Ref. [116] discusses how neutron stars capture Dirac dark matter and considers possible detection strategies. Here, we analyze the capture of Majorana DM by a neutron star through inelastic scattering with muons. When comparing our Eq. (99) with the findings in Ref. [116], it becomes clear that the differential cross section here is significantly smaller, affected by factors such as E_R/m_{μ} , $\delta m/m_{\mu}$, and w^2 . As a result, the prospects of detecting dark matter with compact stars like neutron stars using this model remain quite limited.

Inelastic upscattering across different galaxy systems

In a galaxy or cluster system, when dynamic equilibrium is reached through virialization, the temperature near its center may exceed the dark matter's mass-splitting (δm). According to Ref. [14], because the DM temperature near the Milky Way's center is relatively high, χ_{-} can decrease and be upscattered into the χ_{+} state. Assuming an initially small χ_{+} density, then after some time, the number density of χ_{+} is denoted by

$$n_{\chi_{+}} \simeq n_{\chi_{-}} \min(n_{\chi_{-}} \langle \sigma v \rangle_{\chi_{-}\chi_{-} \rightarrow \chi_{+}\chi_{+}} t_{\text{mw}}, e^{-\delta m/T_{\text{mw}}}) \quad (101)$$

where t_{mw} represents the age of the Milky Way and T_{mw} indicates the temperature near its center, which varies with distance from it. Once the upward-scattering process equilibrates χ_+ , the relation

$$n_{\chi_-} \langle \sigma v \rangle_{\chi_+ \chi_+ \rightarrow \chi_- \chi_-} t \sim e^{\delta m / T_{\text{mw}}}, \text{ with } t \leq t_{\text{mw}}, \quad (102)$$

holds, where we have used the detailed equilibrium condition. Since the initial dark matter state can exchange very light scalars (S) during annihilation, it is expected that the annihilation cross section will include a Sommerfeld correction, which could be significant (as shown in Fig. 8). Therefore, more χ_+ are expected near the galaxy or cluster center. This possibility allows for indirect detection of processes like $\chi_+ \chi_- \rightarrow \mu^+ \mu^-, \tau^+ \tau^-$. We will explore this further in a separate paper.

XII. SUMMARY

We have constructed the inelastic Majorana dark matter model extended by a $U(1)_{L_\mu - L_\tau}$ gauge symmetry added to the Standard Model. Following spontaneous symmetry breaking, two nearly degenerate Majorana dark matter particles are formed. The $U(1)_{L_\mu - L_\tau}$ gauge boson, Z' , gains mass through symmetry breaking and can interact with muons, tauons, and their neutrinos. This interaction explains the observed deviation in the muon anomalous magnetic moment $(g-2)_\mu$, which exceeds the standard model prediction by more than 4.2σ . Furthermore, the model's parameters are still consistent with experimental and astronomical data.

This Z' gauge boson can interact with particles in the dark sector. Due to spontaneous symmetry breaking, the dark sector fermions split into two separate Majorana fermion states, χ_\pm , with masses ranging from about 10 GeV to hundreds of GeV. However, the two states differ slightly in mass due to a tiny Dirac mass term. Scalar particles that spontaneously break symmetry in the dark sector have masses around the MeV scale and are crucial for the evolution, relic abundance, and self-interaction of dark matter. Some features of this model are described below.

- Assuming Z' can couple with muons and thus explain the $(g-2)_\mu$, we analyze the constraints from various related experiments on the $g_{\mu\tau}$ and $m_{Z'}$ parameter space (Sec. IV). Since Z' can mix with photon and Z at the one-loop level, this enables WD cooling and Borexino to impose additional restrictions on $g_{\mu\tau}$ and $m_{Z'}$. However, the mixing of Z' with photons or Z' with Z may involve kinetic energy mixing effects originating from higher energy scales (Sec. II C). Consequently, the reliability of WD cooling and Borexino constraints in the $m_{Z'} \lesssim 10\text{MeV}$ region (Fig. 1) could also be affected by this factor. In addition, Z' bosons can be generated via the Bremsstrahlung reaction $\mu N \rightarrow \mu N Z'$ by colliding a high-energy

muon beam with a target. This method will be used in experiments like NA64 μ and M³ to thoroughly investigate the 2σ allowed parameter space of the $L_\mu - L_\tau$ model interpretation related to $(g - 2)_\mu$ (see Sec. XI).

- During thermal evolution, S and Z' remain in thermal equilibrium with ν_μ and ν_τ through reactions like $S \leftrightarrow Z'Z'$ and $Z' \leftrightarrow \nu_\mu\bar{\nu}_\mu, \nu_\tau\bar{\nu}_\tau$. Because Z' can mix with photons at the one-loop level, the decay $Z' \rightarrow e^+e^-$ also helps maintain thermal balance among SM particles. About one second after the Big Bang, when the weak interaction rate fell below the expansion rate of the Universe, the interactions among these groups— (γ, e^\pm) , (ν_e) , and (ν_μ, ν_τ) — mainly resulted from $Z' \rightarrow e^+e^-$, leading to entropy transfer among them (Sec. VI). This affects the current N_{eff} observations (Fig. 5) and helps lessen the Hubble tension (Fig. 1).
- In this model, the main process for DM evolution during freeze-out is the annihilation $\chi_\mp\chi_\mp \rightarrow SS$. A strong coupling constant between DM and S is crucial, as it ensures the correct DM relic abundance (Sec. V) and promotes significant DM self-interactions. These self-interactions can help address small-scale structure issues in the Universe (Sec. X); therefore, we require that m_S exceeds roughly $2m_{Z'}$ (on the tens of MeV scale), and the DM mass m_\mp ranges from 10 GeV to several hundred GeV (Figs. 11 and 12). The coupling constant between χ_\mp and Z' must be much smaller than $g_{\mu\tau}$ to prevent reactions like $\chi_-\chi_+ \rightarrow Z'S$ and $\chi_\mp\chi_\mp \rightarrow Z'Z'$ from becoming dominant during the evolution.
- The remaining amount of excited Majorana DM, χ_+ , is related to its lifetime (Sec. VII). The lifetime depends on the DM mass splitting δm , $m_{Z'}$, and the coupling constants g_χ and $g_{\mu\tau}$, but not on m_- . When $g_\chi/g_{\mu\tau}$ is set to $1/20$, and for $m_{Z'}$ less than 100 MeV (a feasible range for $(g - 2)_\mu$ measurements), a mass splitting of 100–1000 eV in dark matter can make the excited state, χ_+ , contribute as much as 20% to the total dark matter (Fig. 6). Furthermore, inelastic upscattering increases the χ_+ number density (Sec. XI) because of the high dark matter temperature at galaxy centers. The dense dark matter environment in these regions makes them suitable for detecting signals from the annihilation of $\chi_+\chi_-$ into $\mu^+\mu^-$ or $\tau^+\tau^-$ by analyzing photon spectra. In Sec. XI, we also discuss how to measure dark matter through direct-detection experiments or inelastic scattering in neutron stars. However, the inelastic scattering cross section for these methods is too small, making it ineffective for detecting this model.
- This model shows that the key process determining the relic abundance after dark matter

evolution is the annihilation of $\chi_{\mp}\chi_{\mp} \rightarrow SS$. Although this annihilation cross-section is p -wave suppressed at this stage, the two dark matter particles still exchange very light S particles before annihilation, which enhances the cross-section through the Sommerfeld factor (Sec. VIII B). The main final products of this annihilation are neutrinos. We also compare these theoretical predictions with the current upper limits from SK experiments (Fig. 9).

- In this model, the S scalar mainly interacts with Z' to achieve thermal equilibrium with the SM bath. However, S particles can also directly couple to SM particles via the slight mixing angle α , arising from mixing with SM Higgs particles. We explore various experimental constraints on the size of this mixing angle (Sec. IX). Among these, the direct detection experiment PandaX-4T imposes the tightest upper limit on α (Fig. 10).
- In the dark matter mass range of 10 to hundreds of GeV, and with the S scalar particle mass in the range of tens of MeV, the velocity-weighted cross section $\langle\sigma_T v\rangle/m_-$ shows a strong dependence on the average collision velocity $\langle v\rangle$ (Figs. 11 and 12). Our results can provide a consistent solution to the core-cusp problem. This self-interacting Majorana DM model explains the diversity of DM halos. At the scale of dwarfs and low surface brightness galaxies, the value is usually σ_{SI}/m_- around $(1 - 10) \text{ cm}^2/g$, while at the scale of galaxy clusters, it is generally smaller, roughly $\sigma_{SI}/m_- \sim 0.01 - 0.1 \text{ cm}^2/g$ (Sec. X).

Acknowledgments. This work was partly supported by the National Center for Theoretical Sciences and the National Science and Technology Council of Taiwan under grant number NSTC 113-2112-M-033-005.

Appendix A: The derivation of the inelastic Majorana eigenstates after SSB

After SSB, the mass term of the dark fermions is given by

$$\mathcal{L}_m = \mathcal{L}_m^D + \mathcal{L}_m^M, \quad (\text{A1})$$

where the Dirac mass part is

$$\begin{aligned} -\mathcal{L}_m^D &= \frac{m_D}{2}(\bar{\chi}\chi + \bar{\chi}^c\chi^c) \\ &= \frac{m_D}{2}(\bar{\chi}_R\chi_L + \bar{\chi}_{R\chi L} + \bar{\chi}_R^c\chi_L^c + \bar{\chi}_{R\chi L}^c), \end{aligned} \quad (\text{A2})$$

and the Majorana mass part with $fv_S \equiv m_M$ is

$$\begin{aligned} -\mathcal{L}_m^M &= \frac{m_M}{2} (\bar{\chi}^c \chi + \bar{\chi} \chi^c) = \frac{m_M}{2} (\bar{\chi}_R^c \chi_L + \bar{\chi}_L \chi_R^c) + \frac{m_M}{2} (\bar{\chi}_L^c \chi_R + \bar{\chi}_R \chi_L^c) \\ &= \frac{m_M}{2} (\bar{\chi}_L + \bar{\chi}_R^c) (\chi_L + \chi_R^c) + \frac{m_M}{2} (\bar{\chi}_R + \bar{\chi}_L^c) (\chi_R + \chi_L^c). \end{aligned} \quad (\text{A3})$$

Without m_D , the dark fermion can be represented as two degenerate, independent Majorana states, $\chi_1 = \chi_L + \chi_R^c$ and $\chi_2 = \chi_R + \chi_L^c$; note that an arbitrary angle can rotate the two states to have a new pair if m_D vanishes. Using χ_1 and χ_2 to form the state column $\bar{\mathbf{X}}$, we can write down the masses in the 4×4 matrix form and then recast the mass Lagrangian as⁵

$$-\mathcal{L}_m = \underbrace{\begin{pmatrix} \bar{\chi}_L & \bar{\chi}_R^c & \bar{\chi}_L^c & \bar{\chi}_R \end{pmatrix}}_{\bar{\mathbf{X}}} \begin{pmatrix} 0 & 1 & 0 & 0 \\ 1 & 0 & 0 & 0 \\ 0 & 0 & 0 & 1 \\ 0 & 0 & 1 & 0 \end{pmatrix} \underbrace{\begin{pmatrix} m_M & 0 & m_D & 0 \\ 0 & m_M & 0 & m_D \\ m_D & 0 & m_M & 0 \\ 0 & m_D & 0 & m_M \end{pmatrix}}_{\mathbf{M}} \underbrace{\begin{pmatrix} \chi_L \\ \chi_R^c \\ \chi_L^c \\ \chi_R \end{pmatrix}}_{\mathbf{X}}. \quad (\text{A5})$$

We diagonalize the mass matrix \mathbf{M} by a unitary transformation, $\mathbf{U}_D \mathbf{M} \mathbf{U}_D^\dagger = \mathbf{D}$, where $\mathbf{D} = \text{diag}(m_M - m_D, m_M - m_D, m_M + m_D, m_M + m_D)$. The physical eigenstates can be read from

$$\mathbf{X}_D = \mathbf{U}_D \mathbf{X} = \frac{1}{\sqrt{2}} \begin{pmatrix} 0 & -1 & 0 & 1 \\ -1 & 0 & 1 & 0 \\ 0 & 1 & 0 & 1 \\ 1 & 0 & 1 & 0 \end{pmatrix} \begin{pmatrix} \chi_L \\ \chi_R^c \\ \chi_L^c \\ \chi_R \end{pmatrix} = \frac{1}{\sqrt{2}} \begin{pmatrix} \chi_R - \chi_R^c \\ -\chi_L + \chi_L^c \\ \chi_R + \chi_R^c \\ \chi_L + \chi_L^c \end{pmatrix}. \quad (\text{A6})$$

The first two elements of \mathbf{X}_D sum to χ_- , and the last two elements sum to χ_+ , given by

$$\chi_- = \frac{1}{\sqrt{2}} (-\chi_L + \chi_R - \chi_R^c + \chi_L^c) \quad \text{and} \quad \chi_+ = \frac{1}{\sqrt{2}} (\chi_L + \chi_R + \chi_R^c + \chi_L^c), \quad (\text{A7})$$

with masses $m_M - m_D$ and $m_M + m_D$, respectively.

Appendix B: Some details of obtaining mass states of kinetic-mixing gauge fields

Considering the possible kinetic mixings among the neutral gauge fields at low energy scale $\mu \lesssim m_\mu$, the neutral gauge boson sector of Lagrangian is given by

$$\begin{aligned} \mathcal{L}_{\text{gauge}} &= -\frac{1}{4} \hat{Z}_{\mu\nu} \hat{Z}^{\mu\nu} - \frac{1}{4} \hat{F}_{\mu\nu} \hat{F}^{\mu\nu} - \frac{1}{4} \hat{Z}'_{\mu\nu} \hat{Z}'^{\mu\nu} + \frac{1}{2} m_Z^2 \hat{Z}_\mu \hat{Z}^\mu + \frac{1}{2} m_{Z'}^2 \hat{Z}'_\mu \hat{Z}'^\mu \\ &\quad - \frac{1}{2} \epsilon_A \hat{Z}'_{\mu\nu} \hat{F}^{\mu\nu} - \frac{1}{2} \epsilon_Z \hat{Z}'_{\mu\nu} \hat{Z}^{\mu\nu}, \end{aligned} \quad (\text{B1})$$

⁵ Alternatively, we can write the mass Lagrangian as a 2×2 matrix,

$$-\mathcal{L}_m = \begin{pmatrix} \bar{\chi}_R^c & \bar{\chi}_R \end{pmatrix} \begin{pmatrix} m_M & m_D \\ m_D & m_M \end{pmatrix} \begin{pmatrix} \chi_L \\ \chi_L^c \end{pmatrix} + \text{h.c.}, \quad (\text{A4})$$

to find the Majorana mass eigenstates.

where an additional “*hat*” is added to gauge fields to denote that they are not the mass eigenstates. To eliminate the mixing term, we need to transform the present gauge fields into their physical states by the following procedure. We first diagonalize the kinetic term of the neutral gauge Lagrangian in terms of the canonical basis $\tilde{\mathbf{V}}_\mu = (\tilde{Z}_\mu, \tilde{A}_\mu, \tilde{Z}'_{prime\mu})^T$, resulting in the kinetic mixing terms vanished under transformation $\tilde{\mathbf{V}}_\mu = \zeta \hat{\mathbf{V}}_\mu$, where $\hat{\mathbf{V}}_\mu = (\hat{Z}_\mu, \hat{A}_\mu, \hat{Z}'_\mu)^T$, and

$$\zeta = \begin{pmatrix} 1 & 0 & \epsilon_Z \\ 0 & 1 & \epsilon_A \\ 0 & 0 & 1 - \frac{\epsilon_Z^2}{2} - \frac{\epsilon_A^2}{2} \end{pmatrix} + \mathcal{O}(\epsilon_{A,Z}^3). \quad (\text{B2})$$

In terms of $\tilde{\mathbf{V}}_\mu$, the mass term in Eq. (18) can be written as $\mathcal{L}_{\text{gauge}}^{\text{mass}} = (1/2)\tilde{\mathbf{V}}_\mu^T (\zeta^{-1})^T \mathbf{M} \zeta^{-1} \tilde{\mathbf{V}}_\mu$, where $\mathbf{M} = \text{diag}(m_Z, 0, m_{Z'})$. We can then diagonalize the mass matrix to be $\xi^T ((\zeta^{-1})^T \mathbf{M} \zeta^{-1}) \xi = \mathbf{M}_{ph}$, where

$$\xi = \begin{pmatrix} 1 - \frac{\epsilon_Z^2 m_Z^4}{2(m_Z^2 - m_{Z'}^2)^2} & 0 & \frac{\epsilon_Z m_Z^2}{m_Z^2 - m_{Z'}^2} \\ 0 & 1 & 0 \\ -\frac{\epsilon_Z m_Z^2}{m_Z^2 - m_{Z'}^2} & 0 & 1 - \frac{\epsilon_Z^2 m_Z^4}{2(m_Z^2 - m_{Z'}^2)^2} \end{pmatrix} + \mathcal{O}(\epsilon_{A,Z}^3), \quad (\text{B3})$$

and diagonalized mass matrix is

$$\mathbf{M}_{ph} = \begin{pmatrix} m_Z^2 + \frac{\epsilon_Z^2 m_Z^4}{m_Z^2 - m_{Z'}^2} & 0 & 0 \\ 0 & 1 & 0 \\ 0 & 0 & m_{Z'}^2 (1 + \epsilon_A^2) - \frac{\epsilon_Z^2 m_Z^4}{m_Z^2 - m_{Z'}^2} \end{pmatrix} + \mathcal{O}(\epsilon_{A,Z}^3). \quad (\text{B4})$$

Finally, the physical fields are related the original ones via $\mathbf{V}_\mu = (Z_\mu, A_\mu, Z'_\mu)^T = \mathbf{U} \hat{\mathbf{V}}_\mu$, where the transform matrix is

$$\mathbf{U} = \xi^{-1} \zeta = \begin{pmatrix} 1 - \frac{\epsilon_Z^2 m_Z^4}{2(m_Z^2 - m_{Z'}^2)^2} & 0 & -\frac{\epsilon_Z m_{Z'}^2}{m_Z^2 - m_{Z'}^2} \\ 0 & 1 & \epsilon_A \\ \frac{\epsilon_Z m_{Z'}^2}{m_Z^2 - m_{Z'}^2} & 0 & 1 - \frac{\epsilon_A^2}{2} - \frac{\epsilon_Z^2 m_{Z'}^4}{2(m_Z^2 - m_{Z'}^2)^2} \end{pmatrix} + \mathcal{O}(\epsilon_{A,Z}^3). \quad (\text{B5})$$

Appendix C: Decay widths

$$\Gamma_{S \rightarrow Z' Z'} = \frac{(g_\chi \cos \alpha)^2}{8\pi} \frac{m_S^3}{m_{Z'}^2} \left(1 - \frac{4m_{Z'}^2}{m_S^2}\right)^{1/2} \left(1 - \frac{4m_{Z'}^2}{m_S^2} + \frac{12m_{Z'}^4}{m_S^4}\right), \quad (\text{C1})$$

$$\Gamma_{Z' \rightarrow f\bar{f}} = \begin{cases} \frac{g_{\mu\tau}^2}{12\pi} m_{Z'} \left(1 + \frac{2m_f^2}{m_{Z'}^2}\right) \left(1 - \frac{4m_f^2}{m_{Z'}^2}\right)^{1/2} \theta(m_{Z'} - 2m_f), & \text{for } f = \mu \text{ or } \tau, \\ \frac{g_{\mu\tau}^2}{24\pi} m_{Z'}, & \text{for } f = \nu_\mu \text{ or } \nu_\tau, \end{cases} \quad (\text{C2})$$

$$\Gamma_{Z' \rightarrow e^+e^-} = \frac{\alpha \epsilon_A^2 m_{Z'}}{3} \left(1 + \frac{2m_e^2}{m_{Z'}^2}\right) \left(1 - \frac{4m_e^2}{m_{Z'}^2}\right)^{1/2}, \quad (\text{C3})$$

$$\Gamma_{H \rightarrow \chi_\pm \chi_\pm} = \frac{f^2 \sin^2 \alpha}{16\pi m_H^2} (m_H^2 - 4m_\pm^2)^{3/2} \theta(m_H - 2m_\pm), \quad (\text{C4})$$

$$\Gamma_{H \rightarrow SS} = \frac{1}{128\pi m_H^2 v_S^2 v_H^2} (m_H^2 + 2m_S^2)^2 (m_H - 4m_S^2)^{1/2} (v_H \cos \alpha + v_S \sin \alpha)^2 \sin^2 2\alpha, \quad (\text{C5})$$

$$\Gamma_{H \rightarrow Z'Z'} = \frac{(g_\chi \sin \alpha)^2 m_H^3}{8\pi m_{Z'}^2} \left(1 - \frac{4m_{Z'}^2}{m_H^2}\right)^{1/2} \left(1 - \frac{4m_{Z'}^2}{m_H^2} + \frac{12m_{Z'}^4}{m_H^4}\right). \quad (\text{C6})$$

Appendix D: Cross sections relevant to the DM relic abundance

The thermally averaged annihilation cross section for the process $ij \rightarrow k\ell$ at temperature T is represented by [54]

$$\langle \sigma v \rangle_{ij \rightarrow k\ell} = \frac{g_i g_j T}{8\pi^4 n_i^{\text{eq}}(T) n_j^{\text{eq}}(T)} \int_{(m_i+m_j)^2}^{\infty} \sigma_{ij \rightarrow k\ell} p_{ij}^2 \sqrt{s} K_1 \left(\frac{\sqrt{s}}{T} \right) ds, \quad (\text{D1})$$

where K_n is the modified Bessel function of the second kind, and the Mandelstam variable s is the square of the center-of-mass energy. The momentum of particle i (or j) in the center-of-mass frame is

$$p_{ij} = \frac{[s - (m_i + m_j)^2]^{1/2} [s - (m_i - m_j)^2]^{1/2}}{2\sqrt{s}}, \quad (\text{D2})$$

and the equilibrium number density of i at temperature T is given by

$$n_i^{\text{eq}}(T) = \frac{T}{2\pi^2} g_i m_i^2 K_2 \left(\frac{m_i}{T} \right), \quad (\text{D3})$$

with g_i being its internal degrees of freedom.

Using $s = (m_i + m_j)^2 + m_i m_j v^2$, where $v = |\vec{v}_i - \vec{v}_j|$ is the relative velocity of two particles i and j , we expand $(\sigma v)_{ij \rightarrow kl}$ in power of v^2 as the form,

$$(\sigma v)_{ij \rightarrow kl} = a + bv^2 + cv^4 + \dots, \quad (\text{D4})$$

and perform calculations about its thermal average in terms of the variable v^2 . The result for $m_i \approx m_j$ is given by [56]

$$\langle \sigma v \rangle_{ij \rightarrow kl} = a + 6b \frac{T}{m_i} + (18b + 60c) \left(\frac{T}{m_i} \right)^2 + \dots. \quad (\text{D5})$$

1. $\chi_{\mp} \chi_{\mp} \rightarrow SS$

The cross sections for $\chi_{\mp} \chi_{\mp} \rightarrow SS$, which occur through the u - and t -channels mediated by χ_{\pm} and through the s -channel by the scalar S , are given by

$$\begin{aligned} \sigma_{\chi_{\mp} \chi_{\mp} \rightarrow SS} = & \frac{f^2 c_{\alpha}^2 \sqrt{s - 4m_S^2}}{32\pi s m_Z^2 \sqrt{s - 4m_{\mp}^2} (\Gamma_S^2 m_S^2 + (s - m_S^2)^2)} \\ & \times \left[- \frac{f^2 c_{\alpha}^2 m_Z^2 ((\Gamma_S^2 - 2s)m_S^2 + m_S^4 + s^2) (2m_{\mp}^2 (s - 8m_S^2) + 16m_{\mp}^4 + 3m_S^4)}{m_{\mp}^2 (s - 4m_S^2) + m_S^4} \right. \\ & + \frac{f c_{\alpha} m_Z}{\sqrt{s - 4m_{\mp}^2} \sqrt{s - 4m_S^2} (s - 2m_S^2)} \left(\log \frac{s + \sqrt{s - 4m_{\mp}^2} \sqrt{s - 4m_S^2} - 2m_S^2}{s - \sqrt{s - 4m_{\mp}^2} \sqrt{s - 4m_S^2} - 2m_S^2} \right) \\ & \times \left(f c_{\alpha} m_Z (\Gamma_S^2 m_S^2 + (s - m_S^2)^2) (s^2 - 4m_S^2 (4m_{\mp}^2 + s) + 16sm_{\mp}^2 - 32m_{\mp}^4 + 6m_S^4) \right. \\ & \left. \left. - 12g_{\chi} c_{\alpha}^3 m_{\mp} m_S^2 (s^2 - 3sm_S^2 + 2m_S^4) (s - 8m_{\mp}^2 + 2m_S^2) \right) \right. \\ & \left. - 24fg_{\chi} c_{\alpha}^4 m_{\mp} m_S^2 m_Z (s - m_S^2) + 18g_{\chi}^2 c_{\alpha}^6 m_S^4 (s - 4m_{\mp}^2) \right], \quad (\text{D6}) \end{aligned}$$

where $c_{\alpha} \equiv \cos \alpha$, and s is the Mandelstam invariant mass squared of two incident particles. Here, we have used the triple coupling to calculate the s -channel amplitude,

$$\mathcal{L} \supset \frac{1}{6} g_{SSS} SSS + \dots, \quad \text{with } g_{SSS} \simeq -\frac{6g_{\chi} c_{\alpha}^3 m_S^2}{m_{Z'}}. \quad (\text{D7})$$

Considering two annihilating particles in the non-relativistic limit, the cross section is approximated as

$$(\sigma v)_{\chi_{\mp} \chi_{\mp} \rightarrow SS} \simeq \frac{3f^4}{128\pi m_{\mp}^2} \left[v^2 - \frac{13}{14} v^4 + \mathcal{O}\left(\frac{m_S^2}{m_{\mp}^2}, v^6\right) \right]. \quad (\text{D8})$$

2. $\chi_{\mp}\chi_{\mp} \rightarrow Z' Z'$

The cross-section is given by

$$\begin{aligned}
\sigma_{\chi_{\mp}\chi_{\mp} \rightarrow Z' Z'} = & \frac{g_{\chi}^2 \sqrt{s - 4m_{Z'}^2} (s - 2(m_{\mp}^2 - m_{\pm}^2 + m_{Z'}^2))^2}{32\pi m_{Z'}^4 ((s - m_S^2)^2 + \Gamma_S^2 m_S^2) s \sqrt{s - 4m_{\mp}^2} (2(m_{\mp}^2 - m_{\pm}^2 + m_{Z'}^2) - s)^3} \\
& \times \left\{ \frac{(s - 2(m_{\mp}^2 - m_{\pm}^2 + m_{Z'}^2))}{m_{\mp}^4 - 2(m_{\pm}^2 + m_{Z'}^2)m_{\mp}^2 + sm_{\pm}^2 + (m_{\pm}^2 - m_{Z'}^2)^2} \left[g_{\chi}^2 \Gamma_S^2 m_S^2 [3m_{\mp}^8 - 12m_{\pm}^2 m_{\mp}^6 + 6m_{Z'}^2 m_{\mp}^6 \right. \right. \\
& + 28m_{\pm} m_{Z'}^2 m_{\mp}^5 + 18m_{\pm}^4 m_{\mp}^4 - 13m_{Z'}^4 m_{\mp}^4 - 6m_{\pm}^2 m_{Z'}^2 m_{\mp}^4 - 20m_{\pm} m_{Z'}^4 m_{\mp}^3 - 56m_{\pm}^3 m_{Z'}^2 m_{\mp}^3 \\
& - 12m_{\pm}^6 m_{\mp}^2 - 4m_{Z'}^6 m_{\mp}^2 + 2m_{\pm}^2 m_{Z'}^4 m_{\mp}^2 - 6m_{\pm}^4 m_{Z'}^2 m_{\mp}^2 - 8m_{\pm} m_{Z'}^6 m_{\mp} - 20m_{\pm}^3 m_{Z'}^4 m_{\mp} \\
& + 28m_{\pm}^5 m_{Z'}^2 m_{\mp} + 3m_{\pm}^8 + 8m_{Z'}^8 - 4m_{\pm}^2 m_{Z'}^6 - 13m_{\pm}^4 m_{Z'}^4 - 2s^2 m_{\pm}^2 (m_{\mp} + m_{\pm})^2 + 6m_{\pm}^6 m_{Z'}^2 \\
& - 2s((m_{\mp}^2 + 2m_{\pm} m_{\mp} - m_{\pm}^2) m_{Z'}^4 - 2(m_{\mp} + m_{\pm})^2 (m_{\mp}^2 + 3m_{\pm}^2) m_{Z'}^2 + m_{\mp} (m_{\mp} + 2m_{\pm}) (m_{\mp}^2 - m_{\pm}^2)^2) \left. \right] \\
& - g_{\chi}^2 (m_S^2 - s)^2 [-3m_{\mp}^8 + 12m_{\pm}^2 m_{\mp}^6 - 6m_{Z'}^2 m_{\mp}^6 - 28m_{\pm} m_{Z'}^2 m_{\mp}^5 - 18m_{\pm}^4 m_{\mp}^4 + 13m_{Z'}^4 m_{\mp}^4 \\
& + 6m_{\pm}^2 m_{Z'}^2 m_{\mp}^4 + 20m_{\pm} m_{Z'}^4 m_{\mp}^3 + 56m_{\pm}^3 m_{Z'}^2 m_{\mp}^3 + 12m_{\pm}^6 m_{\mp}^2 + 4m_{Z'}^6 m_{\mp}^2 - 2m_{\pm}^2 m_{Z'}^4 m_{\mp}^2 \\
& + 6m_{\pm}^4 m_{Z'}^2 m_{\mp}^2 + 8m_{\pm} m_{Z'}^6 m_{\mp} + 20m_{\pm}^3 m_{Z'}^4 m_{\mp} - 28m_{\pm}^5 m_{Z'}^2 m_{\mp} - 3m_{\pm}^8 - 8m_{Z'}^8 + 4m_{\pm}^2 m_{Z'}^6 \\
& + 13m_{\pm}^4 m_{Z'}^4 + 2s^2 m_{\pm}^2 (m_{\mp} + m_{\pm})^2 - 6m_{\pm}^6 m_{Z'}^2 + 2s((m_{\mp}^2 + 2m_{\pm} m_{\mp} - m_{\pm}^2) m_{Z'}^4 \\
& - 2(m_{\mp} + m_{\pm})^2 (m_{\mp}^2 + 3m_{\pm}^2) m_{Z'}^2 + m_{\mp} (m_{\mp} + 2m_{\pm}) (m_{\mp}^2 - m_{\pm}^2)^2) \left. \right] \\
& + 4g_{\chi} f m_{Z'} (m_S^2 - s) (- (m_{\mp} + m_{\pm}) s^2 + 2(m_{\mp} + m_{\pm}) (m_{\mp}^2 - m_{\pm} m_{\mp} + m_{Z'}^2) s \\
& + 4m_{\mp} m_{Z'}^2 (m_{\mp}^2 - m_{\pm}^2 - 2m_{Z'}^2)) (m_{\mp}^4 - 2(m_{\pm}^2 + m_{Z'}^2) m_{\mp}^2 + sm_{\pm}^2 + (m_{\pm}^2 - m_{Z'}^2)^2) \\
& + 2f^2 (4m_{\mp}^2 - s) m_{Z'}^2 (12m_{Z'}^4 - 4sm_{Z'}^2 + s^2) (m_{\mp}^4 - 2(m_{\pm}^2 + m_{Z'}^2) m_{\mp}^2 + sm_{\pm}^2 + (m_{\pm}^2 - m_{Z'}^2)^2) \left. \right] \\
& - \frac{g_{\chi}}{\sqrt{s - 4m_{\mp}^2} \sqrt{s - 4m_{Z'}^2}} \left[\log \left(\frac{2m_{\mp}^2 - 2m_{\pm}^2 + 2m_{Z'}^2 - s - \sqrt{s - 4m_{\mp}^2} \sqrt{s - 4m_{Z'}^2}}{2m_{\mp}^2 - 2m_{\pm}^2 + 2m_{Z'}^2 - s + \sqrt{s - 4m_{\mp}^2} \sqrt{s - 4m_{Z'}^2}} \right) \right. \\
& \times \left[\Gamma_S^2 g_{\chi} [16m_{Z'}^8 - 8(5m_{\mp}^2 + 2m_{\pm} m_{\mp} + m_{\pm}^2) m_{Z'}^6 - 2(m_{\mp} - m_{\pm}) (5m_{\mp}^3 - 23m_{\pm} m_{\mp}^2 \right. \\
& - 33m_{\pm}^2 m_{\mp} - 13m_{\pm}^3) m_{Z'}^4 + 4(m_{\mp}^2 - m_{\pm}^2)^2 (7m_{\mp}^2 + 14m_{\pm} m_{\mp} + 3m_{\pm}^2) m_{Z'}^2 + 6(m_{\mp}^2 - m_{\pm}^2)^4 \\
& + s^2 (4m_{Z'}^4 + 4(m_{\mp} + m_{\pm})^2 m_{Z'}^2 + (m_{\mp} - 3m_{\pm}) (m_{\mp} + m_{\pm})^3) - 4s (4m_{\mp} (m_{\mp} + 2m_{\pm}) m_{Z'}^4 \\
& + (3m_{\mp} - 5m_{\pm}) (m_{\mp} + m_{\pm})^3 m_{Z'}^2 + 2m_{\mp} (m_{\mp} - m_{\pm})^2 (m_{\mp} + m_{\pm})^3) \left. \right] m_S^2 \\
& + (m_S^2 - s) [4f m_{Z'} (2(m_{\mp}^2 - m_{\pm}^2 + m_{Z'}^2) - s) [s^2 m_{\pm} (m_{\mp} + m_{\pm})^2 \\
& + 4m_{\mp} (m_{\mp} + m_{\pm} - m_{Z'}) m_{Z'}^2 (m_{\mp} + m_{\pm} + m_{Z'}) ((m_{\mp} - m_{\pm})^2 + 2m_{Z'}^2) + 2s (2(m_{\mp} - m_{\pm}) m_{Z'}^4 \\
& - (m_{\mp} + m_{\pm}) (3m_{\mp}^2 + m_{\pm}^2) m_{Z'}^2 + m_{\mp} (m_{\mp}^2 - m_{\pm}^2)^2) + (m_S^2 - s) g_{\chi} [16m_{Z'}^8 - 8(5m_{\mp}^2 \\
& + 2m_{\pm} m_{\mp} + m_{\pm}^2) m_{Z'}^6 - 2(m_{\mp} - m_{\pm}) (5m_{\mp}^3 - 23m_{\pm} m_{\mp}^2 - 33m_{\pm}^2 m_{\mp} - 13m_{\pm}^3) m_{Z'}^4 \\
& + 4(m_{\mp}^2 - m_{\pm}^2)^2 (7m_{\mp}^2 + 14m_{\pm} m_{\mp} + 3m_{\pm}^2) m_{Z'}^2 + 6(m_{\mp}^2 - m_{\pm}^2)^4 + s^2 (4m_{Z'}^4 + 4(m_{\mp} + m_{\pm})^2 m_{Z'}^2 \\
& + (m_{\mp} - 3m_{\pm}) (m_{\mp} + m_{\pm})^3) - 4s (4m_{\mp} (m_{\mp} + 2m_{\pm}) m_{Z'}^4 + (3m_{\mp} - 5m_{\pm}) (m_{\mp} + m_{\pm})^3 m_{Z'}^2 \\
& + 2m_{\mp} (m_{\mp} - m_{\pm})^2 (m_{\mp} + m_{\pm})^3) \left. \right] \left. \right] \left. \right\}. \tag{D9}
\end{aligned}$$

For two incident particles in the non-relativistic limit, the annihilation cross section, performed

the Laurent series expansion around $m_{Z'} = 0$, is approximated as

$$\begin{aligned}
(\sigma v)_{\chi\mp\chi\mp\rightarrow Z'Z'} &\simeq \frac{g_\chi^4}{16\pi m_-^2} \left\{ 1 + \frac{1}{2} \left(\frac{fm_-}{g_\chi m_{Z'}} \right)^2 \left[1 - \frac{8}{3} \frac{g_\chi m_-}{f m_{Z'}} + \frac{8}{3} \left(\frac{g_\chi m_-}{f m_{Z'}} \right)^2 \right] v^2 \right. \\
&\quad \left. + \mathcal{O} \left(\frac{\delta m}{m_-}, \frac{m_{Z'}^2}{m_-^2}, \frac{m_S^2}{m_-^2}, v^4 \right) \right\}, \tag{D10}
\end{aligned}$$

where the contribution proportional to v^4 is negligible compared with the v^2 term. Compared with the s -wave term, the p -wave term is enhanced by a factor of $(fm_/(g_\chi m_{Z'}))^2$.

3. $\chi-\chi_+ \rightarrow \ell\bar{\ell}, \nu_\ell\bar{\nu}_\ell$

$$\begin{aligned}
\sigma_{\chi-\chi_+\rightarrow\ell\bar{\ell}} &= \frac{g_{\mu\tau}^2 g_\chi^2 \sqrt{s - (m_+ + m_-)^2} (2s + (m_+ - m_-)^2) \sqrt{s - 4m_\ell^2} (2m_\ell^2 + s)}{24\pi s^{3/2} \sqrt{s - (m_+ - m_-)^2} ((s - m_{Z'})^2 + \Gamma^2 m_{Z'}^2)}, \\
\sigma_{\chi-\chi_+\rightarrow\nu_\ell\bar{\nu}_\ell} &= \frac{g_{\mu\tau}^2 g_\chi^2 \sqrt{s - (m_+ + m_-)^2} (2s + (m_+ - m_-)^2)}{48\pi \sqrt{s - (m_+ - m_-)^2} ((s - m_{Z'})^2 + \Gamma^2 m_{Z'}^2)}, \tag{D11}
\end{aligned}$$

where $\ell = \mu$ or τ , $\Gamma_{Z'}$ is the Z' width, which in general reads $\Gamma_{Z'} = \sum_f \Gamma_{Z'\rightarrow f\bar{f}} + \Gamma_{Z'\rightarrow\chi-\chi_+} + \Gamma_{Z'\rightarrow e\bar{e}}$ with the sums over $f = \mu, \tau, \nu_\mu$ and ν_τ , given by

$$\begin{aligned}
\Gamma_{Z'} &= \frac{g_{\mu\tau}^2 m_{Z'}}{12\pi} \left[1 + \sum_{i=\mu,\tau} (1 + 2\kappa_i)(1 - 4\kappa_i)^{1/2} \theta(1 - 2\sqrt{\kappa_i}) \right] \\
&\quad + \frac{g_{\mu\tau}^2 m_{Z'}}{12\pi} [1 - (\kappa_+ + \kappa_-)^2]^{3/2} [1 - (\kappa_+ - \kappa_-)^2]^{1/2} \left[1 + \frac{(\kappa_+ - \kappa_-)^2}{2} \right] \theta(1 - \sqrt{\kappa_+} - \sqrt{\kappa_-}) \\
&\quad + \frac{e^2 \epsilon_A^2 m_{Z'}}{12\pi} \left[(1 + 2\kappa_e)(1 - 4\kappa_e)^{1/2} \theta(1 - 2\sqrt{\kappa_e}) \right], \tag{D12}
\end{aligned}$$

with $\kappa_i \equiv m_i^2/m_{Z'}^2$. In the present study, $Z' \rightarrow \chi-\chi_+$ is kinetically blocked because $m_{Z'} < m_+ + m_-$. Considering two annihilating particles in the non-relativistic limit, the cross section is given by

$$\begin{aligned}
(\sigma v)_{\chi-\chi_+\rightarrow\ell\bar{\ell}} &= \frac{g_{\mu\tau}^2 g_\chi^2}{96\pi m_-^2} v^2 \left[1 + \frac{\delta m}{m_-} + \mathcal{O} \left(\frac{\delta m^2}{m_-^2}, \frac{m_{Z'}^2}{m_-^2}, \frac{m_\ell^2}{m_-^2} \right) \right], \\
(\sigma v)_{\chi-\chi_+\rightarrow\nu_\ell\bar{\nu}_\ell} &= \frac{g_{\mu\tau}^2 g_\chi^2}{192\pi m_-^2} v^2 \left[1 + \frac{\delta m}{m_-} + \mathcal{O} \left(\frac{\delta m^2}{m_-^2}, \frac{m_{Z'}^2}{m_-^2} \right) \right], \tag{D13}
\end{aligned}$$

where $m_+ = m_- + \delta m$.

4. $\chi-\chi_+ \rightarrow Z' s$

The cross-section is given by

$$\begin{aligned}
\sigma_{\chi-\chi_+ \rightarrow Z' s} &= \frac{c_\alpha^2 f^2 g_\chi^2 \sqrt{s - (m_S - m_{Z'})^2} \sqrt{s - (m_S + m_{Z'})^2}}{16\pi s^{3/2} (s - 4m_-^2)^{3/2} m_{Z'}^2} \\
&\left\{ 4\sqrt{s} \coth^{-1} \left(\frac{\sqrt{s}(s - m_S^2 - m_{Z'}^2)}{\sqrt{s - 4m_-^2} \sqrt{s - (m_S - m_{Z'})^2} \sqrt{s - (m_S + m_{Z'})^2}} \right) \right. \\
&\times \left[4m_-(\delta m - m_-) m_{Z'}^6 + 40m_-^4 m_{Z'}^4 + 128m_-^5 (m_- + \delta m) m_{Z'}^2 + s(m_{Z'}^4 - 2m_-(m_- + 9\delta m) m_{Z'}^2) \right. \\
&- 16m_-^3 (7m_- + 4\delta m) m_{Z'}^2 + s^3 (m_{Z'}^2 - 2m_-(m_- + \delta m)) + 2s^2 (4m_-^4 + 4(2m_- + 3\delta m) m_{Z'}^2 m_- - m_{Z'}^4) \\
&+ m_S^4 (8m_-^4 - 2(2m_{Z'}^2 + s) m_-^2 + \delta m (4m_{Z'}^2 - 2s) m_- + s m_{Z'}^2) + 4m_S^2 (m_{Z'}^2 - s) [s(m_{Z'}^2 - m_-(m_- + \delta m)) \\
&+ 4m_-(m_-^3 - m_{Z'}^2 m_- + \delta m m_{Z'}^2)] \left. \right] \frac{1}{\sqrt{s - 4m_-^2} \sqrt{s - (m_S - m_{Z'})^2} (s - m_S^2 - m_{Z'}^2) \sqrt{s - (m_S + m_{Z'})^2}} \\
&+ 2 \left[(4m_-^2 - s) [m_-^2 m_S^4 + (s m_{Z'}^2 - 2m_-^2 (m_{Z'}^2 + s)) m_S^2 + m_-^2 (m_{Z'}^2 - s)^2] [m_-^2 (2m_{Z'}^2 - s) m_S^4 \right. \\
&- ((4m_-^4 + 6s m_{Z'}^2 - 2s^2) m_-^2 + s m_{Z'}^2 (s - 3m_{Z'}^2)) m_S^2 + m_-^2 (2m_{Z'}^6 - 9s m_{Z'}^4 + 4s(4m_-^2 + s) m_{Z'}^2 - s^3) \\
&+ m_- [(4(s - m_{Z'}^2) m_-^4 - s m_{Z'}^2 m_-^2) m_S^8 + 4m_-^2 (4(m_{Z'}^4 + s m_{Z'}^2 - s^2) m_-^2 + s m_{Z'}^2 (3s - 4m_{Z'}^2)) m_S^6 \\
&+ 2m_S^4 (32s m_{Z'}^2 m_-^6 - 4(3m_{Z'}^6 + s m_{Z'}^4 + 9s^2 m_{Z'}^2 - 3s^3) m_-^4 + s m_{Z'}^2 (17m_{Z'}^4 + 10s m_{Z'}^2 - 11s^2) m_-^2 \\
&- 6s^2 m_{Z'}^6 + 4s^3 m_{Z'}^4) - 4m_S^2 m_-^6 (32s m_{Z'}^2 (m_{Z'}^2 + s) - 4m_-^4 (m_{Z'}^8 - 3s m_{Z'}^6 + 8s^2 m_{Z'}^4 + 7s^3 m_{Z'}^2 - s^4) \\
&+ s m_{Z'}^2 (4m_{Z'}^6 - 11s m_{Z'}^4 + 22s^2 m_{Z'}^2 - 3s^3) m_-^2 - s^3 m_{Z'}^6) \\
&+ m_-^2 (m_{Z'}^2 - s)^2 (64s m_{Z'}^2 m_-^4 + 4(s^3 - 11s^2 m_{Z'}^2 + 7s m_{Z'}^4 - m_{Z'}^6) m_-^2 - s(m_{Z'}^3 - s m_{Z'}^2)^2) \left. \right] \\
&\times \left. \frac{1}{(m_-^2 m_S^4 + (s m_{Z'}^2 - 2m_-^2 (m_{Z'}^2 + s)) m_S^2 + m_-^2 (s - m_{Z'}^2)^2)^2} \right\} + \mathcal{O}((\delta m)^2), \tag{D14}
\end{aligned}$$

which is expanded by using $m_+ = m_- + \delta m$. Taking into account two annihilating particles in the non-relativistic limit, the cross section is approximated as

$$(\sigma v)_{\chi-\chi_+ \rightarrow Z' s} \simeq \frac{\delta m^2 c_\alpha^2 g_\chi^2 f^2}{32\pi m_-^4} + v^2 \frac{c_\alpha^2 g_\chi^2 f^2}{24\pi m_{Z'}^2} \left[1 + \mathcal{O} \left(\frac{\delta m^2}{m_-^2}, \frac{m_{Z'}^2}{m_-^2}, \frac{m_S^2}{m_-^2} \right) \right] + \mathcal{O}(\delta m^4, v^4), \tag{D15}$$

which is p -wave dominant for $\delta m \ll m_-$.

Appendix E: Kinetic decoupling of χ_\pm and S

Even after dark matter freezes out, both S and Z' particles remain in thermal equilibrium with the SM bath through the interactions $S \leftrightarrow Z' Z'$ and $Z' \leftrightarrow \nu_\mu \bar{\nu}_\mu, \nu_\tau \bar{\nu}_\tau$. As illustrated in Fig. 4, the

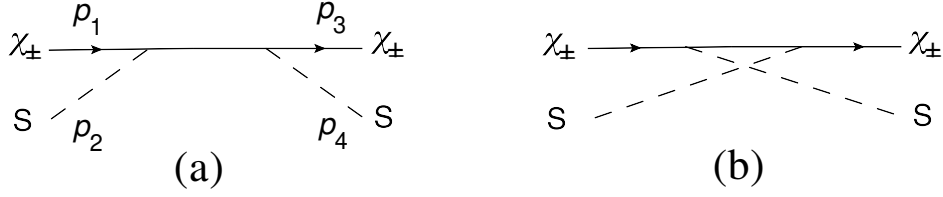


FIG. 13. Feynman diagrams for the $\chi_{\pm} S \rightarrow \chi_{\pm} S$ elastic scattering process, where the corresponding momenta p_i with $i = 1, 2, 3, 4$ are shown.

interaction $Z' \leftrightarrow e^+e^-$ facilitates the thermal connection between the (γ, e^{\pm}) and $(\nu_{\mu}, \nu_{\tau}, S, Z')$ baths, ensuring that $T = T_{\nu_{\mu}}$ is maintained until the temperature roughly drops below m_e . As the temperature drops, the S particles, which are exponentially suppressed by Boltzmann factors with a vanishing chemical potential, follow the temperature $T_{\nu_{\mu}}$.

In the following, we demonstrate that after freeze-out, dark matter particles can stay in kinetic equilibrium with the SM bath via elastic scatterings $\chi_{\pm} S \leftrightarrow \chi_{\pm} S$ for a certain period. This is because the $\chi_{\mp} S \rightarrow \chi_{\mp} S$ elastic scattering rate is proportional to the number density of S , which remains highly relativistic and is not Boltzmann suppressed once the temperature drops below T_f , compared to the process $\chi_{\mp}\chi_{\mp} \rightarrow SS$. We will show that χ_{\pm} with masses ranging from a few GeV to hundreds of GeV decouple from S at temperatures between 210 and 250 MeV. Basically, when studying the kinetic decoupling of χ_{\pm} from S , the S particles can be viewed as part of the thermal bath, sharing the same temperature as the photons.

Fig. 13 depicts the diagrams for elastic scattering $\chi_{\pm} S \rightarrow \chi_{\pm} S$, which are relevant for the kinetic energy transfer between χ_{\pm} and S . The u -channel diagram (on the right) is derived from the s -channel diagram (on the left) through crossing symmetry. For nonrelativistic dark matter, its temperature evolution follows the equation

$$\frac{dT_{\text{DM}}}{dt} + 2HT_{\text{DM}} = -\frac{1}{n} \sum_{i=+,-} 2n_i \gamma_i (T_{\text{DM}} - T) + \dots, \quad (\text{E1})$$

where $n = n_+ + n_-$, and $2\gamma_{\pm}$ is the average rate of kinetic energy transfer from S to χ_{\pm} at temperature T .

The γ_i values can be obtained by reformulating the thermally averaged collision term for elastic

scattering $\chi_{\pm}S \rightarrow \chi_{\pm}S$ using a semi-relativistic Fokker-Planck-like equation [117], expressed as

$$\begin{aligned} \gamma_i &= \frac{1}{6m_i T n_i} \int \prod_{\substack{j=1,2 \\ k=3,4}} d\Pi_j d\Pi_k f_j(T_j) (2\pi)^4 \delta^{(4)}(p_1 + p_2 - p_3 - p_4) |M|_{\chi_{\pm}S \rightarrow \chi_{\pm}S}^2 (-1)^{p_1 - p_4} (p_1 - p_4)^2 \\ &\simeq \frac{1}{6\pi^2 g_i m_i^2 T K_2(m_i/T_{\text{DM}})} \int_{(m_i+m_S)^2}^{\infty} ds \frac{(s - (m_i + m_S)^2)(s - (m_i - m_S)^2)}{4\sqrt{s}} K_1\left(\frac{\sqrt{s}}{T}\right) \\ &\quad \times \int \frac{d\sigma}{d\Omega} m_{\pm} v_{\pm}^2 (1 - \cos\theta) d\Omega, \end{aligned} \quad (\text{E2})$$

with $\gamma_+ \simeq \gamma_-$ and the distributions approximated by

$$f_i = e^{-(E_i - \mu_i)/T_i} (1 \pm f_i) \simeq e^{-(E_i - \mu_i)/T_i} = \frac{n_i}{n_i^{\text{eq}}(T_i)} e^{-E_i/T_i}, \quad (\text{E3})$$

where $n_S = n_S^{\text{eq}}(T)$, $T_S = T$, and $T_+ = T_- \equiv T_{\text{DM}}$.

The squared amplitude, $|M|_{\chi_{\pm}S \rightarrow \chi_{\pm}S}^2$, is summed over initial and final internal degrees of freedom, and

$$\begin{aligned} \int \frac{d\sigma}{d\Omega} m_{\pm} v_{\pm}^2 (1 - \cos\theta) d\Omega &= \frac{f^4}{48\pi(s - m_{\pm}^2)^2} \left[\frac{1}{s^3(m_{\pm}^2 s - (m_{\pm}^2 - m_S^2)^2)} \right. \\ &\quad \left(-2m_{\pm}^2(m_S^2 - m_{\pm}^2)^6 + s^5(5m_S^4 - 62m_S^2 m_{\pm}^2 + 231m_{\pm}^4) \right. \\ &\quad - s(m_S^4 - 22m_S^2 m_{\pm}^2 - 3m_{\pm}^4)(m_S^2 - m_{\pm}^2)^4 + 4s^4(4m_S^6 - 45m_S^4 m_{\pm}^2 + 47m_S^2 m_{\pm}^4 - 102m_{\pm}^6) \\ &\quad + 2m_{\pm}^2 s^3(96m_S^6 - 109m_S^4 m_{\pm}^2 + 18m_S^2 m_{\pm}^4 + 59m_{\pm}^6) \\ &\quad \left. + s^2(4m_S^6 - 87m_S^4 m_{\pm}^2 - 70m_S^2 m_{\pm}^4 + 57m_{\pm}^6)(m_S^2 - m_{\pm}^2)^2 + m_{\pm}^2 s^6 \right) \\ &\quad + \frac{6(s - m_{\pm}^2)}{m_S^4 - 2m_S^2(s + m_{\pm}^2) + (s - m_{\pm}^2)^2} \left(-4m_S^6 + m_S^4(s - 33m_{\pm}^2) + m_S^2(6m_{\pm}^4 + 60m_{\pm}^2 s - 2s^2) \right. \\ &\quad \left. + 31m_{\pm}^6 - 13m_{\pm}^4 s - 19m_{\pm}^2 s^2 + s^3 \right) \log \frac{s(s - 2m_S^2 - m_{\pm}^2)}{m_{\pm}^2 s - (m_{\pm}^2 - m_S^2)^2} \left. \right], \end{aligned} \quad (\text{E4})$$

which is Lorentz invariant even though the right-hand side is expressed in the center-of-mass frame with θ and v_{\pm} representing the scattering angle and velocity of χ_{\pm} , respectively. In Fig. 14, we show the kinetic energy injection rate from the thermal bath into dark matter via elastic scattering $\chi_{\pm}S \leftrightarrow \chi_{\pm}S$, compared to the cosmic cooling rate caused by Hubble expansion. Dark matter becomes kinetically decoupled from the thermal bath when $\gamma(\equiv \gamma_{\pm}) < H$. We find that χ_{\pm} with a mass of several GeV to hundreds of GeV kinetically decouples from S at a temperature roughly between 210 and 250 MeV. Meanwhile, this decoupling temperature is insensitive to m_S , which ranges from several MeV to hundreds of MeV.

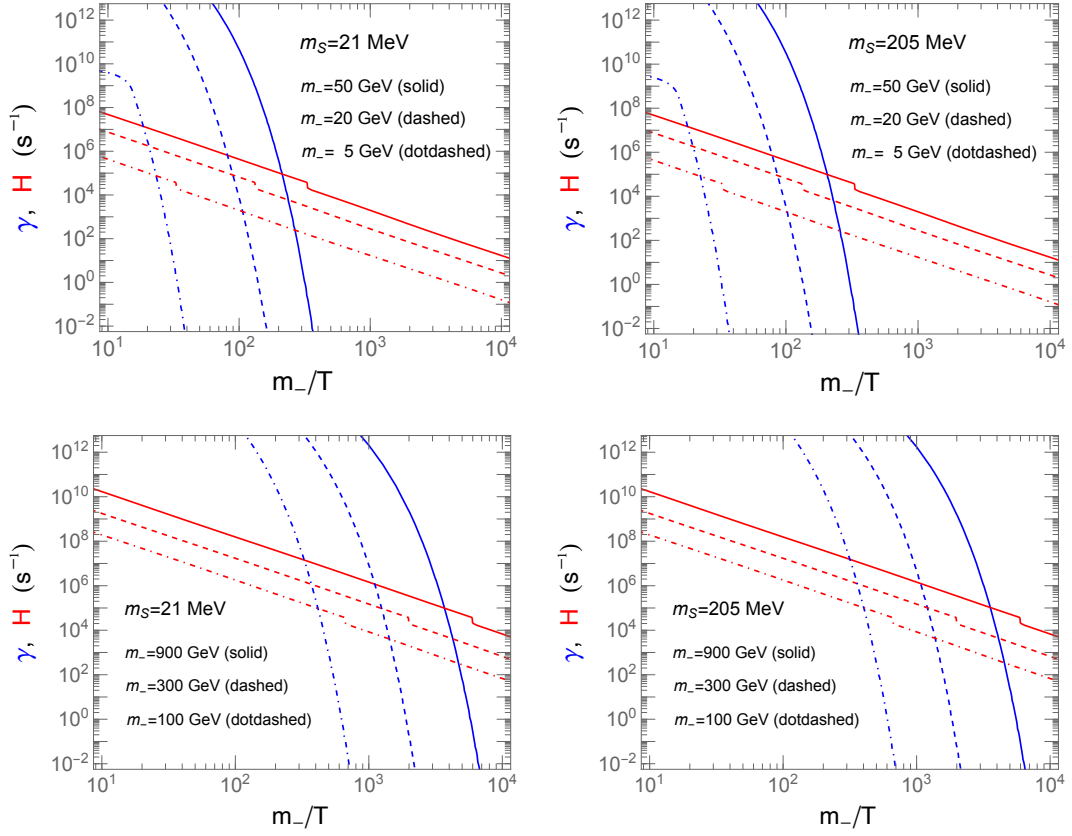


FIG. 14. Comparison of kinetic energy injection rates (blue), $\gamma \equiv \gamma_{\pm}$, from the thermal bath to dark matter via elastic scattering, $\chi_{\pm} S \rightarrow \chi_{\pm} S$, and the cooling rate due to Hubble expansion (red), H . Results are shown for different values of m_- , with m_S fixed at 21 MeV on the left and 205 MeV on the right. When $\gamma < H$, dark matter is kinetically decoupled from the thermal bath. All the decoupling temperatures are roughly between 210 and 250 MeV.

Appendix F: $\chi_+\chi_+ \rightarrow \chi_-\chi_-$

The annihilation cross section of $\chi_+\chi_+ \rightarrow \chi_-\chi_-$ with a Z' exchange in the t - and u - channels is given by⁶

$$\begin{aligned}
(\sigma v)_{\chi_+\chi_+ \rightarrow \chi_-\chi_-} = & \frac{\sqrt{s-4m_{\chi_-}^2}}{32\pi m_{Z'}^4 \sqrt{s}(s-2m_{\chi_+}^2)} \left\{ -9m_{\chi_+}^4 - 12m_{\chi_+}^3 m_{\chi_-} + 18m_{\chi_+}^2 m_{\chi_-}^2 + 20m_{\chi_+}^2 m_{Z'}^2 \right. \\
& + \left(-4m_{Z'}^2(m_{\chi_+}^2 - m_{\chi_-}^2)^2(5m_{\chi_+}^2 + 2m_{\chi_+} m_{\chi_-} + m_{\chi_-}^2) - 6(m_{\chi_+}^2 - m_{\chi_-}^2)^4 + 4m_{Z'}^8 \right. \\
& + 2m_{Z'}^4(23m_{\chi_+}^4 + 12m_{\chi_+}^3 m_{\chi_-} + 2m_{\chi_+}^2 m_{\chi_-}^2 - 4m_{\chi_+} m_{\chi_-}^3 - m_{\chi_-}^4) - 8m_{Z'}^6(3m_{\chi_+} - m_{\chi_-})(m_{\chi_+} + m_{\chi_-}) \left. \right) \\
& \frac{1}{m_{\chi_+}^4 - 2m_{\chi_+}^2(m_{\chi_-}^2 + m_{Z'}^2) + (m_{\chi_-}^2 - m_{Z'}^2)^2 + m_{Z'}^2 s} \\
& - \left[2 \left(9m_{\chi_+}^8 - 4m_{\chi_+}^7 m_{\chi_-} - 12m_{\chi_+}^6 m_{\chi_-}^2 - 18m_{\chi_+}^6 m_{Z'}^2 + 36m_{\chi_+}^5 m_{\chi_-}^3 - 8m_{\chi_+}^5 m_{\chi_-} m_{Z'}^2 \right. \right. \\
& + 6m_{\chi_+}^4 m_{\chi_-}^4 + 34m_{\chi_+}^4 m_{\chi_-}^2 m_{Z'}^2 - 9m_{\chi_+}^4 m_{Z'}^4 - 60m_{\chi_+}^3 m_{\chi_-}^5 - 16m_{\chi_+}^3 m_{\chi_-}^3 m_{Z'}^2 \\
& + 4m_{\chi_+}^3 m_{\chi_-} m_{Z'}^4 - 12m_{\chi_+}^2 m_{\chi_-}^6 - 78m_{\chi_+}^2 m_{\chi_-}^4 m_{Z'}^2 + 18m_{\chi_+}^2 m_{\chi_-}^2 m_{Z'}^4 + 12m_{\chi_+}^2 m_{Z'}^6 \\
& + 28m_{\chi_+} m_{\chi_-}^7 - 40m_{\chi_+} m_{\chi_-}^5 m_{Z'}^2 - 12m_{\chi_+} m_{\chi_-}^3 m_{Z'}^4 + 8m_{\chi_+} m_{\chi_-} m_{Z'}^6 - 2m_{Z'}^2 s^2 (m_{\chi_+} + m_{\chi_-})^2 \\
& + s \left(4m_{Z'}^4 (m_{\chi_+} - m_{\chi_-})(3m_{\chi_+} + 5m_{\chi_-}) + m_{Z'}^2 (m_{\chi_+} + m_{\chi_-})^2 (m_{\chi_+} + 3m_{\chi_-})^2 \right. \\
& \left. \left. - (m_{\chi_+} - m_{\chi_-})^2 (m_{\chi_+} + m_{\chi_-})^3 (15m_{\chi_+} + 7m_{\chi_-}) - 12m_{Z'}^6 \right) + 9m_{\chi_-}^8 - 2m_{\chi_-}^6 m_{Z'}^2 \right. \\
& \left. + 31m_{\chi_-}^4 m_{Z'}^4 + 12m_{\chi_-}^2 m_{Z'}^6 - 8m_{Z'}^8 \right) \log \left(\frac{2m_{\chi_+}^2 + 2m_{\chi_-}^2 - 2m_{Z'}^2 - s - \sqrt{s-4m_{\chi_+}^2} \sqrt{s-4m_{\chi_-}^2}}{2m_{\chi_+}^2 + 2m_{\chi_-}^2 - 2m_{Z'}^2 - s + \sqrt{s-4m_{\chi_+}^2} \sqrt{s-4m_{\chi_-}^2}} \right) \left. \right] \\
& \times \frac{1}{\sqrt{s-4m_{\chi_+}^2} \sqrt{s-4m_{\chi_-}^2} (2(m_{\chi_+}^2 + m_{\chi_-}^2 - m_{Z'}^2) - s)} \\
& \left. + 36m_{\chi_+} m_{\chi_-}^3 + 8m_{\chi_+} m_{\chi_-} m_{Z'}^2 + 15m_{\chi_-}^4 - 12m_{\chi_-}^2 m_{Z'}^2 + 4m_{Z'}^4 + 8m_{Z'}^2 s \right\}. \tag{F2}
\end{aligned}$$

The chemical equilibrium between χ_+ and χ_- can be reached not only through reactions of $\chi_+\chi_+ \leftrightarrow SS$ and $\chi_-\chi_- \leftrightarrow SS$, but also via direct annihilation of $\chi_+\chi_+ \leftrightarrow \chi_-\chi_-$. However, the former reaction ends at the freeze-out temperature. Here, we will estimate the decoupling temperature of the latter. When the increase rate of χ_+ from $\chi_-\chi_- \rightarrow \chi_+\chi_+$ is less than its dilution rate from Hubble expansion, the reaction becomes inactive. We can estimate this decoupling temperature using the sudden decoupling approximation, which roughly satisfies $\langle \sigma v \rangle_{\chi_+\chi_+ \rightarrow \chi_-\chi_-} (n_{\chi_+}^{\text{eq}})^2 \approx H n_{\chi_+}$, where the detailed balance $\langle \sigma v \rangle_{\chi_-\chi_- \rightarrow \chi_+\chi_+} (n_{\chi_-}^{\text{eq}})^2 = \langle \sigma v \rangle_{\chi_+\chi_+ \rightarrow \chi_-\chi_-} (n_{\chi_+}^{\text{eq}})^2$ has been used.

⁶ The annihilation process, $\chi_+\chi_+ \rightarrow \chi_-\chi_-$, can also occur through the exchange of S scalar particles in the s -channel. However, this contribution is much smaller than the one from exchanging Z' scalar particles in the t - and u -channels. For reference, we present the cross-section considering only the interaction mediated by an s -channel scalar particle,

$$(\sigma v)_{\chi_+\chi_+ \rightarrow S^* \rightarrow \chi_-\chi_-} = \frac{f^4 (s-4m_-^2)^{3/2} (s-4m_+^2)}{32\pi \sqrt{s} (s-2m_+^2) ((s-m_S^2)^2 + \Gamma_S^2 m_S^2)}. \tag{F1}$$

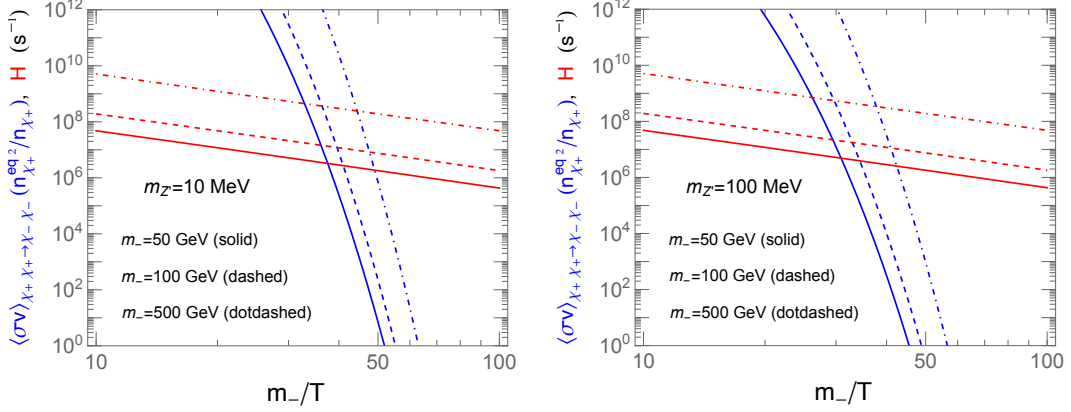


FIG. 15. Comparison of $\chi_+\chi_+ \rightarrow \chi_-\chi_-$ annihilation rates (blue), $\langle\sigma v\rangle_{\chi_+\chi_+\rightarrow\chi_-\chi_-} n_{\chi_+}^{\text{eq}}$, and the Hubble expansion rate (red), H . Results are shown for different values of m_- , with $m_{Z'}$ fixed at 10 MeV on the left and 100 MeV on the right. The decoupling of χ_+ from χ_- occurs below the dark matter freeze-out temperature, approximately when m_-/T ranges from 30 to 50. The decoupling time, proportional to H^{-1} , is about 10^{-8} to 10^{-6} seconds.

Using the $g_{\mu\tau}$ value that fits the $(g-2)_\mu$ experimental results, and approximating

$$n_{\chi_+}(T) \approx n_{\chi_+}^{\text{eq}}(T_{\text{fo}}) \left(\frac{a_{\text{freeze-out}}}{a}\right)^3 \approx n_{\chi_+}^{\text{eq}}(T_{\text{fo}}) \left(\frac{T}{T_{\text{fo}}}\right)^3 \quad (\text{F3})$$

at a later time with temperature T after freeze-out, where T_{fo} is the freeze-out temperature, Fig. 15 shows the results for some typical parameter sets. We set δm to 100 eV and consider $m_{Z'}$ values of 10 and 100 MeV, along with m_- values of 10, 50, and 500 GeV. These parameter choices adequately represent the overall outcomes for $m_{Z'}$, ranging from a few MeV to several hundred MeV, and m_- from a few GeV up to nearly 1,000 GeV. The decoupling of χ_+ from χ_- occurs below the dark matter freeze-out temperature, approximately when m_-/T ranges from 30 to 50. The age of the Universe can be estimated from the inverse of the Hubble expansion rate. This conclusion also applies to δm with a value from a few eV to hundreds of eV, which is the range of interest.

Appendix G: Constraint from Super-Kamiokande on the neutrino excess caused by dark matter annihilations

This appendix provides additional details on the upper limit of the DM neutrino excess, derived from the Super-Kamiokande on-off source analysis described in the main text [63, 64]. The maximum neutrino excess should occur in the on-source region, centered around the Galactic center, while the off-source region, of equal size, is offset by 180° in right ascension of equatorial coor-

dinates. Consequently, the difference in the number of neutrino events (ΔN^{sig}) between on- and off-source regions results from DM annihilations. The 90% C.L. upper limit for $\Delta N_{90}^{\text{sig}}$ is provided separately for μ -like event samples categorized as FC SubGeV, FC MultiGeV, PC, and UP- μ [64], which correspond to the measured neutrino energy ranges of approximately 0.1–1 GeV, 1–5 GeV, 5–50 GeV, and greater than 50 GeV, respectively [65]. The upper limit on $\langle\sigma v\rangle_{SS} \equiv \langle\sigma v\rangle_{\chi_{\mp}\chi_{\mp}\rightarrow SS}$ can be derived from the relation,

$$\begin{aligned}\Delta N_{90}^{\text{sig}} &= T_{\text{live}}\Delta\Omega \int dE A_{\text{eff}}(E) \frac{d\Phi_{\nu}}{dE}, \\ T_{\text{live}} &= \frac{N_{\text{atm}}}{\int dE A_{\text{eff}}(E) \frac{d\Phi_{\text{atm}}}{dE} \Delta\Omega},\end{aligned}\quad (\text{G1})$$

where $\Delta\Omega$ denotes the solid angle of the on-source region for each event sample, N_{atm} is the number of atmospheric muon neutrinos in the off-source region for each sample (see Table 8.2 of Ref. [64]), which are mainly background events, the corresponding flux is $d\Phi_{\text{atm}}/dE$ (shown in Fig. 7 of Ref. [65]), and T_{live} represents the live time.

The effective area depends on the fiducial volume of the water Cherenkov detector and the scattering cross section. The latter is roughly proportional to the incident neutrino energy [118]. Assuming the effective area scales as $\sim E^{\beta}$, then $\beta=0$ to 1 has little effect on the upper limit of $\langle\sigma v\rangle$. This variation is only slightly noticeable at higher m_{-} . When $\beta = 0$, the limit at $m_{-} = 300$ GeV is 1.3 times weaker than with $\beta = 1$, but at $m_{-} = 1000$ GeV, it is 2.7 times weaker. Here, we use $\beta = 1$

The differential “muon neutrino” flux, resulting from the two-step annihilation of DM [66–69], can be expressed as

$$\frac{d\Phi_{\nu}}{dE} \simeq \frac{1}{8\pi m_{-}^2} \langle\sigma v\rangle_{SS} \frac{dN_{\nu}}{dE} \frac{1}{\Delta\Omega} \underbrace{\int_{\Delta\Omega} \int_{\text{l.o.s.}} ds \rho^2(r(s, \psi)) d\Omega}_{\text{J-factor}}, \quad (\text{G2})$$

where the J-factor is the integral of the DM density squared along the line of sight (l.o.s.) and over the solid angle $\Delta\Omega$ that covers the on-source region. dN_{ν}/dE represents the muon neutrino spectrum per DM annihilation. The DM particles annihilate into two scalar mediators, each decaying into two Z' particles. Finally, two neutrinos are produced in the decay of each Z' as a result. Since the neutrinos produced in the DM annihilation involve intermediate steps, the spectrum generated from Z' decays is boosted and becomes broader,

$$\begin{aligned}\frac{dN_{\nu}}{dE} &= \frac{4}{m_{-}} \int_{t_{2,\text{min}}}^{t_{2,\text{max}}} \frac{dx_1}{x_1 \sqrt{1-\epsilon_2^2}} \int_{t_{1,\text{min}}}^{t_{1,\text{max}}} \frac{dx_0}{x_0 \sqrt{1-\epsilon_1^2}} \frac{dN_{\nu}^{Z'}}{dx_0} \\ &= \frac{16/5}{m_{-} \sqrt{1-\epsilon_2^2} \sqrt{1-\epsilon_1^2}} \int_{t_{2,\text{min}}}^{t_{2,\text{max}}} \frac{dx_1}{x_1},\end{aligned}\quad (\text{G3})$$

where

$$\epsilon_2 = \frac{m_S}{m_-}, \quad \epsilon_1 = \frac{2m_{Z'}}{m_S}, \quad (\text{G4})$$

$$t_{1,\max} = \min\left[1, \frac{2x_1}{\epsilon_1^2} \left(1 + \sqrt{1 - \epsilon_1^2}\right)\right], \quad t_{1,\min} = \frac{2x_1}{\epsilon_1^2} \left(1 - \sqrt{1 - \epsilon_1^2}\right), \quad (\text{G5})$$

$$t_{2,\max} = \min\left[\frac{1}{2} \left(1 + \sqrt{1 - \epsilon_1^2}\right), \frac{2E}{\epsilon_2^2 m_-} \left(1 + \sqrt{1 - \epsilon_2^2}\right)\right], \quad t_{2,\min} = \frac{2E}{\epsilon_2^2 m_-} \left(1 - \sqrt{1 - \epsilon_2^2}\right), \quad (\text{G6})$$

$$0 \leq E \leq \frac{m_-}{4} \left(1 + \sqrt{1 - \epsilon_1^2}\right) \left(1 + \sqrt{1 - \epsilon_2^2}\right), \quad x_1 = \frac{2E_1}{m_S}, \quad x_0 = \frac{2E_0}{m_{Z'}}, \quad (\text{G7})$$

with E , E_1 , and E_0 being the neutrino energy in the center-of-mass frame of the DM pair, S rest frame, and Z' rest frame, respectively. In this case, $dN_{\nu}^{Z'}/dx_0 = 2 \times \frac{2}{5} \delta(x_0 - 1)$, where the factor of 2 accounts for each Z' decay producing two neutrinos. The $2/5$ factor reflects the flavor ratio of neutrinos from the Z' decay in the $L_\mu - L_\tau$ model, which is $\nu_e : \nu_\mu : \nu_\tau = 0 : 1 : 1$; consequently, the neutrino flux ratio observed at Earth becomes $1 : 2 : 2$ [71] when considering current oscillation parameters [70].

We use the original Navarro-Frenk-White (NFW) profile with $\gamma = 1$ [119, 120],

$$\rho(r) = \rho_\odot \left(\frac{r}{r_\odot}\right)^{-\gamma} \left(\frac{1 + r/r_s}{1 + r_\odot/r_s}\right)^{\gamma-3}, \quad (\text{G8})$$

to describe the DM density distribution in the Galactic halo, where $r_s = 20$ kpc is the scale radius, r is the distance to the GC. We take the DM density $\rho_\odot = 0.35$ GeV in the location of the Sun $r_\odot = 8.5$ kpc in the analysis. The variation of γ can change the inner slope of the profile.

Thus, the bound of $\langle\sigma v\rangle_{SS}$ vs. m_- can be obtained from the fit.

-
- [1] D. Tucker-Smith and N. Weiner, “Inelastic dark matter,” *Phys. Rev. D* **64**, 043502 (2001) [arXiv:hep-ph/0101138 [hep-ph]].
 - [2] D. Tucker-Smith and N. Weiner, “The Status of inelastic dark matter,” *Phys. Rev. D* **72**, 063509 (2005) [arXiv:hep-ph/0402065 [hep-ph]].
 - [3] B. Batell, M. Pospelov and A. Ritz, “Direct Detection of Multi-component Secluded WIMPs,” *Phys. Rev. D* **79**, 115019 (2009) [arXiv:0903.3396 [hep-ph]].
 - [4] S. Chang, N. Weiner and I. Yavin, “Magnetic Inelastic Dark Matter,” *Phys. Rev. D* **82**, 125011 (2010) [arXiv:1007.4200 [hep-ph]].
 - [5] N. Okada and O. Seto, “Inelastic extra $U(1)$ charged scalar dark matter,” *Phys. Rev. D* **101**, no.2, 023522 (2020) [arXiv:1908.09277 [hep-ph]].
 - [6] G. Dalla Valle Garcia, “A minimalistic model for inelastic dark matter,” *Phys. Lett. B* **862**, 139320 (2025) [arXiv:2411.02147 [hep-ph]].

- [7] X. G. Wang and A. W. Thomas, “A Viable New Model for Dark Matter,” [arXiv:2510.24114 [hep-ph]].
- [8] N. Arkani-Hamed, D. P. Finkbeiner, T. R. Slatyer and N. Weiner, “A Theory of Dark Matter,” *Phys. Rev. D* **79**, 015014 (2009) [arXiv:0810.0713 [hep-ph]].
- [9] M. Pospelov and A. Ritz, “Astrophysical Signatures of Secluded Dark Matter,” *Phys. Lett. B* **671**, 391-397 (2009) [arXiv:0810.1502 [hep-ph]].
- [10] D. P. Finkbeiner, T. R. Slatyer, N. Weiner and I. Yavin, “PAMELA, DAMA, INTEGRAL and Signatures of Metastable Excited WIMPs,” *JCAP* **09**, 037 (2009) [arXiv:0903.1037 [hep-ph]].
- [11] R. A. Gustafson, G. Herrera, M. Mukhopadhyay, K. Murase and I. M. Shoemaker, “Cosmic-ray cooling in active galactic nuclei as a new probe of inelastic dark matter,” *Phys. Rev. D* **111**, no.12, L121303 (2025) [arXiv:2408.08947 [hep-ph]].
- [12] A. Berlin, J. W. Foster, D. Hooper and G. Krnjaic, “dSphobic Dark Matter,” [arXiv:2504.12372 [hep-ph]].
- [13] D. Hooper, G. Krnjaic, D. Rocha and S. Roy, “Gamma-Rays and Gravitational Waves from Inelastic Higgs Portal Dark Matter,” [arXiv:2507.22975 [hep-ph]].
- [14] A. Berlin, G. Krnjaic and E. Pinetti, “Reviving MeV-GeV indirect detection with inelastic dark matter,” *Phys. Rev. D* **110**, no.3, 035015 (2024) [arXiv:2311.00032 [hep-ph]].
- [15] G. Krnjaic, D. McKeen, R. Mizuta, G. Mohlabeng, D. E. Morrissey and D. Tuckler, “X-rays from Inelastic Dark Matter Freeze-in,” [arXiv:2509.19428 [hep-ph]].
- [16] E. Izaguirre, G. Krnjaic and B. Shuve, “Discovering Inelastic Thermal-Relic Dark Matter at Colliders,” *Phys. Rev. D* **93**, no.6, 063523 (2016) [arXiv:1508.03050 [hep-ph]].
- [17] A. Berlin and F. Kling, “Inelastic Dark Matter at the LHC Lifetime Frontier: ATLAS, CMS, LHCb, CODEX-b, FASER, and MATHUSLA,” *Phys. Rev. D* **99**, no.1, 015021 (2019) [arXiv:1810.01879 [hep-ph]].
- [18] I. V. Voronchikhin and D. V. Kirpichnikov, “Examining scalar portal inelastic dark matter with lepton fixed target experiments,” [arXiv:2505.04290 [hep-ph]].
- [19] G. Krnjaic, D. Rocha and I. R. Wang, “Discovering Dark Matter with the MUonE Experiment,” *Phys. Rev. Lett.* **134**, no.16, 161801 (2025) [arXiv:2409.00170 [hep-ph]].
- [20] G. D. V. Garcia, F. Kahlhoefer, M. Ovchinnikov and T. Schwetz, “Not-so-inelastic Dark Matter,” *JHEP* **02**, 127 (2025) [arXiv:2405.08081 [hep-ph]].
- [21] A. M. Abdullahi, M. Hostert, D. Massaro and S. Pascoli, “Semi-Visible Dark Photon Phenomenology at the GeV Scale,” *Phys. Rev. D* **108**, no.1, 015032 (2023) [arXiv:2302.05410 [hep-ph]].
- [22] M. Carrillo González and N. Toro, “Cosmology and signals of light pseudo-Dirac dark matter,” *JHEP* **04**, 060 (2022) [arXiv:2108.13422 [hep-ph]].
- [23] S. Heeba, T. Lin and K. Schutz, “Inelastic freeze-in,” *Phys. Rev. D* **108**, no.9, 095016 (2023) [arXiv:2304.06072 [hep-ph]].
- [24] N. Brahma, S. Heeba and K. Schutz, “Resonant pseudo-Dirac dark matter as a sub-GeV thermal

- target,” Phys. Rev. D **109**, no.3, 035006 (2024) [arXiv:2308.01960 [hep-ph]].
- [25] S. Tulin and H. B. Yu, “Dark Matter Self-interactions and Small Scale Structure,” Phys. Rept. **730**, 1-57 (2018) [arXiv:1705.02358 [hep-ph]].
- [26] S. Adhikari, A. Banerjee, K. K. Boddy, F. Y. Cyr-Racine, H. Desmond, C. Dvorkin, B. Jain, F. Kahlhoefer, M. Kaplinghat and A. Nierenberg, *et al.* “Astrophysical Tests of Dark Matter Self-Interactions,” [arXiv:2207.10638 [astro-ph.CO]].
- [27] M. Kaplinghat, S. Tulin and H. B. Yu, “Dark Matter Halos as Particle Colliders: Unified Solution to Small-Scale Structure Puzzles from Dwarfs to Clusters,” Phys. Rev. Lett. **116**, no.4, 041302 (2016) [arXiv:1508.03339 [astro-ph.CO]].
- [28] F. Jegerlehner and A. Nyffeler, “The Muon $g-2$,” Phys. Rept. **477**, 1-110 (2009) [arXiv:0902.3360 [hep-ph]].
- [29] W. Altmannshofer, S. Gori, S. Profumo and F. S. Queiroz, “Explaining dark matter and B decay anomalies with an $L_\mu - L_\tau$ model,” JHEP **12**, 106 (2016) [arXiv:1609.04026 [hep-ph]].
- [30] A. Kamada, K. Kaneta, K. Yanagi and H. B. Yu, “Self-interacting dark matter and muon $g - 2$ in a gauged $U(1)_{L_\mu-L_\tau}$ model,” JHEP **06**, 117 (2018) [arXiv:1805.00651 [hep-ph]].
- [31] P. Foldenauer, “Light dark matter in a gauged $U(1)_{L_\mu-L_\tau}$ model,” Phys. Rev. D **99**, no.3, 035007 (2019) [arXiv:1808.03647 [hep-ph]].
- [32] M. Escudero, D. Hooper, G. Krnjaic and M. Pierre, “Cosmology with A Very Light $L_\mu - L_\tau$ Gauge Boson,” JHEP **03**, 071 (2019) [arXiv:1901.02010 [hep-ph]].
- [33] K. Asai, S. Okawa and K. Tsumura, “Search for $U(1)_{L_\mu-L_\tau}$ charged dark matter with neutrino telescope,” JHEP **03**, 047 (2021) [arXiv:2011.03165 [hep-ph]].
- [34] D. Borah, M. Dutta, S. Mahapatra and N. Sahu, “Muon ($g - 2$) and XENON1T excess with boosted dark matter in $L_\mu - L_\tau$ model,” Phys. Lett. B **820**, 136577 (2021) [arXiv:2104.05656 [hep-ph]].
- [35] I. Holst, D. Hooper and G. Krnjaic, “Simplest and Most Predictive Model of Muon $g-2$ and Thermal Dark Matter,” Phys. Rev. Lett. **128**, no.14, 141802 (2022) [arXiv:2107.09067 [hep-ph]].
- [36] M. Drees and W. Zhao, “ $U(1)_{L_\mu-L_\tau}$ for light dark matter, $g_\mu - 2$, the 511 keV excess and the Hubble tension,” Phys. Lett. B **827**, 136948 (2022) [arXiv:2107.14528 [hep-ph]].
- [37] T. Hapitas, D. Tuckler and Y. Zhang, “General kinetic mixing in gauged $U(1)_{L_\mu-L_\tau}$ model for muon $g-2$ and dark matter,” Phys. Rev. D **105**, no.1, 016014 (2022) [arXiv:2108.12440 [hep-ph]].
- [38] P. Figueroa, G. Herrera and F. Ochoa, “Direct detection of light dark matter charged under a $L_\mu-L_\tau$ symmetry,” Phys. Rev. D **110**, no.9, 095018 (2024) [arXiv:2404.03090 [hep-ph]].
- [39] K. Asai, K. Hamaguchi, N. Nagata, S. Y. Tseng and J. Wada, “Probing the $L_\mu-L_\tau$ gauge boson at the MUonE experiment,” Phys. Rev. D **106**, no.5, L051702 (2022) [arXiv:2109.10093 [hep-ph]].
- [40] L. Zu, X. Pan, L. Feng, Q. Yuan and Y. Z. Fan, “Constraining $U(1)_{L_\mu-L_\tau}$ charged dark matter model for muon $g - 2$ anomaly with AMS-02 electron and positron data,” JCAP **08**, no.08, 028 (2022) [arXiv:2104.03340 [hep-ph]].
- [41] D. P. Aguillard *et al.* [Muon $g-2$], “Measurement of the Positive Muon Anomalous Magnetic Moment

- to 0.20 ppm,” Phys. Rev. Lett. **131**, no.16, 161802 (2023) [arXiv:2308.06230 [hep-ex]].
- [42] D. P. Aguillard *et al.* [Muon g-2], “Detailed report on the measurement of the positive muon anomalous magnetic moment to 0.20 ppm,” Phys. Rev. D **110**, no.3, 032009 (2024) [arXiv:2402.15410 [hep-ex]].
- [43] G. W. Bennett *et al.* [Muon g-2], “Final Report of the Muon E821 Anomalous Magnetic Moment Measurement at BNL,” Phys. Rev. D **73**, 072003 (2006) [arXiv:hep-ex/0602035 [hep-ex]].
- [44] T. Aoyama, N. Asmussen, M. Benayoun, J. Bijnens, T. Blum, M. Bruno, I. Caprini, C. M. Carloni Calame, M. Cè and G. Colangelo, *et al.* “The anomalous magnetic moment of the muon in the Standard Model,” Phys. Rept. **887**, 1-166 (2020) [arXiv:2006.04822 [hep-ph]].
- [45] C. Davies, “Muon g-2,” PoS **LATTICE2024**, 019 (2025) [arXiv:2503.03364 [hep-lat]].
- [46] R.L. Workman *et al.* (Particle Data Group), Prog. Theor. Exp. Phys. 2022, 083C01 (2022).
- [47] J. P. Lees *et al.* [BaBar], “Search for a muonic dark force at BABAR,” Phys. Rev. D **94**, no.1, 011102 (2016) [arXiv:1606.03501 [hep-ex]].
- [48] S. R. Mishra *et al.* [CCFR], “Neutrino Tridents and W Z Interference,” Phys. Rev. Lett. **66**, 3117-3120 (1991)
- [49] W. Altmannshofer, S. Gori, M. Pospelov and I. Yavin, “Neutrino Trident Production: A Powerful Probe of New Physics with Neutrino Beams,” Phys. Rev. Lett. **113**, 091801 (2014) [arXiv:1406.2332 [hep-ph]].
- [50] M. Bauer, P. Foldenauer and J. Jaeckel, “Hunting All the Hidden Photons,” JHEP **07**, 094 (2018) [arXiv:1803.05466 [hep-ph]].
- [51] H. K. Dreiner, J. F. Fortin, J. Isern and L. Ubaldi, “White Dwarfs constrain Dark Forces,” Phys. Rev. D **88**, 043517 (2013) [arXiv:1303.7232 [hep-ph]].
- [52] G. Bellini, J. Benziger, D. Bick, S. Bonetti, G. Bonfini, M. Buizza Avanzini, B. Caccianiga, L. Cadonati, F. Calaprice and C. Carraro, *et al.* “Precision measurement of the 7Be solar neutrino interaction rate in Borexino,” Phys. Rev. Lett. **107**, 141302 (2011) [arXiv:1104.1816 [hep-ex]].
- [53] N. Aghanim *et al.* [Planck], “Planck 2018 results. VI. Cosmological parameters,” Astron. Astrophys. **641**, A6 (2020) [erratum: Astron. Astrophys. **652**, C4 (2021)] [arXiv:1807.06209 [astro-ph.CO]].
- [54] J. Edsjo and P. Gondolo, “Neutralino relic density including coannihilations,” Phys. Rev. D **56**, 1879-1894 (1997) [arXiv:hep-ph/9704361 [hep-ph]].
- [55] D. G. Cerdeno, T. Delahaye and J. Lavalle, Nucl. Phys. B **854**, 738-779 (2012) [arXiv:1108.1128 [hep-ph]].
- [56] P. Gondolo and G. Gelmini, “Cosmic abundances of stable particles: Improved analysis,” Nucl. Phys. B **360**, 145 (1991).
- [57] K. C. Yang, “Freeze-out forbidden dark matter in the hidden sector in the mass range from sub-GeV to TeV,” JHEP **11**, 083 (2022) [arXiv:2209.10827 [hep-ph]].
- [58] S. Vagnozzi, “New physics in light of the H_0 tension: An alternative view,” Phys. Rev. D **102**, no.2, 023518 (2020) [arXiv:1907.07569 [astro-ph.CO]].

- [59] E. Di Valentino, O. Mena, S. Pan, L. Visinelli, W. Yang, A. Melchiorri, D. F. Mota, A. G. Riess and J. Silk, “In the realm of the Hubble tension—a review of solutions,” *Class. Quant. Grav.* **38**, no.15, 153001 (2021) [arXiv:2103.01183 [astro-ph.CO]].
- [60] M. Kawasaki, K. Kohri and N. Sugiyama, “MeV scale reheating temperature and thermalization of neutrino background,” *Phys. Rev. D* **62**, 023506 (2000) [astro-ph/0002127].
- [61] R. Iengo, “Sommerfeld enhancement for a Yukawa potential,” [arXiv:0903.0317 [hep-ph]].
- [62] R. Iengo, “Sommerfeld enhancement: General results from field theory diagrams,” *JHEP* **05**, 024 (2009) [arXiv:0902.0688 [hep-ph]].
- [63] K. Abe *et al.* [Super-Kamiokande], “Indirect search for dark matter from the Galactic Center and halo with the Super-Kamiokande detector,” *Phys. Rev. D* **102**, no.7, 072002 (2020) [arXiv:2005.05109 [hep-ex]].
- [64] K. Frankiewicz, “Indirect Search for Dark Matter with the Super-Kamiokande Detector”, Ph.D. thesis, National Centre For Nuclear Research, Poland, Apr. 2018.
- [65] E. Richard *et al.* [Super-Kamiokande], “Measurements of the atmospheric neutrino flux by Super-Kamiokande: energy spectra, geomagnetic effects, and solar modulation,” *Phys. Rev. D* **94**, no.5, 052001 (2016) [arXiv:1510.08127 [hep-ex]].
- [66] G. Elor, N. L. Rodd and T. R. Slatyer, “Multistep cascade annihilations of dark matter and the Galactic Center excess,” *Phys. Rev. D* **91**, 103531 (2015) [arXiv:1503.01773 [hep-ph]].
- [67] K. C. Yang, “Search for Scalar Dark Matter via Pseudoscalar Portal Interactions: In Light of the Galactic Center Gamma-Ray Excess,” *Phys. Rev. D* **97**, no.2, 023025 (2018) [arXiv:1711.03878 [hep-ph]].
- [68] K. C. Yang, “Hidden Higgs portal vector dark matter for the Galactic center gamma-ray excess from the two-step cascade annihilation, and muon $g - 2$,” *JHEP* **08**, 099 (2018) [arXiv:1806.05663 [hep-ph]].
- [69] K. C. Yang, “A potentially detectable gamma-ray line in the Fermi Galactic center excess — in light of one-step cascade annihilations of secluded (vector) dark matter via the Higgs portal,” *JHEP* **07**, 148 (2020) [arXiv:2001.04946 [hep-ph]].
- [70] M. Maltoni, T. Schwetz, M. A. Tortola and J. W. F. Valle, “Status of global fits to neutrino oscillations,” *New J. Phys.* **6**, 122 (2004) [arXiv:hep-ph/0405172 [hep-ph]].
- [71] S. Palomares-Ruiz and S. Pascoli, “Testing MeV dark matter with neutrino detectors,” *Phys. Rev. D* **77**, 025025 (2008) [arXiv:0710.5420 [astro-ph]].
- [72] S. Adrian-Martinez *et al.* [ANTARES], “Search of Dark Matter Annihilation in the Galactic Centre using the ANTARES Neutrino Telescope,” *JCAP* **10**, 068 (2015) [arXiv:1505.04866 [astro-ph.HE]].
- [73] C. A. Argüelles, A. Diaz, A. Kheirandish, A. Olivares-Del-Campo, I. Safa and A. C. Vincent, “Dark matter annihilation to neutrinos,” *Rev. Mod. Phys.* **93**, no.3, 035007 (2021) [arXiv:1912.09486 [hep-ph]].
- [74] F. Bergsma *et al.* [CHARM], “Search for Axion Like Particle Production in 400-GeV Proton -

- Copper Interactions,” Phys. Lett. B **157**, 458-462 (1985)
- [75] M. W. Winkler, “Decay and detection of a light scalar boson mixing with the Higgs boson,” Phys. Rev. D **99**, no.1, 015018 (2019) [arXiv:1809.01876 [hep-ph]].
- [76] G. Bernardi, G. Carugno, J. Chauveau, F. Dicarolo, M. Dris, J. Dumarchez, M. Ferro-Luzzi, J. M. Levy, D. Lukas and J. M. Perreau, *et al.* “Search for Neutrino Decay,” Phys. Lett. B **166**, 479-483 (1986)
- [77] G. Bernardi, G. Carugno, J. Chauveau, F. Dicarolo, M. Dris, J. Dumarchez, M. Ferro-Luzzi, J. M. Levy, D. Lukas and J. M. Perreau, *et al.* “Anomalous Electron Production Observed in the CERN Ps Neutrino Beam,” Phys. Lett. B **181**, 173-177 (1986)
- [78] G. Bernardi, G. Carugno, J. Chauveau, F. Dicarolo, M. Dris, J. Dumarchez, M. Ferro-Luzzi, J. M. Levy, D. Lukas and J. M. Perreau, *et al.* “FURTHER LIMITS ON HEAVY NEUTRINO COUPLINGS,” Phys. Lett. B **203**, 332-334 (1988)
- [79] D. Gorbunov, I. Krasnov and S. Suvorov, “Constraints on light scalars from PS191 results,” Phys. Lett. B **820**, 136524 (2021) [arXiv:2105.11102 [hep-ph]].
- [80] A. V. Artamonov *et al.* [BNL-E949], “Study of the decay $K^+ \rightarrow \pi^+ \nu \bar{\nu}$ in the momentum region $140 < P_\pi < 199$ MeV/c,” Phys. Rev. D **79**, 092004 (2009) [arXiv:0903.0030 [hep-ex]].
- [81] E. Cortina Gil *et al.* [NA62], “Measurement of the very rare $K^+ \rightarrow \pi^+ \nu \bar{\nu}$ decay,” JHEP **06**, 093 (2021) [arXiv:2103.15389 [hep-ex]].
- [82] E. Cortina Gil *et al.* [NA62], “Search for π^0 decays to invisible particles,” JHEP **02**, 201 (2021) [arXiv:2010.07644 [hep-ex]].
- [83] J. Beacham, C. Burrage, D. Curtin, A. De Roeck, J. Evans, J. L. Feng, C. Gatto, S. Gninenko, A. Hartin and I. Irastorza, *et al.* “Physics Beyond Colliders at CERN: Beyond the Standard Model Working Group Report,” J. Phys. G **47**, no.1, 010501 (2020) [arXiv:1901.09966 [hep-ex]].
- [84] E. Cortina Gil *et al.* [NA62], “The Beam and detector of the NA62 experiment at CERN,” JINST **12**, no.05, P05025 (2017) [arXiv:1703.08501 [physics.ins-det]].
- [85] S. Alekhin, W. Altmannshofer, T. Asaka, B. Batell, F. Bezrukov, K. Bondarenko, A. Boyarsky, K. Y. Choi, C. Corral and N. Craig, *et al.* “A facility to Search for Hidden Particles at the CERN SPS: the SHiP physics case,” Rept. Prog. Phys. **79**, no.12, 124201 (2016) [arXiv:1504.04855 [hep-ph]].
- [86] C. Ahdida *et al.* [SHiP], “The experimental facility for the Search for Hidden Particles at the CERN SPS,” JINST **14**, no.03, P03025 (2019) [arXiv:1810.06880 [physics.ins-det]].
- [87] K. Bondarenko, A. Boyarsky, T. Bringmann, M. Hufnagel, K. Schmidt-Hoberg and A. Sokolenko, “Direct detection and complementary constraints for sub-GeV dark matter,” JHEP **03**, 118 (2020) [arXiv:1909.08632 [hep-ph]].
- [88] M. Cirelli, A. Strumia and J. Zupan, “Dark Matter,” [arXiv:2406.01705 [hep-ph]].
- [89] Y. Meng *et al.* [PandaX-4T], Phys. Rev. Lett. **127** (2021) no.26, 261802 [arXiv:2107.13438 [hep-ex]].
- [90] D. S. Akerib *et al.* [LUX-ZEPLIN Collaboration], “Projected WIMP Sensitivity of the LUX-ZEPLIN (LZ) Dark Matter Experiment,” arXiv:1802.06039 [astro-ph.IM].

- [91] D. N. Spergel and P. J. Steinhardt, “Observational evidence for selfinteracting cold dark matter,” *Phys. Rev. Lett.* **84**, 3760-3763 (2000) [arXiv:astro-ph/9909386 [astro-ph]].
- [92] J. J. Sakurai, *Modern Quantum Mechanics* (Addison-Wesley, Reading, MA, 1994).
- [93] F. Kahlhoefer, K. Schmidt-Hoberg, M. T. Frandsen and S. Sarkar, “Colliding clusters and dark matter self-interactions,” *Mon. Not. Roy. Astron. Soc.* **437**, no.3, 2865-2881 (2014) [arXiv:1308.3419 [astro-ph.CO]].
- [94] B. Colquhoun, S. Heeba, F. Kahlhoefer, L. Sagunski and S. Tulin, “Semiclassical regime for dark matter self-interactions,” *Phys. Rev. D* **103**, no.3, 035006 (2021) [arXiv:2011.04679 [hep-ph]].
- [95] F. Kahlhoefer, K. Schmidt-Hoberg and S. Wild, “Dark matter self-interactions from a general spin-0 mediator,” *JCAP* **08**, 003 (2017) [arXiv:1704.02149 [hep-ph]].
- [96] S. Tulin, H. B. Yu and K. M. Zurek, “Beyond Collisionless Dark Matter: Particle Physics Dynamics for Dark Matter Halo Structure,” *Phys. Rev. D* **87**, no.11, 115007 (2013) [arXiv:1302.3898 [hep-ph]].
- [97] R. Dave, D. N. Spergel, P. J. Steinhardt and B. D. Wandelt, “Halo properties in cosmological simulations of selfinteracting cold dark matter,” *Astrophys. J.* **547**, 574-589 (2001) [arXiv:astro-ph/0006218 [astro-ph]].
- [98] O. D. Elbert, J. S. Bullock, S. Garrison-Kimmel, M. Rocha, J. Oñorbe and A. H. G. Peter, “Core formation in dwarf haloes with self-interacting dark matter: no fine-tuning necessary,” *Mon. Not. Roy. Astron. Soc.* **453**, no.1, 29-37 (2015) [arXiv:1412.1477 [astro-ph.GA]].
- [99] T. Ren, A. Kwa, M. Kaplinghat and H. B. Yu, “Reconciling the Diversity and Uniformity of Galactic Rotation Curves with Self-Interacting Dark Matter,” *Phys. Rev. X* **9**, no.3, 031020 (2019) [arXiv:1808.05695 [astro-ph.GA]].
- [100] D. Harvey, R. Massey, T. Kitching, A. Taylor and E. Tittley, “The non-gravitational interactions of dark matter in colliding galaxy clusters,” *Science* **347**, 1462-1465 (2015) [arXiv:1503.07675 [astro-ph.CO]].
- [101] M. Bradac, S. W. Allen, T. Treu, H. Ebeling, R. Massey, R. G. Morris, A. von der Linden and D. Applegate, “Revealing the properties of dark matter in the merging cluster MACSJ0025.4-1222,” *Astrophys. J.* **687**, 959 (2008) [arXiv:0806.2320 [astro-ph]].
- [102] S. W. Randall, M. Markevitch, D. Clowe, A. H. Gonzalez and M. Bradac, “Constraints on the Self-Interaction Cross-Section of Dark Matter from Numerical Simulations of the Merging Galaxy Cluster 1E 0657-56,” *Astrophys. J.* **679**, 1173-1180 (2008) [arXiv:0704.0261 [astro-ph]].
- [103] H. Sieber, D. Banerjee, P. Crivelli, E. Depero, S. N. Gninenko, D. V. Kirpichnikov, M. M. Kirsanov, V. Poliakov and L. Molina Bueno, “Prospects in the search for a new light Z' boson with the NA64 μ experiment at the CERN SPS,” *Phys. Rev. D* **105**, no.5, 052006 (2022) [arXiv:2110.15111 [hep-ex]].
- [104] Y. Kahn, G. Krnjaic, N. Tran and A. Whitbeck, “ M^3 : a new muon missing momentum experiment to probe $(g - 2)_\mu$ and dark matter at Fermilab,” *JHEP* **09**, 153 (2018) [arXiv:1804.03144 [hep-ph]].
- [105] M. Cirelli, E. Del Nobile and P. Panci, “Tools for model-independent bounds in direct dark matter searches,” *JCAP* **10**, 019 (2013) [arXiv:1307.5955 [hep-ph]].

- [106] P. W. Graham, R. Harnik, S. Rajendran and P. Saraswat, “Exothermic Dark Matter,” *Phys. Rev. D* **82**, 063512 (2010) [arXiv:1004.0937 [hep-ph]].
- [107] J. Li, L. Su, L. Wu and B. Zhu, “Spin-dependent sub-GeV inelastic dark matter-electron scattering and Migdal effect. Part I. Velocity independent operator,” *JCAP* **04**, 020 (2023) [arXiv:2210.15474 [hep-ph]].
- [108] N. Anand, A. L. Fitzpatrick and W. C. Haxton, “Weakly interacting massive particle-nucleus elastic scattering response,” *Phys. Rev. C* **89**, no.6, 065501 (2014) [arXiv:1308.6288 [hep-ph]].
- [109] A. Y. Potekhin, A. F. Fantina, N. Chamel, J. M. Pearson and S. Goriely, “Analytical representations of unified equations of state for neutron-star matter,” *Astron. Astrophys.* **560**, A48 (2013) [arXiv:1310.0049 [astro-ph.SR]].
- [110] S. Goriely, N. Chamel and J. M. Pearson, “Further explorations of Skyrme-Hartree-Fock-Bogoliubov mass formulas. XII: Stiffness and stability of neutron-star matter,” *Phys. Rev. C* **82**, 035804 (2010) [arXiv:1009.3840 [nucl-th]].
- [111] N. B. Zhang and B. A. Li, “Constraints on the muon fraction and density profile in neutron stars,” *Astrophys. J.* **893**, 61 (2020) [arXiv:2002.06446 [astro-ph.HE]].
- [112] R. Garani, Y. Genolini and T. Hambye, “New Analysis of Neutron Star Constraints on Asymmetric Dark Matter,” *JCAP* **05**, 035 (2019) [arXiv:1812.08773 [hep-ph]].
- [113] J. L. Feng, J. Smolinsky and P. Tanedo, “Dark Photons from the Center of the Earth: Smoking-Gun Signals of Dark Matter,” *Phys. Rev. D* **93**, no.1, 015014 (2016) [erratum: *Phys. Rev. D* **96**, no.9, 099901 (2017)] [arXiv:1509.07525 [hep-ph]].
- [114] M. Blennow, S. Clementz and J. Herrero-Garcia, “Pinning down inelastic dark matter in the Sun and in direct detection,” *JCAP* **04**, 004 (2016) [arXiv:1512.03317 [hep-ph]].
- [115] J. Lundberg and J. Edsjo, “WIMP diffusion in the solar system including solar depletion and its effect on earth capture rates,” *Phys. Rev. D* **69**, 123505 (2004) [arXiv:astro-ph/0401113 [astro-ph]].
- [116] R. Garani and J. Heeck, “Dark matter interactions with muons in neutron stars,” *Phys. Rev. D* **100**, no.3, 035039 (2019) [arXiv:1906.10145 [hep-ph]].
- [117] T. Binder, L. Covi, A. Kamada, H. Murayama, T. Takahashi and N. Yoshida, “Matter Power Spectrum in Hidden Neutrino Interacting Dark Matter Models: A Closer Look at the Collision Term,” *JCAP* **11**, 043 (2016) [arXiv:1602.07624 [hep-ph]].
- [118] Y. Ashie *et al.* [Super-Kamiokande], “A Measurement of atmospheric neutrino oscillation parameters by SUPER-KAMIOKANDE I,” *Phys. Rev. D* **71**, 112005 (2005) [arXiv:hep-ex/0501064 [hep-ex]].
- [119] J. F. Navarro, C. S. Frenk and S. D. M. White, “A Universal density profile from hierarchical clustering,” *Astrophys. J.* **490**, 493 (1997) [astro-ph/9611107].
- [120] J. F. Navarro, C. S. Frenk and S. D. M. White, “The Structure of cold dark matter halos,” *Astrophys. J.* **462**, 563 (1996) [astro-ph/9508025].